

**Ultrafast Electron Microscopes: Design Criteria, Electron Sources, and
Column Modeling**

BY

Joel A. Berger
B.S., University of Illinois at Chicago, 2005

THESIS

Submitted as partial fulfillment of the requirements
for the degree of Doctor of Philosophy in Physics
in the Graduate College of the
University of Illinois at Chicago, 2014

Chicago, Illinois

Defense Committee:

W. Andreas Schroeder, Chair and Advisor
Nestor Zaluzec, Electron Microscopy Center, Argonne National Laboratory
Alan Nicholls, Research Resources Center
Christoph Grein
Robert Klie



This work is licensed under the Creative Commons Attribution-NonCommercial-NoDerivs 3.0 United States License. To view a copy of this license, visit <http://creativecommons.org/licenses/by-nc-nd/3.0/us/> or send a letter to

Creative Commons

444 Castro Street, Suite 900

Mountain View, CA, 94041, USA.

This thesis is dedicated to my parents, who in love and infinite patience always encouraged me, no matter how many questions I asked; and to my amazing wife, who has believed in me since the day we met.

ACKNOWLEDGMENT

I would like to thank my advisor, W. Andreas Schroeder, and all of my committee members, Nestor Zaluzec, Alan Nicholls, Christoph Grein and Robert Klie. It has been my honor to learn from and work with each one of you.

I would like to thank all of my research group members, past and present, Stephanie Schieffer, Benjamin Rickman, John Hogan, Tuo Li, Daniel Brajkovic, Michael Greco, Michael Szotek, and Robin Taylor. Through your professional efforts and personal interactions, you have made my time at UIC most enjoyable. I also want to thank former member Nathan Rimington for laying the groundwork for the presented laser.

I want to thank my collaborators, Nigel Browning, now of Pacific Northwest National Laboratory, and Dean Miller and Jon Hiller of the Electron Microscopy Center at Argonne National Laboratory.

Finally, I want to thank the funding agencies which have made this research possible: the National Science Foundation (DMR-0619573) and the Department of Energy (DE-FG52-06NA26213 and DE-FG52-09NA29451). I have been honored to be personally funded by a Department of Education GAANN fellowship (DED P200A070409), a UIC Dean's Scholar Award fellowship, and a Physics Department James Kouvel Fellowship.

JAB

TABLE OF CONTENTS

<u>CHAPTER</u>		<u>PAGE</u>
1	INTRODUCTION	1
2	THE ANALYTIC GAUSSIAN MODEL	5
2.1	Formal Evolution	5
2.2	Evolution of a Gaussian Distribution	8
2.3	Generating the Differential Equations	11
2.4	The Differential Equation System	13
2.5	Validity and Limitations	14
3	EXTENSION OF THE ANALYTIC GAUSSIAN MODEL FOR UEM COLUMN MODELING	15
3.1	Determining Appropriate Initial Conditions	16
3.1.1	A Simplistic Analytic Form	16
3.1.2	Iterative Spatial/Temporal Bin Model	21
3.2	Implications of Liouville's Theorem	24
3.3	Formal Extension to Include Generic External Forces	26
3.3.1	Mathematical Formulation of External Force Contribution	27
3.3.2	Constant External Forces	29
3.3.3	Linear External Forces	29
3.3.4	Validity and Limitations	31
3.4	Extension to Include Magnetic Lenses, RF Cavities, and DC Accelerators	32
3.4.1	Region of Influence	33
3.4.2	Magnetic Lenses	33
3.4.3	RF Cavities	37
3.4.4	Acceleration Region	42
3.5	Implementation	46
4	MODEL RESULTS, PREDICTIONS AND IMPLICATIONS	48
4.1	Effect of Pulse Eccentricity on Dynamics	49
4.2	Effect of Space Charge on Dynamics	53
4.3	Space-charge Effects and Spatial Focusing	57
4.4	Compensation of Temporal Space-charge Effects: RF Cavities	60
4.5	UEM Column Example	65
5	UEM DESIGN CONSIDERATIONS	69
5.1	Pulse Charge Requirement	70

TABLE OF CONTENTS (Continued)

<u>CHAPTER</u>		<u>PAGE</u>
5.2	Generation Current Limitations	71
5.3	Beam Quality and Resolution Limit	74
6	PROTOTYPE INSTRUMENT	77
6.1	Yb:KGW Laser System	77
6.1.1	Laser Introduction	79
6.1.2	Laser Head Design	81
6.1.3	The Yb:KGW laser cavity	87
6.1.4	Mode-locked laser operation	88
6.1.5	Frequency doubling	94
6.1.6	Long-term Performance Enhancements	96
6.2	Column Design and Construction	97
6.3	Accelerator Design	99
6.4	Magnetic Lenses	103
6.4.1	Design	105
6.4.2	Thermal Properties	109
6.5	Deflection Plates	110
7	PHOTOCATHODE ENGINEERING	113
7.1	Experimental Methodology	115
7.2	Single-photon Photoemission from Flat Metal Photocathodes	116
7.3	Two-photon Assisted Thermionic Emission	119
7.4	Nanopatterned (Plasmonic) Photocathodes	122
7.4.1	The Grating Coupling Geometry	123
7.4.2	Commercial Grating on Glass	125
7.4.3	Sinusoidal Grating	127
7.4.4	Sinusoidal Grating, Rotated	131
7.4.5	Trenched Grating	133
7.4.6	Discussion	134
7.5	Excited State Thermionic Emission	135
7.6	Future Prospects	140
8	CONCLUSIONS	142
8.1	Modeling	142
8.2	UEM Design	148
8.3	Photocathode Engineering	150
	APPENDIX	153
	CITED LITERATURE	158
	VITA	168

LIST OF FIGURES

FIGURE		PAGE
1	Results of bin model for computing initial conditions	23
2	Comparison of the AG model and a kinematic model of a magnetic lens	36
3	An example of a tanh form acceleration region for three different “sharpness” values	45
4	AG simulation of free-space pulse expansion	51
5	Idealistic free-space pulse evolution vs charge density	54
6	More realistic free-space pulse evolution vs charge density	56
7	AG model simulated focal behavior of perfect magnetic lenses as a function of pulse charge N	58
8	Dynamics of the pulse length and width under the influence of an RF cavity	61
9	Example model of a compound system of electron-optical elements .	66
10	Picture of the prototype UEM column at UIC	78
11	Laser crystal and anti-reflection coating	82
12	Thermal profile and thermal lens shaping of KGW crystal pumping	86
13	Schematic and stability plot of employed Yb:KGW ultrafast laser .	89
14	Autocorrelation measurements of employed ultrafast laser’s pulse du- ration	91
15	Power measurements of employed ultrafast laser	93
16	Side view of main chamber	98
17	Pictures of the employed Togawa-inspired custom cathode-anode pair	100
18	Schematic of the employed Togawa-inspired custom cathode-anode pair	101
19	An example of a tanh form acceleration region for three different “sharpness” values	102
20	Picture of the high-voltage side of the prototype UEM	104
21	Schematic of a generic magnetic lens with a pole-piece	106
22	Design schematic of our magnetic lens with a pole-piece	107
23	Side-view picture of the employed two custom large-bore magnetic lenses	109
24	Schematic diagram of one pair of deflection plates	111
25	Picture of custom deflector plates	112
26	Beam profile simulation of experimental setup	114
27	Single-photon photoemission from Tungsten	118
28	Measured Fourier plane electron beam size and yield vs incident laser pulse energy on gold photocathode	120
29	Grating coupling geometry for driving a surface plasmon	125

LIST OF FIGURES (Continued)

<u>FIGURE</u>		<u>PAGE</u>
30	Damage to commercial gold-on-glass holographic grating	126
31	SEM image of sinusoidal grating on silicon	127
32	Photoemission characteristics of laser-driven plasmons on a one-dimensional periodic gold surface	129
33	Comparison of the collinear and rotated plasmonic excitation geome- tries	132
34	Electron emission vs UV laser pulse energy for GaSb and InSb . . .	136

LIST OF ABBREVIATIONS

AG	Analytic Gaussian (Model)
AR	Anti-Reflection
ARPES	Angle-resolved Photoemission Spectroscopy
BBO	β -Barium Borate — β -Ba(BO ₂) ₂
CCD	Charge-coupled Device (camera)
CF	ConFlat
CPAN	Comprehensive Perl Archive Network
CW	Continuous Wave
CXLS	Compact X-ray Light Source
DC	Direct Current (i.e. Static Electric Field)
DTEM	Dynamic Transmission Electron Microscope/Microscopy
ESTE	Excited State Thermionic Emission
FEM	Finite Element Method
FIB	Focused Ion Beam
FWHM	Full-Width at Half Maximum
GRIN	Gradient Index (of Refraction)
GSL	GNU Scientific Library

LIST OF ABBREVIATIONS (Continued)

GVD	Group Velocity Dispersion
HW1/eM	Half-Width at 1/e Maximum
KGW	Potassium Gadolinium Tungstate — $\text{KGd}(\text{WO}_4)_2$
KYW	Potassium Yttrium Tungstate — $\text{KY}(\text{WO}_4)_2$
LBO	Lithium Triborate — LiB_3O_5
LHS	Left Hand Side
LO	Longitudinal Optical (Phonon)
ML	Mode-Locked
NCF	(UIC) Nano Core Facility
PAPE	Plasmon-Assisted Photoemission
PDL	Perl Data Language
Q	Quality Factor
RHS	Right Hand Side
RF	Radio Frequency
RMS	Root Mean Square
SBR	Saturable Bragg Reflector
SEM	Scanning Electron Microscope/Microscopy
SHG	Second Harmonic Generation

LIST OF ABBREVIATIONS (Continued)

TEM	Transmission Electron Microscope/Microscopy
TEM ₀₀	Transverse Electromagnetic 00 Mode
TLS	Thermal Lens Shaping/Shaped
TM ₀₁₀	Transverse Magnetic 010 Mode
TOF	Time of Flight
UED	Ultrafast Electron Diffraction
UEM	Ultrafast Electron Microscope/Microscopy
UIC	University of Illinois at Chicago
UV	Ultraviolet
YAG	Yttrium Aluminum Garnet — $\text{Y}_3\text{Al}_5\text{O}_{12}$
XFEL	X-ray Free Electron Laser

SUMMARY

Dynamic Transmission Electron Microscopy, and its picosecond/femtosecond subclass Ultrafast Electron Microscopy, is an emerging field in instrumentation science. It attempts to combine the nanoscale spatial resolution of transmission electron microscopes with the temporal resolution of modern ultrafast lasers. In this thesis, I present my contributions to this young field. These include a novel model for simulating the dynamics of ultrafast electron pulses in electron microscope systems, design criteria for constructing such a system, and theoretical and experimental groundwork geared towards selecting a useful photocathode for electron pulse generation. I also present the prototype ultrafast electron microscope system being built at UIC.

CHAPTER 1

INTRODUCTION

The development of laboratory-scale instrumentation for the direct visualization of fundamental ultrafast (i.e., sub-nanosecond) events with nano-scale (even atomic) spatial resolution is a current active area of research (51). In many areas of physics, chemistry and materials science a space-time resolution in the sub-1nm·ps range is ideally required to allow for the observation of the fastest structural events. A promising approach is to employ ultrashort pulses of electrons generated by a laser-driven 10-100keV photoelectron gun to probe the dynamics of the specimen that has been perturbed by a synchronized laser pulse (51). Ultrafast electron diffraction (UED) or femtosecond electron diffraction (FED) (98; 107; 25) is an example of this type of technique and has been used successfully to elucidate atomic-scale dynamics in melting (25; 91; 97), chemical bond breaking (111), etc. Direct time-resolved imaging of similar events can be accomplished using transmission electron microscopy (TEM). To date, such dynamic transmission electron microscopes (DTEMs) (20; 33) have been developed for both single-shot imaging with $\sim 10^5$ nm·ps space-time resolution (e.g., 30ns electron pulses and 5-10nm spatial resolution (55; 12)) and ~ 1 nm·ps space-time resolution (~ 100 fs with a few nanometer resolution (80)) in the multi-shot data acquisition mode of operation. Both of these instruments, which operate with vastly different pulse charge densities, employ retro-fitted standard electron microscope columns and are limited in performance mainly by space-charge effects.

Improvements in the performance of DTEMs, especially ultrafast electron microscopes (UEMs), and UED systems will likely require the implementation of techniques that offset or compensate for deleterious space-charge effects (13; 62). Such performance optimization efforts will require efficient models of electron pulse propagation dynamics that include the ability to simulate the action of electron optical elements (including the photoelectron gun itself) on the pulse. Indeed 2nd generation UED instruments are now beginning to employ both magnetic lenses and radio-frequency (RF) resonant cavities (102; 103) to optimize the electron pulse delivery to the specimen; that is, compensate for global space-charge effects in both the transverse and longitudinal pulse dimensions, respectively. Similarly, future UEM column designs are expected to use RF pulse compression cavities while circumventing high charge density beam cross-overs (i.e., beam foci).

In Chapter 2, I will introduce the work of Michalik and Sipe (70; 71), describing free-space electron bunch propagation in a mean-field self-similar Analytic Gaussian (AG) pulse treatment. For free-space propagation, the AG model of charge bunch dynamics has already been shown to be very consistent with full Monte Carlo (i.e., particle tracking) simulations for a wide variety of electron pulse shapes (70; 72), including the uniform ellipsoid (63). Due primarily to the versatility of the AG model, which results from its use of transverse and longitudinal pulse position and momentum variances, the AG approach is applicable to both the single electron per pulse limit (62), where momentum variances determine the pulse evolution and the model is exact (obeying Gaussian optics), and the high charge density limit in which space-charge effects dominate (63; 96; 25). Unfortunately, the AG model as laid out by Michalik and Sipe lacks

the ability to model the dynamics of electron pulses under the influence of external forces; this prevents the AG model from being used to simulate the behavior of electron pulses in realistic microscope columns. Additionally, to be useful for UEM, for which the electron pulse’s initial conditions are of notable importance for the performance of the instrument, a realistic set of initial conditions is essential for accurately modeling the pulse dynamics.

In Chapter 3, I present some optimizations to the AG model and develop useful initial conditions representing single-photon photoemission from a typical metal photocathode. I then present extensions to the Michalik and Sipe AG model which permit the inclusion of generic linear external forces, such as those due to perfect electron-optical elements in a microscope column. In order to adapt this extended AG model for simulating pulses in a realistic UEM column, I then present specific contributions that arise from magnetic lenses, RF cavities, and DC accelerators. The resulting computationally efficient propagation analysis can then be used to model, and hence design, UEM columns and UED systems in a straightforward manner. These analyses presented are performed in the non-relativistic limit, which is a reasonable approximation for the typical 20-200keV electron energies employed in UED and electron microscopy.

In Chapter 4, I apply the extended AG model to draw some initial insight into the dynamics of ultrafast electron pulses traversing a UEM column. One of the conclusions that I will make is that electron pulses which are oblate or “disk-like” in shape will be generally preferred to those that are prolate or “cigar-like.” Indeed for UEM, with typical laser pulse durations in the femtosecond to picosecond timescales, the electron pulses are likely to be oblate for reasonably sized incident laser spot sizes. Then in Chapter 5, I apply some well known results from the

field of electron microscopy, namely the Rose criterion (88), an ultrafast analog to the Child-Langmuir law (29; 57; 101), and the conservation of transverse emittance (45) (each of which will be introduced) to arrive at two design goals for building a UEM which will produce high-resolution images. First, that the electron pulses should be emitted from a large-area source, and second, that every effort must be made to reduce the initial rms transverse momentum (i.e., the emission cone angle) of the electron pulse as generated from the photocathode.

All of these considerations motivate the construction of the prototype UEM column being built by our group at UIC. In Chapter 6, I detail the design and fabrication of large-aperture electron-optical elements, which can readily admit these large width electron pulses; included among these are the accelerator and magnetic lenses. Then, before I conclude, I will in Chapter 7 highlight the photocathode engineering work which has been undertaken in an attempt to reduce the rms transverse momentum of the emitted electron pulses. In fact, the search for a low transverse momentum electron source has applications beyond UEM and UED; the fields of X-ray Free Electron Lasers (XFELs, (76)) and Compact X-ray Light Sources (CXLS) (11) will also benefit from such a source. I will present investigations of several different photoemission processes, some of which are yielding very promising results. Our recent work on excited-state thermionic emission (18) may even challenge long-standing ideas about which materials and processes may hold the keys to low-emittance (or high-brightness) electron sources.

CHAPTER 2

THE ANALYTIC GAUSSIAN MODEL

This chapter introduces the Analytic Gaussian (AG) model of Michalik and Sipe (70). In the AG model the dynamics of a Gaussian electron pulse are computed using a mean-field self-similar approximation. The result is a set of equations that can be solved very quickly using numerical methods on a modern computer. When checked against N-body simulations, the authors find that the model is also surprisingly accurate, even for a large set of non-Gaussian pulse shapes (70; 72). A drawback is that the only force included in this model is that of the internal repulsive space-charge field. In Chapter 3, I will extend this model, adding the influence of external forces, making it more generally applicable for UEM.

2.1 Formal Evolution

Before one may describe the evolution of a pulse of electrons, one must first learn to describe the pulse. Rather than record the position of each electron, commonly one writes a distribution function for the electrons. A distribution function describes the location of a number of objects in a certain space. This space may be a 1D line, a 3D space, or even a 6D phase space (three spatial dimensions and three momentum dimensions). The functional form may be chosen to appropriately characterize the objects in a natural way, however one property is true for all distribution functions: when integrated over all relevant space, all objects should be accounted

for. In n dimensional space, with N objects, this normalization condition on a distribution function f can be written mathematically as

$$N = \int_{\text{all space}} f(\vec{x}) d^n x, \quad (2.1)$$

which for 6D phase space is written as

$$N = \int f(\vec{r}, \vec{p}; t) d^3x d^3p. \quad (2.2)$$

This notation suggests to the reader that the distribution function is implicitly a function of time as well as of the spatial and momentum coordinates; for most circumstances however, the total number of particles N will not change with time.

For a classical set of N discrete particles (labeled by the index i), distributed in 6D space (3 position, 3 momentum) the distribution function is

$$f_D(\vec{r}, \vec{p}; t) = \sum_{i=1}^N \delta(\vec{r}_i - \vec{r}) \delta(\vec{p}_i - \vec{p}), \quad (2.3)$$

which automatically satisfies Equation 2.2. If the particles have mass m which interact with some potential $V(\vec{r}_i - \vec{r}_j)$, their motion is governed by the equations

$$\frac{d\vec{r}_i(t)}{dt} = \frac{\vec{p}_i(t)}{m} \quad (2.4a)$$

$$\frac{d\vec{p}_i(t)}{dt} = - \sum_j \frac{d}{d\vec{r}_i} V(\vec{r}_i - \vec{r}_j). \quad (2.4b)$$

Now let us consider the time evolution of f_D ;

$$\frac{\partial f_D}{\partial t} = \frac{d\vec{r}}{dt} \frac{\partial f_D}{\partial \vec{r}} + \frac{\partial f_D}{\partial \vec{p}} \frac{d\vec{p}}{dt}, \quad (2.5)$$

but with Equation 2.4 the final discrete evolution equation is

$$\frac{d}{dt} f_D(\vec{r}, \vec{p}; t) = -\frac{\vec{p}}{m} \frac{\partial}{\partial \vec{r}} f_D(\vec{r}, \vec{p}; t) + \frac{\partial}{\partial \vec{p}} f_D(\vec{r}, \vec{p}; t) \frac{\partial}{\partial \vec{r}} \iint d\vec{r}' d\vec{p}' V(\vec{r} - \vec{r}') f_D(\vec{r}', \vec{p}'; t), \quad (2.6)$$

where the extra negation comes from the change of perspective of Equation 2.4b from the frame of the individual particle i to the observer frame.

This analysis can be extended to continuous distributions by taking the ensemble average over Equation 2.6. In order to simplify the resulting equation to a useful result, one applies the usual mean-field approximation

$$\langle f_D(\vec{r}, \vec{p}; t) f_D(\vec{r}', \vec{p}'; t) \rangle = \langle f_D(\vec{r}, \vec{p}; t) \rangle \langle f_D(\vec{r}', \vec{p}'; t) \rangle, \quad (2.7)$$

so that the formal evolution of a continuous distribution is given by

$$\frac{d}{dt} f(\vec{r}, \vec{p}; t) = -\frac{\vec{p}}{m} \frac{\partial}{\partial \vec{r}} f(\vec{r}, \vec{p}; t) + \frac{\partial}{\partial \vec{p}} f(\vec{r}, \vec{p}; t) \frac{\partial}{\partial \vec{r}} \iint d\vec{r}' d\vec{p}' V(\vec{r} - \vec{r}') f(\vec{r}', \vec{p}'; t). \quad (2.8)$$

Although this equation looks very similar to Equation 2.6, notice that it contains the mean-field approximation that has already been seen and the distribution function is now implicitly self-similar, an approximation that the discrete description did not employ.

2.2 Evolution of a Gaussian Distribution

The formal evolution explored in Section 2.1 allows for any distribution function. For Ultrafast Electron Microscopy, the electron pulse is generated by a laser pulse, therefore the electron pulse can be thought to be a Gaussian in space and time, mimicking the laser pulse which generated it. How correct this assumption is will be explored in Section 3.1. Consider a Gaussian distribution function, generally of the form

$$f(\vec{r}, \vec{p}; t) = C(t) \exp[-G(\vec{r}, \vec{p}; t)] . \quad (2.9)$$

The analysis presented here will consider a cylindrically symmetric pulse. For the remainder of this analysis, the subscripts $_T$ (transverse) and $_z$ (longitudinal) will accompany many quantities, reflecting the congruence of x and y . The subscript α will refer to either $_T$ or $_z$. In order to model several important physical characteristics of the pulse, we choose the argument (i.e. the function G) as

$$G(\vec{r}, \vec{p}; t) = \frac{x^2 + y^2}{2\sigma_T} + \frac{z^2}{2\sigma_z} + \frac{[p_x - (\gamma_T/\sigma_T)x]^2 + [p_y - (\gamma_T/\sigma_T)y]^2}{2\eta_T} + \frac{[p_z - (\gamma_z/\sigma_z)z]^2}{2\eta_z} . \quad (2.10)$$

This parameterization defines the spatial variance σ_α , the local momentum variance η_α , and the momentum chirp γ_α in each spatial direction α . The “chirp” of a pulse quantifies the difference in average local momentum from one side of the pulse to the other. For example, in a pulse which is normally (positively) chirped longitudinally, electrons near the front of the pulse will

be moving faster (on average) than those in the back. The normalization constant $C(t)$, for this distributions of N total particles, is found by applying equation Equation 2.2:

$$C(t) = \frac{N}{(2\pi)^3} \left(\frac{1}{\sigma_T^2 \eta_T^2 \sigma_z \eta_z} \right)^{\frac{1}{2}}. \quad (2.11)$$

To help simplify what is already becoming a complex problem, these equations may be viewed from a matrix perspective if we define the “coordinate vector”

$$u_i = \{x, p_x, y, p_y, z, p_z\}. \quad (2.12)$$

In this space, Equation 2.10 becomes

$$G(\vec{r}, \vec{p}; t) = \frac{1}{2} \sum_{ij} A_{ij} u_i u_j, \quad (2.13)$$

where the 9 x 9 matrix A is defined as

$$A = \begin{pmatrix} a_T & 0 & 0 \\ 0 & a_T & 0 \\ 0 & 0 & a_z \end{pmatrix} \quad \text{and} \quad a_\alpha = \begin{pmatrix} 1/\sigma_\alpha + \gamma_\alpha^2/(\eta_\alpha \sigma_\alpha) & \gamma_\alpha/(\eta_\alpha \sigma_\alpha) \\ \gamma_\alpha/(\eta_\alpha \sigma_\alpha) & 1/\eta_\alpha \end{pmatrix}, \quad (2.14)$$

again with $\alpha = T$ or z . A nice property of Gaussians of this form is the convenient “Multidimensional Gaussian Integral” given by

$$(A^{-1})_{ij} = \frac{1}{N} \int u_i u_j f(\vec{r}, \vec{p}; t) d\vec{r} d\vec{p}, \quad (2.15)$$

which is a common form of integral analysis in Quantum Field Theory (see for example Peskin and Schroeder Equation 9.70). Application of this integral yields another 9 x 9 matrix

$$A^{-1} = \begin{pmatrix} a_T^{-1} & 0 & 0 \\ 0 & a_T^{-1} & 0 \\ 0 & 0 & a_z^{-1} \end{pmatrix} \quad \text{and} \quad a_\alpha^{-1} = \begin{pmatrix} \sigma_\alpha & \gamma_\alpha \\ \gamma_\alpha & \eta_\alpha + \gamma_\alpha^2 / \sigma_\alpha \end{pmatrix}. \quad (2.16)$$

Since time derivative of Equation 2.15 is simply

$$\frac{d}{dt}(A^{-1})_{ij} = \frac{1}{N} \int u_i u_j \frac{df(\vec{r}, \vec{p}; t)}{dt} d\vec{r} d\vec{p}, \quad (2.17)$$

and the time derivative of the components of A^{-1} are

$$\frac{d}{dt} a_\alpha^{-1} = \begin{pmatrix} \frac{d\sigma_\alpha}{dt} & \frac{d\gamma_\alpha}{dt} \\ \frac{d\gamma_\alpha}{dt} & \frac{d\eta_\alpha}{dt} + 2\frac{\gamma_\alpha}{\sigma_\alpha} \frac{d\gamma_\alpha}{dt} - \frac{\gamma_\alpha^2}{\sigma_\alpha^2} \frac{d\sigma_\alpha}{dt} \end{pmatrix}, \quad (2.18)$$

these components, when viewed in the context of Equation 2.8, form the left hand side (LHS) of the system of differential equations governing the evolution of σ_α , γ_α , and η_α , which will be established in the upcoming sections.

2.3 Generating the Differential Equations

Inserting Equation 2.8 into Equation 2.17 yields two integral terms, one related to the propagation of a non-charged Gaussian beam, the other adds the influence of the internal force due to Coulomb repulsion for an electron pulse. These terms will be denoted K^{flow} and K^{force} respectively,

$$\frac{d}{dt}(A^{-1})_{ij} = K_{ij}^{flow} + K_{ij}^{int}. \quad (2.19)$$

Collecting and expanding terms where possible gives these forms of the K terms

$$K_{ij}^{flow} \equiv -\frac{1}{N} \int u_i u_j \frac{\vec{p}}{m} \frac{\partial f}{\partial \vec{r}} d\vec{r} d\vec{p} \quad (2.20)$$

$$K_{ij}^{force} \equiv \frac{1}{N} \int u_i u_j \frac{\partial f}{\partial \vec{p}} \frac{\partial \Phi(\vec{r}; t)}{\partial \vec{r}} d\vec{r} d\vec{p} \quad (2.21)$$

$$\Phi(\vec{r}; t) \equiv \int d\vec{r}' V(\vec{r} - \vec{r}') n(\vec{r}'; t) \quad (2.22)$$

$$n(\vec{r}; t) \equiv \int d\vec{p} f(\vec{r}, \vec{p}; t) = \frac{N}{(2\pi)^{3/2} \sigma_T \sqrt{\sigma_z}} \exp\left(-\frac{x^2 + y^2}{2\sigma_T} - \frac{z^2}{2\sigma_z}\right). \quad (2.23)$$

Obviously the K^{flow} term is far easier to evaluate;

$$K^{flow} = \begin{pmatrix} k_T^{flow} & 0 & 0 \\ 0 & k_T^{flow} & 0 \\ 0 & 0 & k_z^{flow} \end{pmatrix} \quad \text{and} \quad k_\alpha^{flow} = \begin{pmatrix} \frac{2\sigma_\alpha}{m} & \frac{1}{m} \left(\eta_\alpha + \frac{\gamma_\alpha^2}{\sigma_\alpha} \right) \\ \frac{1}{m} \left(\eta_\alpha + \frac{\gamma_\alpha^2}{\sigma_\alpha} \right) & 0 \end{pmatrix}. \quad (2.24)$$

The K^{force} integrals, related to the internal force of the pulse's Coulombic repulsion, are far more complicated to evaluate. For more information about the derivation, see Reference (70).

The final matrices are

$$K^{force} = \begin{pmatrix} k_T^{force} & 0 & 0 \\ 0 & k_T^{force} & 0 \\ 0 & 0 & k_z^{force} \end{pmatrix}, \quad (2.25)$$

where

$$k_\alpha^{force} = \frac{Ne^2}{4\pi\epsilon_0} \frac{1}{2\pi^{1/2}\sigma_\alpha^{1/2}} L_\alpha(\xi) \begin{pmatrix} 0 & 1 \\ 1 & \frac{2\gamma_\alpha}{\sigma_\alpha} \end{pmatrix}. \quad (2.26)$$

The parameter ξ quantifies the spatial ellipticity of the electron pulse, defined as

$$\xi \equiv \sqrt{\frac{\sigma_z}{\sigma_T}}. \quad (2.27)$$

[Note that the original paper of Michalik and Sipe (Reference (70)) contained an error which incorrectly defined ξ ; this was corrected in an erratum (Reference (71)).] The family of L functions are

$$L_T(\xi) = \frac{3}{2} \left(L(\xi) + \frac{\xi^2 L(\xi) - \xi}{1 - \xi^2} \right) \quad (2.28a)$$

$$L_z(\xi) = \frac{3\xi^2}{\xi^2 - 1} (\xi L(\xi) - 1) \quad (2.28b)$$

$$L(\xi) = \frac{1}{2} \int_0^\pi \frac{1}{1 + \xi \sin(\theta)} d\theta. \quad (2.28c)$$

The integral function $L(\xi)$ (Equation 2.28c) can be further evaluated to the piecewise function

$$L(\xi) = \begin{cases} \frac{\arcsin \sqrt{1-\xi^2}}{\sqrt{1-\xi^2}} & 0 \leq \xi \leq 1 \\ \frac{\ln(\xi + \sqrt{\xi^2 - 1})}{\sqrt{\xi^2 - 1}} & \xi \geq 1, \end{cases} \quad (2.29)$$

which, although defined piecewise, is a smooth and well behaved function for all physically meaningful ξ .

2.4 The Differential Equation System

When these K matrices are summed (Equation 2.19) to form the right hand side (RHS) of the differential equations and compared to LHS derived above (Equation 2.18), the non-zero elements finally yield a system of differential equations which govern the dynamics of these Gaussian beam parameters.

$$\frac{d\sigma_\alpha}{dt} = \frac{2\gamma_\alpha}{m} \quad (2.30a)$$

$$\frac{d\gamma_\alpha}{dt} = \frac{1}{m} \left(\eta_\alpha + \frac{\gamma_\alpha^2}{\sigma_\alpha} \right) + \frac{Ne^2}{4\pi\epsilon_0} \frac{1}{6\sqrt{\sigma_\alpha\pi}} L_\alpha(\xi) \quad (2.30b)$$

$$\frac{d\eta_\alpha}{dt} = -\frac{2\gamma_\alpha\eta_\alpha}{m\sigma_\alpha} \quad (2.30c)$$

These equations are the crux of the model presented by Michalik and Sipe for the time evolution of a Gaussian electron pulse propagating through free space (no external forces). They form the basis upon which much of the work in the following chapters is founded.

2.5 Validity and Limitations

This AG formalism of Michalik and Sipe (70) employs a mean-field approximation in the evolution of the dynamical effect of the electron pulse’s internal space-charge field. This is of course not strictly accurate for a Gaussian charge distribution and the error leads to a distortion of the pulse shape. The “self-similar” nature of the model, the fact that the overall shape of the pulse cannot change, prevents inclusion of these distortions. Even so, the AG model of charge bunch dynamics has been benchmarked against particle tracking simulations for a number of electron pulse shapes (70; 72), including the uniform ellipsoid which explicitly features a linear internal space-charge field (63).

CHAPTER 3

EXTENSION OF THE ANALYTIC GAUSSIAN MODEL FOR UEM COLUMN MODELING

In Chapter 2, I have introduced the AG model, originally presented by Michalik and Sipe (70). Although it is a very impressive model and a very useful starting point, because it cannot include the influence of external forces on the pulse dynamics, it does not provide the complete picture of the evolution of an electron pulse through an entire microscope column. Further, it does not contain a set of initial conditions which reflect a realistic photoemission process.

In the following chapter, I will derive a set of initial conditions which, though simplistic, should be sufficient to simulate single-photon photoemission from a metal, and which may additionally serve as a basis for future sets of initial conditions for other photoemission processes. I will then present a model which builds on and extends the AG model to include the influence of external forces on pulses. I will also include the mathematical representations of magnetic lenses, TM_{010} RF cavities, and DC accelerators. With these computational tools it is possible to form one model which has the ability to simulate a UEM column. Indeed I have implemented this model in the Perl programming language, in a form generic enough to easily model many different electron column configurations and yet is computationally fast enough to be used to design and optimize a column.

3.1 Determining Appropriate Initial Conditions

For a DTEM or UED apparatus, where the electron pulse is produced in a laser-driven photoelectron gun, the implementation of the AG model of Michalik and Sipe (70) requires knowledge of the initial ($t = 0$) bunch parameters immediately after generation at the photocathode surface inside the acceleration region of the gun. For the purposes of this thesis, we will make a simple approximation to the behavior of the gun in order to provide generic initial conditions for the electron pulse.

3.1.1 A Simplistic Analytic Form

Consider a single-photon photoemission process with a spatially cylindrically symmetric incident Gaussian laser beam with Gaussian temporal irradiance profile

$$I(x, y, t) = I_0 \exp \left(-\frac{(x^2 + y^2)}{w^2} - \frac{t^2}{\tau^2} \right), \quad (3.1)$$

where w is the half-width 1/e maximum (HW1/eM) of the spatial irradiance distribution, τ is the HW1/eM pulse duration and I_0 is the peak pulse irradiance incident on a flat metallic photocathode. A laser pulse of this form has a temporal uncertainty $\Delta t_L = \tau/\sqrt{2}$.

The initial transverse properties of the emitted electron beam are easily understood. The electron pulse's initial spatial variance is simply

$$\sigma_T(0) = (\Delta x)^2 = (\Delta y)^2 = \frac{w^2}{2}. \quad (3.2)$$

For spatially-uniform photoemission from a planar photocathode, from symmetry we have $\gamma_T(0) = 0$; i.e., there is no initial transverse spatial momentum chirp across the electron bunch. Finally, thanks to the careful analysis of Dowell and Schmerge (34) (confirmed by Jensen *et al.* (45)), we know that metallic photocathode's initial transverse momentum variance at $t = 0$ is given by

$$\eta_T(0) = (\Delta p_T)^2 \approx \frac{m}{3}(\hbar\omega - \Phi), \quad (3.3)$$

in the limit where the maximum excess photoemission energy, $\Delta E = \hbar\omega - \Phi$ is significantly greater than the thermal energy $k_B T$ of the electrons in the photocathode – a condition that is generally met in laser-driven DC photoelectron guns. For completeness we note that for thermionic emission $\Delta p_T = \sqrt{mk_B T_e}$ where k_B is the Boltzmann constant and T_e is the electron temperature (34; 45).

In the longitudinal direction (z), the interplay between acceleration, $a = eE_{DC}/m$, in the DC gun and the physics of the photoemission process determine the initial values of σ_z , the longitudinal spatial variance, and γ_z , the longitudinal momentum chirp, of an electron bunch. Two limiting regimes for the initial longitudinal variances $\sigma_i(0)$ are readily identified: (i) when the incident drive laser pulse duration is sufficiently long to ensure that the distance the electrons travel due to acceleration in E_{DC} over the laser pulse duration is much greater than the distance traveled by electrons moving with a constant velocity $v_{max} = \sqrt{2\Delta E/m}$, the maximum photoemission velocity, over the same time period; and (ii) the opposite regime for sufficiently short laser pulse durations.

In the long-pulse regime, the DC field dominated case, we assume that the intrinsic velocity of the emitted electrons is negligible. The emitted electrons travel an average distance Δz , during the Δt_L rms laser pulse duration given by,

$$\sqrt{\sigma_z(0)} \approx \Delta z = \frac{1}{2}a(\Delta t_L)^2 = \frac{eE_{DC}\tau^2}{4m}. \quad (3.4)$$

By a similar logic, we can say that the ‘front’ of the pulse then has a velocity equal to $a\Delta t_L$, while the ‘back’ of the pulse (a distance $\frac{1}{2}\sqrt{\sigma_z(0)}$ from the electron bunch peak) has zero velocity since it has just been generated. From this one sees that the initial linear chirp across the pulse is given by

$$\gamma_z(0) \approx m\Delta v\Delta z = ma\Delta t_L\sqrt{\sigma_z(0)} = \frac{eE_{DC}\tau}{\sqrt{2}}\sqrt{\sigma_z(0)}. \quad (3.5)$$

In the short pulse limit, where the acceleration in the DC gun field over the incident laser pulse duration can be neglected, the initial electron bunch properties are determined primarily by the photoemission physics. Since the electric field has no time to influence the front of the pulse before the back is also generated we can say that the front of the pulse has a velocity equal to v_{max} and the back is essentially stationary just after generation. Further, since the photoemission efficiency is proportional to ΔE^2 (94) the distribution of emitted electrons vs velocity is proportional to v^4 ; therefore to a first approximation it is reasonable to say that in

this case $\Delta v \approx v_{max}$. The pulse's initial spatial variance Δz is therefore approximately to the spread of distances traveled during the laser pulse duration Δt_L ,

$$\sqrt{\sigma_z(0)} \approx \Delta z = \Delta v \Delta t_L = \frac{v_{max} \tau}{\sqrt{2}}. \quad (3.6)$$

Once again, we can use this information to determine a velocity chirp across the pulse in this regime,

$$\gamma_z(0) \approx m \Delta v \Delta z = m v_{max} \sqrt{\sigma_z(0)}, \quad (3.7)$$

For simplicity of use, one may combine the initial conditions resulting from these two cases. Since they arise from independent processes, the initial spatial uncertainties $\sigma_z(0)$ may be added naively

$$\sigma_z(0) \approx \frac{(v_{max} \tau)^2}{2} + \left(\frac{e E_{DC} \tau^2}{4m} \right)^2. \quad (3.8)$$

In the case of the initial momentum chirp terms $\gamma_z(0)$, while it is perhaps more rigorously correct to naively add the terms with the spatial variance evaluated in each respective limit, we propose that the evaluation be done in terms of the resultant form presented in Equation 3.8, keeping σ_z unevaluated,

$$\gamma_z(0) \approx \sqrt{\sigma_z(0)} \left(m v_{max} + \frac{e E_{DC} \tau}{\sqrt{2}} \right). \quad (3.9)$$

In this way the model may, in an intermediate case, more closely reflect the pulse length as modeled rather than the pulse length as idealized in each limiting case.

Finally, and again from a simplistic viewpoint, only the electrons generated with positive longitudinal momentum will contribute to the pulse since those electrons generated with negative momentum do not leave the photocathode. This implies that the final initial condition, the local momentum uncertainty in the longitudinal direction η_z , is half that of the transverse directions; that is to say

$$(\Delta p_z)^2 = \left(\frac{\Delta p_{x,y}}{2} \right)^2, \quad (3.10)$$

so that

$$\eta_z(0) \approx \frac{\eta_T(0)}{4}, \quad (3.11)$$

which is certainly expected to be reasonably accurate in the short-pulse limit, where the acceleration has had no effect (see Section 3.1.2 for further investigation).

In conclusion, the resulting set of analytic initial conditions for an incident Gaussian laser pulse of the form given in Equation 3.1 are

$$\sigma_T(0) \approx \frac{w^2}{2} \quad (3.12a)$$

$$\sigma_z(0) \approx \frac{(v_{max}\tau)^2}{2} + \left(\frac{eE_{DC}\tau^2}{4m} \right)^2 \quad (3.12b)$$

$$\gamma_T(0) \approx 0 \quad (3.12c)$$

$$\gamma_z(0) \approx \sqrt{\sigma_z(0)} \left(mv_{max} + \frac{eE_{DC}\tau}{\sqrt{2}} \right) \quad (3.12d)$$

$$\eta_T(0) \approx \frac{m}{3}(\hbar\omega - \Phi) \quad (3.12e)$$

$$\eta_z(0) \approx \frac{\eta_T(0)}{4}. \quad (3.12f)$$

Unless otherwise noted, these initial conditions will be used in all simulations for the remainder of this paper.

We recognize that these initial conditions for an electron pulse generated by a laser-driven DC gun are idealized in that they neglect several important effects; in particular, the interplay of dispersive ($\eta_i(0) \neq 0$) and space-charge effects in the acceleration region of the photoelectron gun and transverse and longitudinal effects due to the divergence of the DC field in the vicinity of the gun anode (17; 100). Such effects and the limits of the validity of the longitudinal terms of Equation 3.12, within the context of the AG model, will be presented in Section 3.1.2. However, Equation 3.12 also represents a defined set of initial conditions that allows the effect of electron optics (i.e., magnetic lenses and RF cavities) on electron pulse propagation to be more readily understood. Moreover, they reflect the fact that the majority of DC photoelectron guns are driven by laser pulses with spatial and temporal profiles that are close to Gaussian (107; 91). Only for specialized cases, such as the generation of uniform ellipsoid electron bunch shapes, is spatial and temporal manipulation of the incident laser pulse considered (63; 59).

3.1.2 Iterative Spatial/Temporal Bin Model

To test the validity of the simplistic model presented above, I also developed a bin model that depends on nothing other than basic Newtonian kinematics and a simple quantum-mechanical “transmission” function over a barrier. This function represents the likelihood of emission versus emission energy; the maximum energy being the full excess photoemission energy ΔE .

In the model, the space in front of the photocathode is binned into segments in ranges of distance from the photocathode. The total laser pulse duration is then binned into slices of

time for a total duration of $N\tau$, a few times the HW1/eM duration τ ; N is a number selected to accumulate enough of the total laser pulse for an accurate simulation. In this notation the peak of the pulse occurs at time $N\tau/2$. For each slice of time, one can determine the relative number of electrons generated in that slice (normalized to the total number that will be created by the end of the simulation), and the velocity distribution of those electrons. Knowing the remaining time in the simulation and the acceleration due to the electric field, the velocity distribution can be used to place these electrons into their final spatial bins (ignoring Coulomb repulsion on these short time scales). Additionally, as the electrons are placed into these bins, their average velocity is stored as well.

This simulation repeats for each time slice until the finish time, at which point the laser has essentially stopped creating electrons. At this time, the earliest fastest electrons will be a distance

$$z_{max} = v_{max}N\tau + \frac{eE_{DC}}{2m}(N\tau)^2 \quad (3.13)$$

away from the the photocathode and the the electrons created in the last slice will be at $z = 0$. By counting the electrons in each spatial bin and fitting to a Gaussian, we can determine $\sigma_z(0)$, the initial longitudinal spatial variance of the pulse. Taking a weighted average of the velocity of the electrons in each spatial bin and fitting to a linear function across the pulse (as defined by the AG model), we can determine the initial longitudinal velocity (momentum) chirp $\gamma_z(0)$. As seen in Figure 1, the shapes of the actual output compare well with the fitted functional form for both of these parameters for all reasonable ranges of field and laser pulse duration.

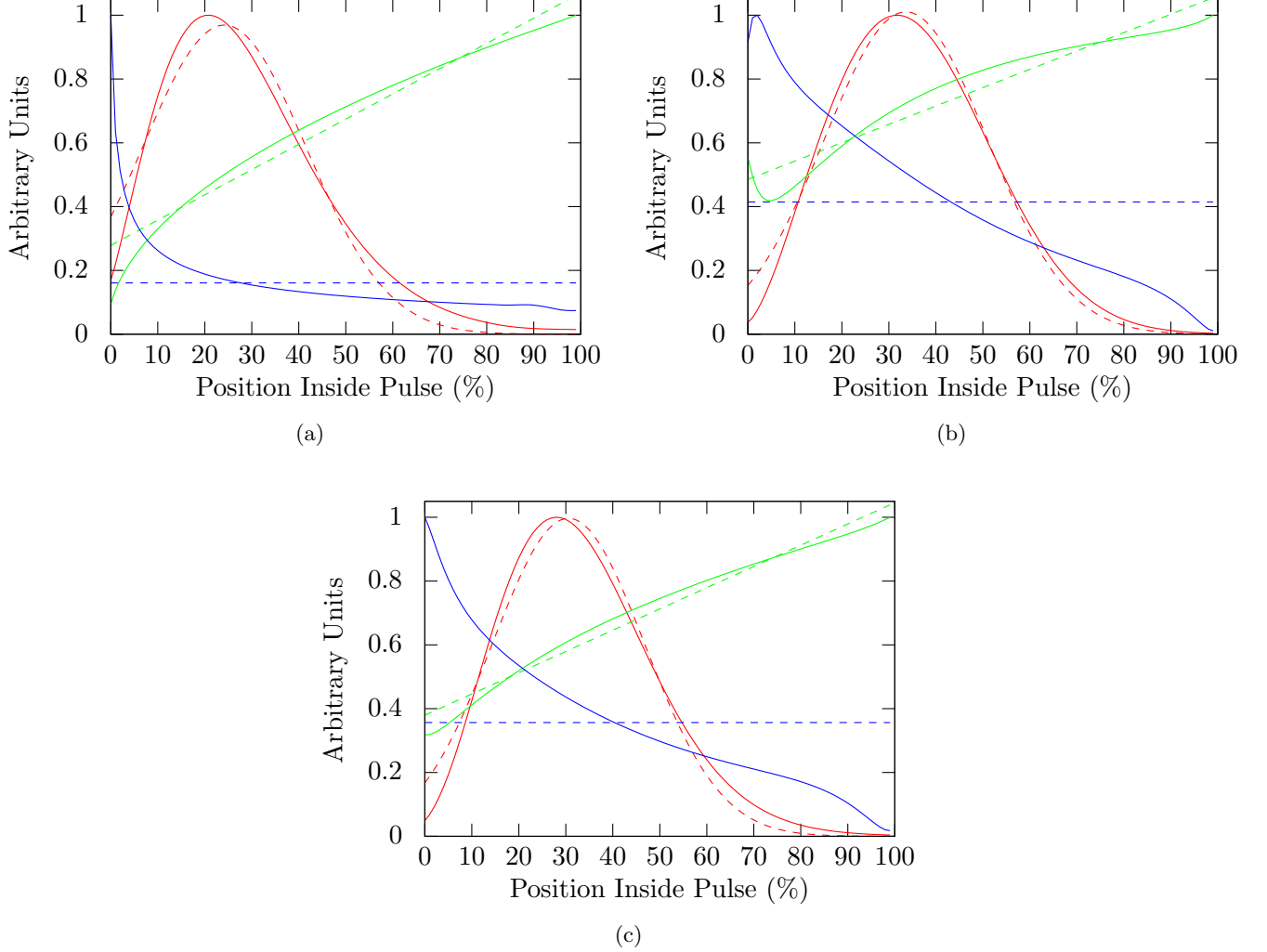


Figure 1: Comparison of the results of the bin model and AG model allowed functional forms for three different input parameters cases. Compared are: (a) the DC acceleration dominated case, (b) the photoemission energy dominated case, and (c) an intermediate case. For the Gaussian spatial distribution whose variance is σ_z (red) and the momentum chirp γ_z (green) the simulated data (solid) and the fit to the AG allowed form (dashed) are decently well matched in all cases. Unfortunately, the model only allows for a constant local momentum variance η_z (green) and in all but the extreme acceleration dominated case (a) the model cannot well represent the simulated data.

Finally, the velocity uncertainty in each bin can be computed, however, unlike the previous parameters, the AG model only allows for a constant value of $\eta_z(0)$, the local momentum variance across the pulse. Unfortunately, Figure 1 clearly demonstrates that the local momentum variance is not constant over the initial photo-generated electron bunch; in fact it varies by almost an order of magnitude over the $1/e^2$ maximum full-width of the electron bunch. The narrowest momentum distribution are clearly at the front of the bunch where only the earliest generated electrons with initial velocity near v_{max} initially reside; the largest distribution is at the back where the last electrons generated still haven't had time to separate from one another.

This limitation on functional form severely limits the accuracy with which a determined spatially constant value of $\eta_z(0)$ represents the actual distribution of momentum uncertainties computed by the binning model. The self-similar theory of Michalik and Sipe (70) is not equipped to handle such a variation as it assumes a constant η_z over the electron bunch; with a more realistic fit to the simulated initial data, the pulse would eventually evolve to be non-Gaussian.

3.2 Implications of Liouville's Theorem

One of the most well known theorems in physics (and mathematics) is Liouville's Theorem. This theorem can be summarized succinctly as a 'the total phase space of a system is conserved.' In the AG model the component phase-space products are simply $\sigma_\alpha \eta_\alpha$ where as before $\alpha = r, z$.

In fact it is easy to show that the AG model explicitly obeys the Liouville Theorem. To do so, consider the time derivative of these component phase-space products. Using Equation 2.30 it is easy to show that

$$\frac{d}{dt}(\sigma_\alpha \eta_\alpha) = \sigma_\alpha \frac{d\eta_\alpha}{dt} + \eta_\alpha \frac{d\sigma_\alpha}{dt} = 0, \quad (3.14)$$

and therefore we can define the per-simulation constants Γ_α as

$$\Gamma_\alpha^2 \equiv \sigma_\alpha \eta_\alpha = \text{Constant}. \quad (3.15)$$

Not only is this an interesting result, but it can be both instructive and computationally useful. By evaluating Γ_α at some time (presumably $t = 0$) and rewriting Equation 3.15 as $\eta_\alpha = \Gamma_\alpha^2 / \sigma_\alpha$, we can rewrite Equation 2.30 as

$$\frac{d\sigma_\alpha}{dt} = \frac{2\gamma_\alpha}{m} \quad (3.16a)$$

$$\frac{d\gamma_\alpha}{dt} = \frac{\Gamma_\alpha^2 + \gamma_\alpha^2}{\sigma_\alpha m} + \frac{Ne^2}{4\pi\epsilon_0} \frac{1}{6\sqrt{\sigma_\alpha\pi}} L_\alpha(\xi). \quad (3.16b)$$

These four equations now contain all of the information previously contained in six (Equation 2.30). Having fewer equations, and fewer mathematical operations, makes this set of equations much less computationally intensive. Further, when viewed in comparison to the chirps γ_α , one can now see that these Γ_α constants can be thought of as some minimum/intrinsic action of the pulse. This becomes apparent when noting that if a momentum chirp γ_α should

ever reach zero (e.g. as it does at the focal point of a lens) there is still a non-Coulombic term driving the $\frac{d\gamma_\alpha}{dt}$, as there surely must be when the local momentum variance η_α is not zero.

We note that, in the transverse directions (x), this is consistent with the definition of ‘coherent fluence’ employed by Reed *et al.* (86) for time-resolved electron microscopy and, of course, the transverse spatial emittance of an electron beam (46; 96). Additionally, though the AG model explicitly satisfies Liouville’s Theorem, there are cases where the pulse’s phase space product may change in a realistic system. This effect is called “emittance growth” and is most commonly seen in TEM as a result of aberrations in lens systems (78). As will be seen in Section 3.3.4, the AG model will, of necessity, only consider perfect lenses.

3.3 Formal Extension to Include Generic External Forces

Simulation of electron pulse propagation in UEM and modern UED apparatus (96; 102; 85) requires the ability to model electron-optical elements designed to control the three-dimensional space-charge and dispersion induced broadening of the pulse, and hence deliver electron pulses of the desired quality to the specimen. The Analytic Gaussian model as presented by Michalik and Sipe (see Chapter 2) is only useful for modeling free-space propagation. This is because there is no allowance for external forces, such as those imparted by the “optical” elements of an electron microscope column. In this section, I show that the AG model can be extended to include external forces on the pulse, such as the influence of magnetic electron lenses and RF pulse compression cavities (102; 103).

3.3.1 Mathematical Formulation of External Force Contribution

While the free-space AG model does not contain any external forces, it does include an internal force: the Coulomb force is included to model the repulsion of the pulse's electrons from each other. As this force is self-influencing, it is the major source of complexity in the model; indeed without this term, a complete analytic solutions is possible, which is identical to so-called ‘‘Gaussian optics’’ (70).

The internal Coulombic repulsion force enters the model in Equation 2.22. Since both potentials and integrals are linear, one may add additional potentials, so that it becomes

$$V(\vec{r} - \vec{r}') \rightarrow V^{int}(\vec{r} - \vec{r}') + \sum_k V_k^{ext}(\vec{r}). \quad (3.17)$$

In doing so, we rename the potential due to the internal repulsive Coulomb force V^{int} . Following these new terms through the derivation, we see that

$$\begin{aligned} \Phi(\vec{r}; t) &= \int d\vec{r}' \left(V^{int}(\vec{r} - \vec{r}') + \sum_k V_k^{ext}(\vec{r}) \right) n(\vec{r}'; t) \\ &= \int d\vec{r}' V^{int}(\vec{r} - \vec{r}') n(\vec{r}'; t) + \sum_k \int d\vec{r}' V_k^{ext}(\vec{r}) n(\vec{r}'; t) \\ &\equiv \Phi^{int}(\vec{r}; t) + \sum_k \Phi_k^{ext}(\vec{r}; t). \end{aligned} \quad (3.18)$$

Therefore each external force contributes an additional term defined as

$$\Phi_k^{ext}(\vec{r}; t) \equiv \int d\vec{r}' V_k^{ext}(\vec{r}) n(\vec{r}'; t). \quad (3.19)$$

These external terms are not self-influencing, and thus are not subject to the complexities of the internal Coulombic repulsion force. For consistency we have now defined $\Phi^{int}(\vec{r}; t)$ as the old $\Phi(\vec{r}; t)$, which results from the Coulomb force.

This new form of $\Phi(\vec{r}; t)$ can be substituted into the definition of K^{force} matrix (Equation 2.21), again in the basis defined in Equation 2.12, to give

$$\begin{aligned} K_{ij}^{force} &= \frac{1}{N} \int u_i u_j \frac{\partial f}{\partial \vec{p}} \frac{\partial}{\partial \vec{r}} \left(\Phi(\vec{r}; t) + \sum_k \Phi_k^{ext}(\vec{r}; t) \right) d\vec{r} d\vec{p} \\ &\equiv K_{ij}^{int} + \sum_k (K_k^{ext})_{ij}. \end{aligned} \quad (3.20)$$

Like the potential integrals, we are left with an additional matrix for each external force. Again, for consistency, we have defined K^{int} as the K matrix resulting from the internal Coulombic repulsion.

Noting that the spatial derivative of a potential is just the force, we can now define the matrix contributed by each external force as given by

$$K_{ij}^{ext} = \frac{1}{N} \iint u_i u_j \left[\frac{\partial}{\partial \vec{p}} f(\vec{r}, \vec{p}; t) \right] \cdot \vec{F}_{ext} d^3x d^3p. \quad (3.21)$$

Finally, the general form of Equation 2.19 for (possibly multiple) external force (\vec{F}_{ext}) contributions is now

$$\frac{\partial}{\partial t} A_{ij}^{-1} = K_{ij}^{flow} + K_{ij}^{int} + \sum K_{ij}^{ext}. \quad (3.22)$$

3.3.2 Constant External Forces

For constant static forces having no dependence in x , y , z , or t , one can readily show that there is no effect on the pulse propagation parameters σ_α , η_α , and γ_α . For example, consider an acceleration electric field $\vec{E} = -E\hat{z}$ such that electrons are accelerated in the positive z direction. The force is then $\vec{F}_{ext} = eE\hat{z}$, so that from Equation 3.21 we have

$$K_{ij}^{ext} = \frac{eE}{N} \int u_i u_j \left(\frac{p_z}{\eta_z} - \frac{\gamma_z z}{\sigma_z \eta_z} \right) f d^3x d^3p. \quad (3.23)$$

It is clear that no function of this form multiplying f , which is a Gaussian distribution, can avoid creating an odd integrand, and thus $K_{ij}^{ext} = 0$ for all i and j meaning that this static field has no effect on the parameters of the pulse. Of course, this is only true in the pulse frame, the frame of the simulation, where there is no total momentum and thus $\Delta E = (\Delta p)^2 / 2m$ is unchanged. In the lab frame however, where $\Delta E = p\Delta p/m$, there is an increase in the momentum spread, as the pulse now has the large momentum p imparted by the accelerating field.

3.3.3 Linear External Forces

For the case of a cylindrically symmetric perfect lens, or in the longitudinal direction a perfect RF compression element, with a parabolic potential, the external force is linear with distance from the center of the electron pulse:

$$\vec{F}_{ext} = -M_T r \hat{r} - M_z z \hat{z}. \quad (3.24)$$

Here, M_T and M_z characterize the strength of a lens or a compressor, respectively, and are chosen to be positive for focusing/compression elements. Substitution into the integral equation for the K^{ext} matrix elements,

$$\begin{aligned}
K_{ij}^{ext} &\equiv \frac{1}{N} \int u_i u_j (\vec{\nabla}_p f) \cdot \vec{F}_{ext} d^3 x d^3 p \\
&= \frac{1}{N} \int u_i u_j \left[x \left(\frac{p_x}{\eta_T} - \frac{\gamma_T x}{\sigma_T \eta_T} \right) + y \left(\frac{p_y}{\eta_T} - \frac{\gamma_T y}{\sigma_T \eta_T} \right) \right. \\
&\quad \left. + z \left(\frac{p_z}{\eta_z} - \frac{\gamma_z z}{\sigma_z \eta_z} \right) \right] f d^3 x d^3 p,
\end{aligned} \tag{3.25}$$

leads to the 6×6 matrix

$$K^{ext} = \begin{pmatrix} k_T^{lin} & 0 & 0 \\ 0 & k_T^{lin} & 0 \\ 0 & 0 & k_z^{lin} \end{pmatrix}, \tag{3.26}$$

where

$$k_\alpha^{lin} = \begin{pmatrix} 0 & M_\alpha \sigma_\alpha \\ M_\alpha \sigma_\alpha & 2M_\alpha \gamma_\alpha \end{pmatrix}. \tag{3.27}$$

which by Equation 2.18 this yields an additional term $M_\alpha \sigma_\alpha$ which is added to the original $\frac{d\gamma_\alpha}{dt}$ equation. This derivation has been for a single force, in practice however there may be multiple forces. Therefore if each force is labeled by f , Equation 3.16b may be restated as

$$\frac{d\gamma_\alpha}{dt} = \frac{\Gamma_\alpha^2 + \gamma_\alpha^2}{\sigma_\alpha m} + \frac{Ne^2}{4\pi\epsilon_0} \frac{1}{6\sqrt{\sigma_\alpha\pi}} L_\alpha(\xi) + \sigma_\alpha \sum_f M_\alpha^{\{f\}}. \tag{3.28}$$

Since these terms are only added to $\frac{d\gamma_\alpha}{dt}$, the analysis of Liouville’s Theorem, shown in Section 3.2, is unaffected: the *extended* AG model still explicitly satisfies Liouville’s Theorem.

3.3.4 Validity and Limitations

The presented extension to the AG model to include external forces acting on the electron pulse is valid only within the limits of the analytical method itself; in particular, its mean internal space-charge field and self-similar Gaussian approximations (70). As a result, we emphasize that the presented AG model extension is valid only for the action of linear forces (i.e., forces that have a linear dependence on distance in the pulse frame) on the electron pulse due to the model’s self-similar Gaussian approximation. Since nonlinear forces are not considered, “emittance growth” effects arising from imperfect lenses cannot be modeled (78). The inclusion of the action of nonlinear forces (e.g., due to higher-order space-charge effects, spherical magnetic lens aberrations, etc.) will require the use of more sophisticated electron pulse propagation models such as full particle tracking simulations.

It should also be noted that these analyses are performed in the non-relativistic limit, which is a reasonable approximation for the typical 20-200keV electron energies employed in UED and electron microscopy. Extension to include relativistic effects is conceptually straightforward using standard transformations between the laboratory and electron pulse reference frames.

Nonetheless, for free-space propagation, the AG model of charge bunch dynamics has already been shown to be very consistent with full Monte Carlo (i.e., particle tracking) simulations for a wide variety of electron pulse shapes (70; 72), including the uniform ellipsoid (63). This successful benchmarking is due primarily to the versatility of the AG model which results from

its use of transverse and longitudinal pulse position and momentum variances. Consequently, the AG approach is applicable to both the single electron per pulse limit (62), where momentum variances determine the pulse evolution and the model is exact (obeying Gaussian optics), and the high charge density limit in which space-charge effects dominate (63; 96; 25). It is this versatility combined with its computational efficiency that makes the presented extended AG model particularly suitable for rapid initial assessments of pulsed electron microscope column designs and electron pulse delivery systems in UED experiments. Verification of the validity (and determination of the limits) of the extended AG model will, of course, require future comparison with both experiment and more complete simulations of electron pulse propagation dynamics (e.g., full particle tracking models) that include nonlinear forces, for both the intra-pulse space-charge field and the description of aberrations in electron optics.

3.4 Extension to Include Magnetic Lenses, RF Cavities, and DC Accelerators

The mathematical formalism developed in Section 3.3 is only an abstract mechanism for including external forces. To model electron pulses traveling through realistic electron microscope columns, these abstract mechanisms must be developed further to properly describe each specific electron-optical element. In the following section, I demonstrate concrete applications of the extended AG model, including magnetic lenses, radio-frequency (RF) cavities (useful for both pulse compression (102) and acceleration (50)) and DC acceleration regions (i.e. electron gun dynamics).

3.4.1 Region of Influence

Of course, physical electron-optical elements occupy only a finite space in the column, and thus their influence on the pulse should be limited to a region near the element itself. To localize the mathematical result shown in Section 3.3, it is convenient to redefine a particular M_α to include a super-Gaussian envelope in z' , the position of the peak of the pulse in the lab frame;

$$M_\alpha \rightarrow M_\alpha \exp \left[- \left(\frac{z' - z'_{lens}}{L_{lens}/2} \right)^{2n} \right], \quad (3.29)$$

where z'_{lens} is the position of the center of the lens, L_{lens} is the axial length of the lens and n is the super-Gaussian order parameter. The order parameter defines the “sharpness” of the edge of the region of influence with integer values ranging from 1 (a simple Gaussian) through ∞ (a top-hat). We connect z' to t through v_0 , the speed of the pulse; the kinematic equations are simply defined for the position of the peak of the pulse.

3.4.2 Magnetic Lenses

A simple magnetic lens is just a solenoid whose axis is collinear with the axis of the microscope column. As electrons propagate through the solenoid the fringing magnetic field imparts an azimuthal velocity. This “tumbling” around the axis, along with the axial magnetic field, is what causes the inward-directed force.

The full description of the motion of an electron (in cylindrical coordinates r, θ, z) in an azimuthally symmetric magnetic field ($\vec{B} = B_r \hat{r} + B_z \hat{z}$) is easily derived (37),

$$m\ddot{r} = -eB_z r \dot{\theta} + mr\dot{\theta}^2 \quad (3.30a)$$

$$\frac{d}{dt}(mr^2\dot{\theta}) = er\dot{r}B_z - erB_r\dot{z} \quad (3.30b)$$

$$m\ddot{z} = eB_r r \dot{\theta}, \quad (3.30c)$$

where each dot denotes a time derivative. Attempting to further separate these equations quickly highlights the tightly coupled nature of the motion of the electron in this system. Compounding the problem, the full description of the off-axis field of a real (non-infinite) air-core solenoid is also surprisingly complicated. Montgomery and Terrell (75) provide a full treatment for many lens configurations, including a tractable treatment for a single current loop of radius a , again in cylindrical coordinates,

$$\frac{B_z}{\mu} = H_z = \frac{2I}{\sqrt{Q}} \left(F(k) + \frac{a^2 - r^2 - z^2}{(1 - k^2)Q} E(k) \right) \quad (3.31a)$$

$$\frac{B_r}{\mu} = H_r = \frac{2I}{\sqrt{Q}} \left(-F(k) + \frac{a^2 + r^2 + z^2}{(1 - k^2)Q} E(k) \right) \quad (3.31b)$$

$$Q \equiv (a + r)^2 + z^2 \quad (3.31c)$$

$$k \equiv \sqrt{4ar/Q}, \quad (3.31d)$$

where μ is the local magnetic permeability, H is the auxiliary field, and $F(k)$ and $E(k)$ are the complete elliptic integrals of the first and second kind respectively. In the vacuum, μ is simply

the usual free space permeability μ_0 ; in Section 6.4, we will see how this permeability can be used to improve the performance of magnetic lenses. An even more accurate solenoid can be modeled by appropriately summing the fields of many such loops.

For the AG model, a magnetic lens may be modeled using one linear force contribution in the transverse (τ) direction. Unfortunately, it is not practical to write an analytic form of the magnitude of this term. As seen in Equation 3.31 the field distribution is surprisingly complicated to describe and the “lensing” action is in fact a compound force (first rotating the beam, then lensing). I have found that in practice, characterizing a specific magnetic lens ($M_T^{mag}(I)$ where I is the current in the magnetic lens) is much easier than attempting to find a generic functional form. This may be done in comparison to either experimental data or, as shown in Figure 2, to numerical simulations based on Equation 3.31.

For localizing the region of influence of the lens, I have generally modeled a thin magnetic lens as having a super-Gaussian order value $n = 1$, a simple Gaussian; of course this may depend on the specifics of the lens. To simulate the effect of magnetic lenses in a UEM by the extended AG model, for each magnetic lens, one adds a term like

$$M_T^{mag} = M_T^{mag}(I) \exp \left[- \left(\frac{z' - z'_{mag}}{L_{mag}/2} \right)^2 \right], \quad (3.32)$$

to the set of M_T parameters, where z'_{mag} and L_{mag} are the position and length of the lens in question respectively.

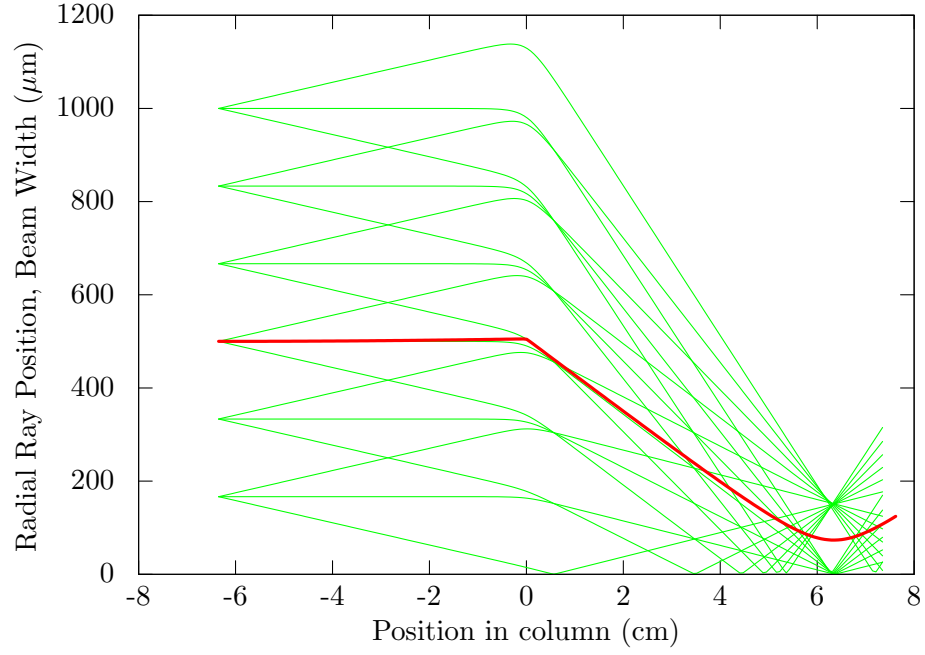


Figure 2: Comparison of electron rays tracked kinematically through a realistic magnetic lens simulation (green) and an AG model simulation of a Gaussian electron beam (red) of a similar HW1/eM beam width $w = 500\mu\text{m}$.

Figure 2 shows electron rays tracked kinematically (by employing Equation 3.30) through a realistic magnetic lens simulation (shown in green). The kinematic model employs ten individual current loops generating magnetic fields described by Equation 3.31; these loops occupy a total length of $635\mu\text{m}$ at position $z = 0$. These loops each carry a current of 45A ; this approximates a more realistic stack of 10 loops carrying 4.5A , thus simulating a 100 turn solenoid in a 10×10 array. Each ray bunch consists of one ray parallel to the axis of propagation and one each having a longitudinal velocity of 1×10^8 m/s and an inward or outward transverse velocity related to an excess photoemission energy $\Delta E \approx 0.1\text{eV}$. The bunches are distributed evenly from $r = 0$ to $r = 1\text{mm}$. These are compared with an AG model simulation of a Gaussian electron beam of HW1/eM beam width $w = 500\mu\text{m}$ having an initial transverse momentum variance associated with ΔE .

The AG model very accurately mimics the behavior of the kinematic model for an appropriate choice of the free parameter M_T^{mag} . In fact, when the rays are weighted by a Gaussian of width w the minimum “radius” of the beam is $100\mu\text{m}$, while the AG model has a minimum HW1/eM width of $73\mu\text{m}$. (The kinematic model actually overestimates the width as there are two rays at the outer convergence zone for every one which converges at the axis.)

3.4.3 RF Cavities

In the longitudinal (z) direction, a resonant radio-frequency (RF) cavity can be used in a UEM column or UED experiment (102; 38) to act as a pulse compression or ‘temporal focusing’ element. The model of the RF cavity is different from the magnetic lens in two distinct ways. First, the RF cavity contains several different fields and thus contributes several different linear

force terms to the overall equation set. Second, though there are more terms, their magnitudes are easily connected to the physical characteristics of the cavity.

Although there are many possible resonant cavity structures (102; 44), for simplicity, this analysis will consider only the evacuated cylindrical (or ‘pillbox’) TM_{010} cavity for which the electrons propagate down the axis (38; 44). The known mathematical forms of the electric and magnetic components of this resonant mode together with a super-Gaussian envelope function (Equation 3.29) allow the three main effects of a pill-box RF cavity element on the electron pulse to be described within the approximation of the linear force extension to the AG model: the primary action of the pulse compression (or acceleration and expansion dependent upon the relative RF phase), and the transverse lens effects due to the magnetic component of the TM_{010} resonance and the electric RF cavity fringe fields at its entrance and exit apertures (50).

The spatial dependence of the axial RF electric field experienced by the electron pulse in a TM_{010} cavity of radius a may be written as

$$E(r, z, z') = E_0 \sin \left(\frac{\Omega(z' - z)}{v_0} + \phi \right) J_0 \left(\frac{kr}{a} \right), \quad (3.33)$$

where E_0 is the oscillating field amplitude, Ω is the RF frequency and ϕ is a phase factor determining whether the RF cavity acts as a pulse compressor ($\phi \approx 0$) or an electron accelerator ($\phi \approx \pm\pi/2$). The coordinate z' describes the position of the center of the pulse in the RF cavity, which extends from $z' = -d/2$ to $z' = d/2$, and z is the position of any electron in the pulse

with respect to the center of the pulse. For the TM_{010} oscillation mode, the RF frequency is given by

$$\Omega = 2.405 \frac{c}{a}, \quad (3.34)$$

where c is the speed of light in a vacuum and 2.405 is the first zero of the J_0 Bessel function.

For the usual case of a spatially compact electron pulse with respect to the dimension of the RF cavity (i.e., $\Omega z \ll v_0$ and $\sqrt{\sigma_T} \ll a$), Equation 3.33 can be rewritten as

$$E(r, z, z') = E_0 \left[\sin \left(\frac{\Omega z'}{v_0} + \phi \right) - \frac{\Omega z}{v_0} \cos \left(\frac{\Omega z'}{v_0} + \phi \right) \right], \quad (3.35)$$

which demonstrates that the RF cavity acts both as a pulse acceleration (first term on RHS of Equation 3.35) and a pulse compression or expansion (second term on RHS of Equation 3.35) device. The linear term (second) then gives the desired form (see Equation 3.24) for the force manipulating the temporal dynamics and characteristics during electron pulse compression;

$$F_{z,RF}^{linear} = - \left[\frac{e\Omega E_0}{v_0} \cos \left(\frac{\Omega z'}{v_0} + \phi \right) \right] z \hat{z}. \quad (3.36)$$

By considering the impulse exerted by the RF cavity field on the electrons in the pulse, it is straightforward to show that pulse compression (when $\phi = 0$) is maximized for $\Omega d / (2v_0) = \pi/2$; that is, the time of flight of the electron pulse through the RF cavity of length d is equal to half the RF period. Such a calculation assumes that the pulse velocity v_0 is constant; so that, the condition that $\phi = 0$ when the pulse is at the center of the RF cavity (i.e., when the pulse is at

$z' = 0$) is readily met. As suggested by the acceleration term in Equation 3.35, this is only a good approximation if the RF field amplitude E_0 is sufficiently small to not affect the velocity of the peak of the pulse as it propagates through the cavity. As a result, in practice, the phase ϕ of the RF field is adjusted to optimize the performance of the cavity.

The two main effects contributing to the transverse lens of a TM₀₁₀-mode RF cavity, its magnetic field component and electric fringe field aperture effects, may also be included within the linear force approximation. The azimuthal magnetic component of the resonant mode oscillates 90° out of phase with the electric component and with a J₁ Bessel radial form; i.e., $J_1(kr/a) \sim kr/a$ for small r . Symmetry and Gauss' Law dictate that in the vicinity of the axial center of the entrance and exit apertures of the RF cavity there exists a radial component of the oscillating electric field determined by $E_r = -(r/2)(\partial E_z/\partial z)_{r=0}$ (50), where the form of the axial electric field for TM₀₁₀ oscillation (Equation 3.33) implies that, in the context of this analysis, its axial gradient is solely dependent upon the envelope function for the RF cavity (Equation 3.29). In practice, of course, the exact form of $E_r(z)$ is strongly tied to the size and shape of the RF cavity apertures (see for example 1½-cell RF photo-gun designs (69)). For the case of an evacuated cavity, these two contributions result in a net force,

$$F_{r,RF} = eE_0 \left[\frac{v_0\Omega}{c^2} \cos\left(\frac{\Omega z'}{v_0} + \phi\right) + \frac{2n}{d} \left(\frac{z' - z'_{RF}}{d/2}\right)^{2n-1} \sin\left(\frac{\Omega z'}{v_0} + \phi\right) \right] r\hat{r}. \quad (3.37)$$

In obtaining Equation 3.37, which is also of the form for use in Equation 3.24, we have again used an arbitrary super-Gaussian of order n as a region of influence envelope (see Equation 3.29)

with $L_{RF} \equiv d$, the RF cavity length. As will be seen in Section 4.4, under the pulse compression conditions ($\phi = 0$ when the pulse is at $z' = 0$), both effects are defocussing for the electron pulse and the magnetic contribution is generally smaller than the transverse lenses associated with the RF cavity apertures when $d = \pi v_0/\Omega$ (50), even though its magnitude is maximized for $\phi = 0$. Other effects, such as magnetic fringe field aperture effects, could also be included, but are significantly weaker.

To summarize, the additional terms which are added to model the internal pulse dynamics arising from a single TM_{010} -mode cylindrical RF cavity are

$$M_z^{RF} = \left[\frac{e\Omega E_0}{v_0} \cos\left(\frac{\Omega z'}{v_0} + \phi\right) \right] \exp\left[-\left(\frac{z' - z'_{RF}}{L_{RF}/2}\right)^2\right] \quad (3.38)$$

$$M_T^{RF} = eE_0 \left[\frac{v_0\Omega}{c^2} \cos\left(\frac{\Omega z'}{v_0} + \phi\right) + \frac{2n}{L_{RF}} \left(\frac{z' - z'_{RF}}{L_{RF}/2}\right)^{2n-1} \right. \\ \left. \times \sin\left(\frac{\Omega z'}{v_0} + \phi\right) \right] \exp\left[-\left(\frac{z' - z'_{RF}}{L_{RF}/2}\right)^2\right]. \quad (3.39)$$

Additionally, since an RF cavity can act as a pulse accelerator (as seen in the leading term of Equation 3.35) an additional force term

$$F_z^{RF} = eE_0 \sin\left(\frac{\Omega z'}{v_0} + \phi\right) \exp\left[-\left(\frac{z' - z'_{RF}}{L_{RF}/2}\right)^2\right], \quad (3.40)$$

should be added to the equation of motion governing the propagation of the pulse down the column.

3.4.4 Acceleration Region

In the acceleration region of a UEM column, a constant electric field is applied to the newly created electron pulse, increasing its velocity until it achieves its ultimate velocity just upon leaving the region at the anode aperture. As seen in Section 3.3.2, this constant electric field does not affect the intrapulse dynamics, however the distortion in the electric field near this aperture causes the anode itself to act as a negative transverse lens. Additionally, the longitudinal electric field strength sharply decreases near the anode. As the front of the pulse sees this change before the back, this changing field also acts as a pulse compression element.

Since the aforementioned effects are localized in the area very near the anode, the following analysis is only asserted for pulses that are of approximately the same length as the acceleration region or shorter. This assumption is very reasonable for UEM and for some of the shorter-pulse DTEM systems. Though these effects are expected for longer pulses, they are unlikely to be predominant factors in the dynamics.

To model an acceleration region, one must assume a form for the accelerating field. From that form one may derive the terms governing the pulse dynamics. Initially, assume that the on-axis field is purely in the longitudinal direction, which may be thought of as an implication of radial symmetry. Mathematically, that is

$$\vec{F}(r' = 0, z') = F_z(0, z')\hat{z} = eE_z(0, z')\hat{z}, \quad (3.41)$$

where as before, the primed coordinates are the location of the center of the pulse.

To first model the longitudinal (compression) action at the anode, consider electrons that are a distance z ahead or behind of the center of the pulse and so feel a slightly different force,

$$F_z(0, z' - z) \approx F_z(0, z') + \frac{\partial F_z}{\partial z'} z, \quad (3.42)$$

Again, the constant leading term does not contribute to the intrapulse dynamic, however the second term is of the proper form to say that in this region the anode's longitudinal compression strength M_z is given by

$$M_z = \frac{\partial F_z}{\partial z'} = e \frac{\partial E_z}{\partial z'}. \quad (3.43)$$

To model the radial action (negative transverse lensing), we can expand the radial force F_r for electrons that are a distance r radially outward from the center of the pulse,

$$F_r(r, z') \approx F_r(0, z') + \frac{\partial F_r}{\partial r'} r. \quad (3.44)$$

Without an analytic form for F , we can appeal to Gauss' law (in absence of external charge),

$$\frac{\partial F_x}{\partial x'} + \frac{\partial F_y}{\partial y'} + \frac{\partial F_z}{\partial z'} = 2 \frac{\partial F_T}{\partial r'} + \frac{\partial F_z}{\partial z'} = 0 \quad (3.45)$$

$$\Rightarrow \frac{\partial F_T}{\partial r'} = -\frac{1}{2} \frac{\partial F_z}{\partial z'}, \quad (3.46)$$

to see that the transverse lens strength M_T from the anode is simply,

$$M_T = -\frac{1}{2} \frac{\partial F_z}{\partial z'}. \quad (3.47)$$

We may choose to assume that the on-axis field is defined as a smoothed step down function

$$F_z(0, z') = \frac{eV}{2z'_A} \left(1 - \tanh \left(\frac{z' - z'_A}{z'_A/s} \right) \right), \quad (3.48)$$

where V is the accelerating potential, z'_A is the position of the anode (the cathode assumed to be at $z' = 0$) and s is a constant quantifying the “sharpness” of the fall-off of the electric field. Indeed, this form is analogous to the super-Gaussian envelope (Equation 3.29), however it is open ended on the cathode side, which is necessary for the electrons to be accelerated away from the photocathode. Given this form the “lensing” strengths are then

$$M_T = -\frac{eVs}{4z_A'^2} \operatorname{sech}^2 \left(\frac{z' - z'_A}{z'_A/s} \right) \quad (3.49)$$

$$M_z = \frac{eVs}{2z_A'^2} \operatorname{sech}^2 \left(\frac{z' - z'_A}{z'_A/s} \right). \quad (3.50)$$

As with the RF cavity, one needs to include the on-axis force (Equation 3.48) in the overall pulse propagation kinematics.

Figure 3 shows an example acceleration region for three values of the “sharpness” s . What is clear from this figure is that the dynamics are not highly coupled to the value of this hard-to-quantify parameter. For all values of s the divergence of the beam is equal (though the size may vary slightly). Interestingly the length of the pulse is stabilized on exiting the anode, coming very nearly to a constant length (neither expanding nor contracting). This effect is due to the slower electrons remaining in the cavity longer and thus receiving an additional kick,

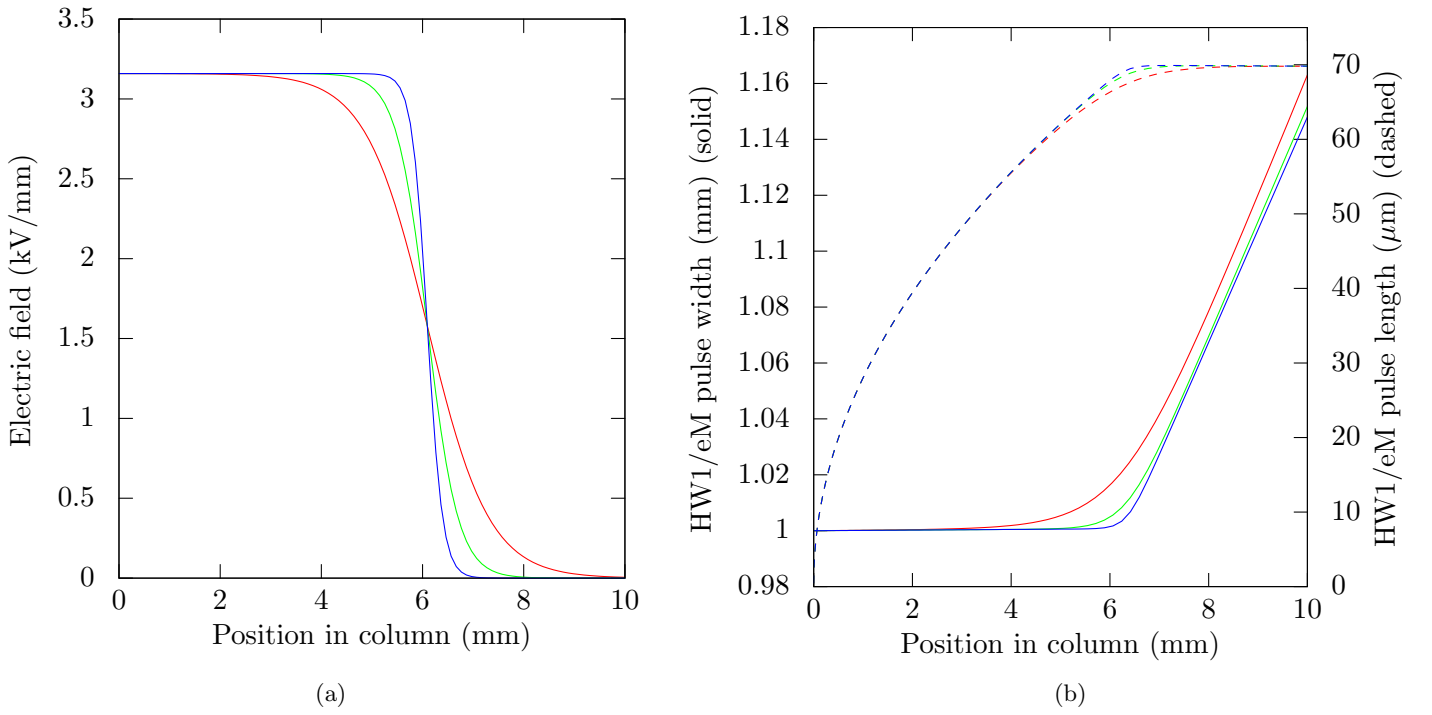


Figure 3: An example of a tanh form acceleration region (overall length 6.35mm) for three different “sharpness” values. The colored electric fields in figure (a) correspond to the pulse width (solid) and length (dashed) in figure (b). This form is compared to FEM simulated electric field data in Figure 19.

as described in (102). This longitudinal electric field shape is compared to the electric field computed by finite-element (FEM) simulations of our acceleration cavity in Section 6.3.

3.5 Implementation

The model presented in this chapter was initially implemented in Wolfram’s Mathematica. While this implementation provided the results needed, it was inflexible and overly confusing. The limitations of the Mathematica language precluded abstracting the model sufficiently to cover all common use cases.

Recently the model was rewritten in Perl, and is called `Physics::UEMColumn`. Perl is a dynamic scripting language known for its versatility and flexibility. In this implementation, the model is implemented as a decoupled set of high-level object-oriented classes.

`Physics::UEMColumn` has been released as open source software under the terms of the Artistic License (a derivative of the GNU General Public License), which allows for free use of the software. The current state of development of the simulation toolkit is publicly available at <https://github.com/jberger/Physics-UEMColumn>. Releases of the toolkit are available via the Comprehensive Perl Archive Network (CPAN), which is a central repository of software developed for Perl, a standard tool for the language. The CPAN has several tracker sites, see for example <https://metacpan.org/module/Physics::UEMColumn>.

A simulation script is composed of creating instances of the classes that represent the column, the pulse, electron-optical elements like magnetic lenses and RF cavities. These objects act as containers for the information about the physical object that they represent. Further they manage programmatic tasks related to those objects. For example, electron-optical ele-

ment objects manage the Gaussian region-of-influence (Equation 3.29) and calculate the force that their fields apply to the pulse. While the pulse object may be created manually, the toolkit contains the class `Physics::UEMColumn::Photocathode` which implements the simple initial conditions described in Section 3.1. These objects are managed by a central “simulation” class (called `Physics::UEMColumn`) which handles the time evolution of the system. This arrangement allows for clean, manageable and extensible code.

Many scripts which use `Physics::UEMColumn` were needed to generate data and figures used for the preparation of this thesis. I have included most of them in the source repository which is available at <https://github.com/jberger/Thesis>. In Appendix A, I present the simulation scripts used to create Figure 5, Figure 6 and Figure 9, as examples of this implementation.

Additionally, a development version of the bin model presented in Section 3.1.2 is available at <https://github.com/jberger/Physics-Photoemission>. Once I am sufficiently confident in its implementation, and more importantly its veracity, I intend to release it to the CPAN as well, most likely under the name `Physics::Photoemission`. This module depends on the much larger Perl project PDL (<http://pdl.perl.org>), a matrix-oriented numerical library, making it slightly more difficult to install, however the speed and implementational simplicity benefit added by that dependency is marked. Of particular interest to users of `Physics::UEMColumn`, `Physics::Photoemission` also includes a subclass of `Physics::UEMColumn::Photocathode` which uses this binning model to generate the pulse’s z direction initial conditions.

CHAPTER 4

MODEL RESULTS, PREDICTIONS AND IMPLICATIONS

In Chapters 2 and 3, I have introduced the extended Analytic Gaussian model. In this chapter, I use this model to make general observations about pulse propagation for Ultrafast Electron Microscopy.

The examples presented will each use one of two initialization schemes. The first represents an idealized pulse which is not generated by photocathode and then accelerated, but rather springs into existence at its initial position with its velocity already established. This type of pulse is useful to demonstrate general pulse dynamics or the ideal influence of electron-optical elements independent of the pulse's creation conditions. Simulations using pulses of this type will specify an initial velocity v_0 (or equivalent acceleration voltage V_{DC}), an excess photoemission energy ΔE , and HW1/eM dimensions; width w_T and duration τ or length $w_z = v_0\tau$. The width and length will be used directly to calculate initial spatial variances σ_α . Both momentum chirp terms, γ_α , will be initially zero, but since pulses must still be subject to Liouville's Theorem (discussed in Section 3.2), Equation 3.12 will still be used to calculate meaningful local momentum widths η_α . This idealization only applies to the initialization, therefore these pulses will still be subject to intrinsic pulse broadening and internal space-charge repulsion which might cause pulse expansion before or during the demonstration, especially for high charge densities.

Other examples in this section will require a more realistic pulse resulting from photoemission and subsequent acceleration. Indeed, some of the examples shown with the idealistic pulses display markedly different behavior in light of these realistic conditions. Simulations using pulses of this type will specify the HW1/eM width and duration of the laser, the length and voltage of the acceleration region, and an excess photoemission energy. In these cases, all initial parameters will be calculated from Equation 3.12. The acceleration process, and more specifically the anode (see Section 3.4.4), will have an impact on the beam dynamics which will be evident in the pulse's evolution.

4.1 Effect of Pulse Eccentricity on Dynamics

The initial ‘space-time’ eccentricity (defined in Equation 2.27),

$$\xi(0) = \sqrt{\frac{\sigma_z(0)}{\sigma_T(0)}} = \frac{w_z(0)}{w_T(0)} = \frac{v_0\tau(0)}{w_T(0)}, \quad (4.1)$$

of the photo-generated electron pulse plays a major role in the bunch propagation dynamics, particularly when space-charge effects dominate. Figure 4 illustrates the typical dynamics of initially spherical ($\xi(0) = 1$), oblate or ‘disk-like’ ($\xi(0) < 1$), and prolate or ‘cigar-like’ ($\xi(0) > 1$) pulses. This simulation uses the idealized pulse conditions described above, where the initial bunch dimensions are given by the ellipticities $\xi(0) = \{1/3, 1, 3\}$ and in each case the product of the initial HW1/eM bunch widths $w_T^2 w_z = 1\text{mm}^3$. Pulses used in Figure 4(a) have just one electron per pulse (i.e. $N = 10^0$), while Figure 4(b) have a much higher $N = 10^6$ electrons in the bunch. Since the initial pulse volume is consistent between all runs, initial peak pulse

charge density is six orders of magnitude greater in Figure 4(b) than in Figure 4(a). The pulse velocity is $v_0 \approx c/3$, which is equivalent to a DC photogun with $V_{DC} = 30\text{kV}$.

The bunch propagation dynamics for the negligible pulse charge density case shown in Figure 4(a) display the trends expected from the initial photoemission conditions. In particular, in the initially spherical case ($\xi(0) = 1$), the transverse bunch width $\sqrt{2\sigma_T}$ expands approximately twice as rapidly as the longitudinal length $\sqrt{2\sigma_z}$ due to the factor of two difference in the initial momentum variances Δp_α and the artificially zero initial pulse chirp. Naturally, for initially non-spherical electron bunches, the pulse propagation model also shows that the relative bunch broadening $\sqrt{\sigma_\alpha/\sigma_\alpha(0)}$ for comparable η_α is greatest for the smallest initial $\sigma_\alpha(0)$; that is both oblate and prolate pulses are initially driven towards the spherical regime. In all cases, this intrinsic electron pulse broadening due to non-zero η_α generates a momentum chirp across the electron bunch; in the longitudinal dimension the faster electrons, those photoemitted with larger excess energy, lead the slower electrons.

For an electron pulse with a higher initial space-charge density, intra-pulse Coulomb effects may dominate the propagation dynamics. Figure 4(b), shows the predicted time evolution dynamics of electron pulses with the same initial size and photoemission conditions as Figure 4(a), but with $N = 10^6$ electrons — the number required for single-shot diffraction pattern measurements in a DTEM (17; 12). The significant influence of space-charge effects for the higher initial peak pulse charge density is clearly evident. In the spherical case, space-charge induced bunch broadening begins to overwhelm the initial difference between η_T and η_z , producing a more uniform three-dimensional ‘Coulomb explosion’ of the electron pulse with the overall

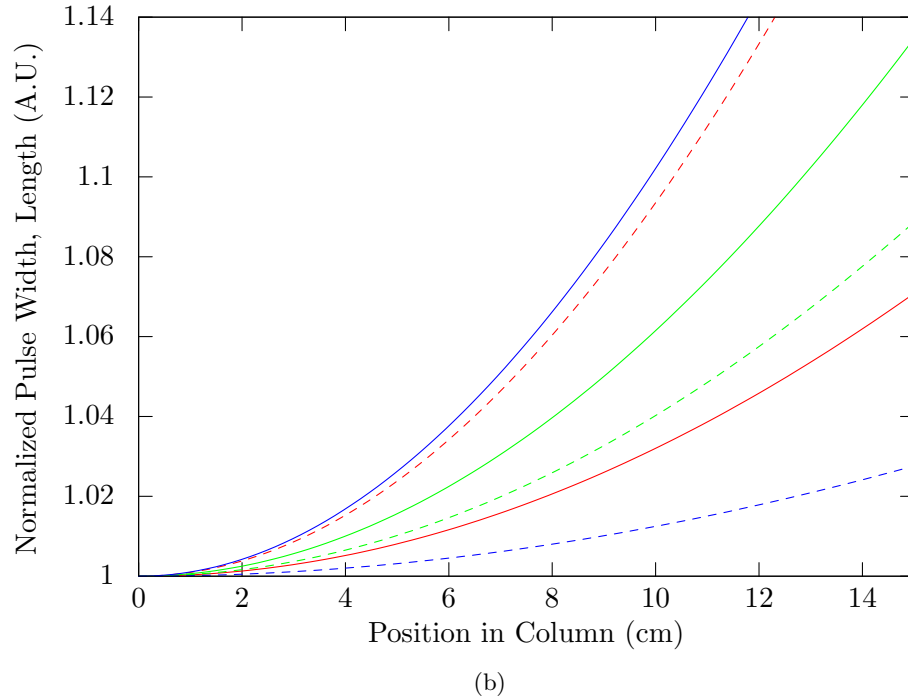
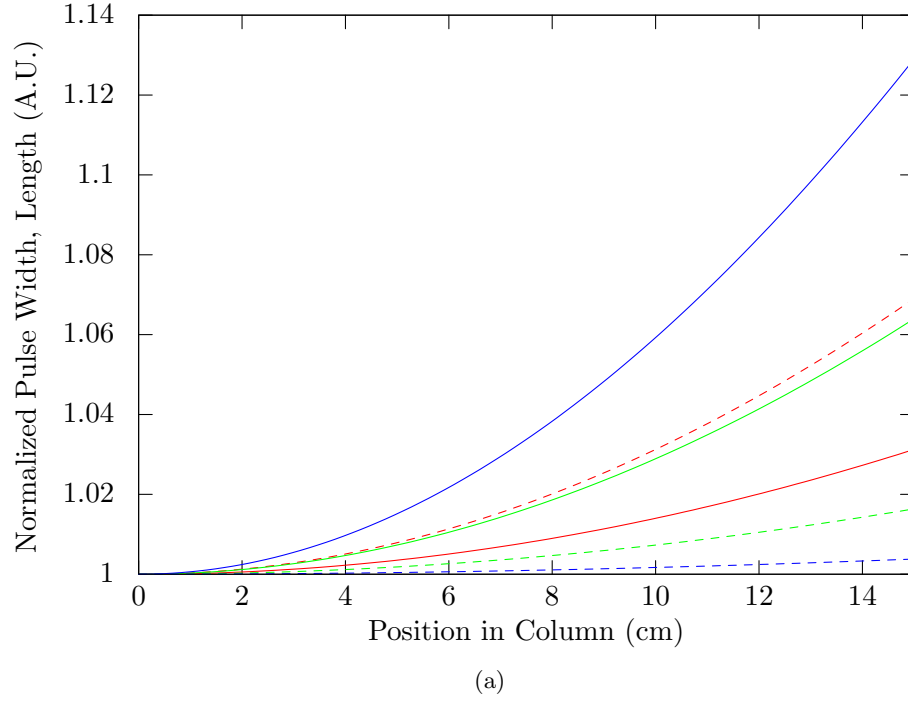


Figure 4: Transverse (solid) and longitudinal (dashed) dynamics of three example pulses for three length/width ratios (ξ). The red lines represent a oblate pulse (a “pancake”) with $\xi = 1/3$, green lines for a spherical pulse with $\xi = 1$, and blue for an prolate pulse (a “cigar”) having $\xi = 3$. The pulses shown in (a) all have total charge $N = 1$, while in (b) the pulses have $N = 10^6$.

bunch broadening rate much greater than that for $N = 10^0$ (Figure 4(a)). For $\xi(0) > 1$ (or $\xi(0) < 1$), the smaller initial transverse (longitudinal) bunch dimension experiences the greatest relative expansion in free-space propagation. This is to be expected, because the initial η_α are non-zero (but comparable in magnitude) while Coulomb effects will produce the greatest differential pulse broadening in the dimension with the largest internal space-charge field (i.e., the dimension with the largest electrostatic potential gradient). The initial impulse induced by the strong space-charge field then provides for continued linear expansion (in time), resulting in a linear pulse chirp in the dimension associated with the smallest initial HW1/eM bunch width (70; 17) $\sqrt{2\sigma_\alpha(0)}$.

The data presented in Figure 4 using the AG model of Michalik and Sipe (70) are entirely consistent with prior works (85; 96). In femtosecond UED experiments, significant efforts are made to offset space-charge induced temporal (longitudinal, z) pulse broadening by reducing the time of flight from the gun photocathode to the sample (96; 86). Moreover, efforts are now underway to compensate for temporal electron pulse broadening using RF cavity pulse compression techniques (102). In UEM, employing a standard retro-fitted electron microscope column driven by MHz repetition-rate sub-picosecond lasers (62), deleterious space-charge effects have obliged operation in the ~ 1 electron/pulse regime to maintain high spatial resolution. Even for nanosecond DTEM (the extreme prolate pulse case, $\xi \gg 1$), transverse space-charge induced beam broadening has necessitated the insertion of an additional magnetic electron lens in a microscope column to allow more efficient delivery of electrons to the specimen when $N > 10^6$ (56). In this thesis, however, I will often restrict the discussion to ultrashort (ps

and sub-ps) electron pulses which (i) allow for the temporal resolution of fundamental events occurring on ultrafast time scales in materials science, biology and chemistry (51) and (ii) can be easily generated in the oblate regime ($\xi < 1$) where transverse bunch broadening effects are minimized (Figure 4)(enabling more efficient beam propagation) and RF cavities can be used to compensate and reverse longitudinal (temporal) pulse broadening (103).

4.2 Effect of Space Charge on Dynamics

As seen in Section 4.1, at low pulse charge densities, the propagation dynamics should be largely determined by the effects associated with the intrinsic geometric pulse broadening; for most photoemission processes this is related to the excess photoemission energy ΔE . On the other hand, space-charge effects are expected to dominate at large pulse charge densities. A full analysis of how high the charge density may be before deleterious space-charge become unmanageable would be a sizable task. While much discussion could be had on the degree of distortion allowable, as well as considerations of the initial shape of the pulse and length, and arrangement of the column and its constituent elements, a certain amount of intuition can be gained simply by considering a progressive series of examples.

The expected trend is evident in Figure 5 which presents the predicted HW1/eM pulse width $\sqrt{2\sigma_T}$ (solid line) and longitudinal length $\sqrt{2\sigma_z}$ (dashed line) after a propagation distance of 15cm as a function of the number of electrons in the pulse. Once again, this simulation employs the idealistic pulse described earlier, starting with a velocity of $c/3$ where c is the speed of light in a vacuum (1.5ns total propagation time), initial width $w_T = 1$ mm, HW1/eM pulse duration 1 ps ($w_z = 0.1$ mm), and an excess photoemission energy $\Delta E = 0.5$ eV. For these conditions,

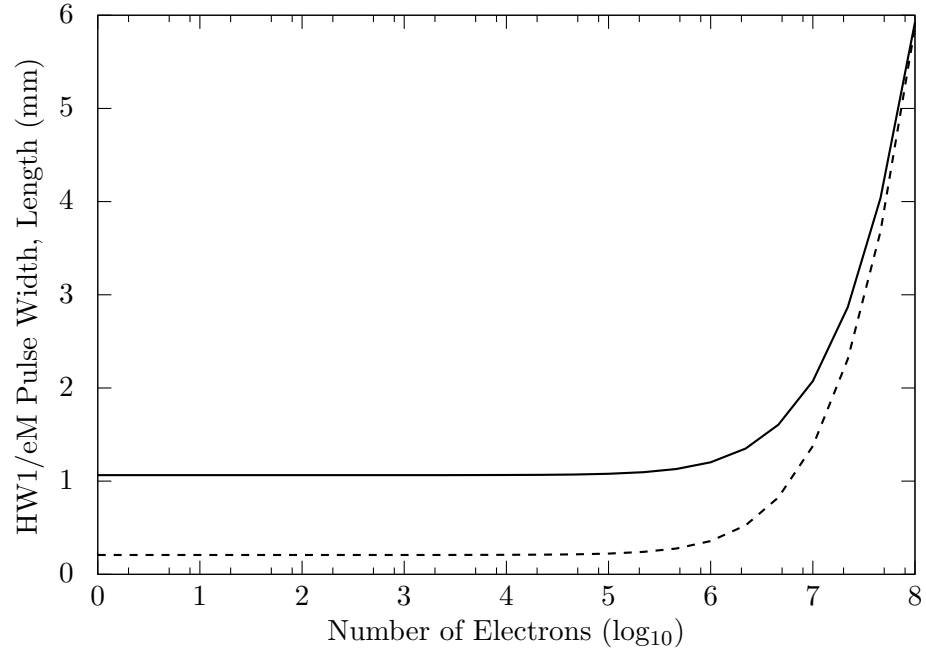


Figure 5: The final HW1/eM pulse width (solid) and length (dashed) after a 15 cm propagation. Pulses are initially similar except for the number of electrons in the pulse, each having 1 mm (HW1/eM) width and 1 ps in duration traveling at $c/3$ with 0.5eV excess photoemission energy.

that are used to isolate the behavior of a propagating pulse from its creation environment, the simulations clearly indicate that both the electron beam width and length at the end of the simulation will remain unchanged below about 10^5 electrons/pulse; that is, global space-charge effects only significantly influence the pulse propagation for pulses having more than 10^5 electrons/pulse. In the absence of space-charge effects, the presented oblate shaped pulses should be maintained as such during free-space propagation, because the initial values of the electron pulse's divergence and temporal broadening rate are both proportional to $\Delta E^{1/2}$ but not to N .

In this example, as the number of electrons/pulse increases beyond 10^6 , both the pulse's final length and width rapidly increase. The model predicts that space-charge effects produce a spherical charge distribution of approximately five times larger width at 10^8 electrons/pulse for these conditions. As noted in Section 4.1, pulses under the influence of the internal space-charge field expand preferentially in the dimension that was smallest initially; this causes the pulse to initially trend towards being spherical.

Figure 5 employed the idealistic conditions specifically to isolate the behavior of an “ideal” pulse which is independent of its creation environment. Of course in a more realistic system, the electron pulse is generated from a photocathode and then accelerated. Now that we have seen how the ideal case behaves, it is important to consider the interesting role that these more realistic factors play in the system.

Consider now a simulation comparable to the one presented above, but which uses the realistic initial conditions set (Equation 3.12). The pulse is generated by a 1 mm width 1 ps laser

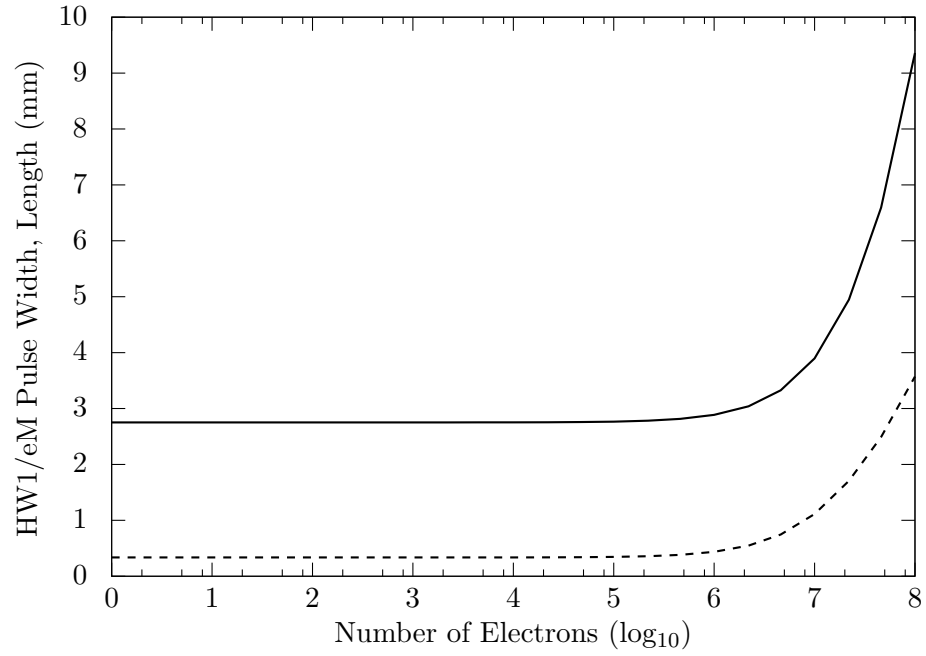


Figure 6: The final HW1/eM pulse width (solid) and length (dashed) after a 15 cm propagation. Pulses are initially similar except for the number of electrons in the pulse, each is generated by 1 mm (HW1/eM) width 1 ps laser pulses with 0.5eV excess photoemission energy and then traverses a 20mm acceleration region followed by drift region, accelerating to a velocity of $c/3$.

(HW1/eM) and accelerated by an electron gun which is 20mm in length and which accelerates the pulse through a voltage of 30 kV to speed $c/3$, the same velocity as in the idealistic case. The results of this simulation are presented in Figure 6. It is immediately obvious that the final transverse width is larger than in the ideal case presented in Figure 5, even in the low charge-density regime; this is primarily due to the additional divergence imparted by the negative lensing at the anode (see Section 3.4.4). One can see that though the pulse size does increase beyond a certain total pulse charge, and while that trend appears to start at a higher charge, due to the complexity of the pulse dynamics it is rather difficult to compare the exact charge-density from this plot to that in the idealistic case. What can be seen is that the transverse size increases more sharply with pulse charge at higher levels. Recall that the pulse is already diverging in the transverse direction, the increased pulse charge now serves to compound this action. This increased divergence then acts to lower the overall charge-density more quickly, thus the longitudinal pulse length is not affected as strongly as was seen in Figure 5.

4.3 Space-charge Effects and Spatial Focusing

In the transverse spatial dimension, space-charge effects that increase σ_T can be compensated for by using magnetic electron lenses (102; 56). In an UEM, of course, the electron pulse will also need to be focused onto the specimen — the focal spot size, post specimen image magnification, and CCD detector pixelation determining the spatial resolution in a TEM geometry (17). The extent to which space-charge effects limit the focal fidelity is expected to be dependent upon both N and the pulse shape (i.e., the pulse’s space-time eccentricity), while still subject to Liouville’s Theorem (see Section 3.2).

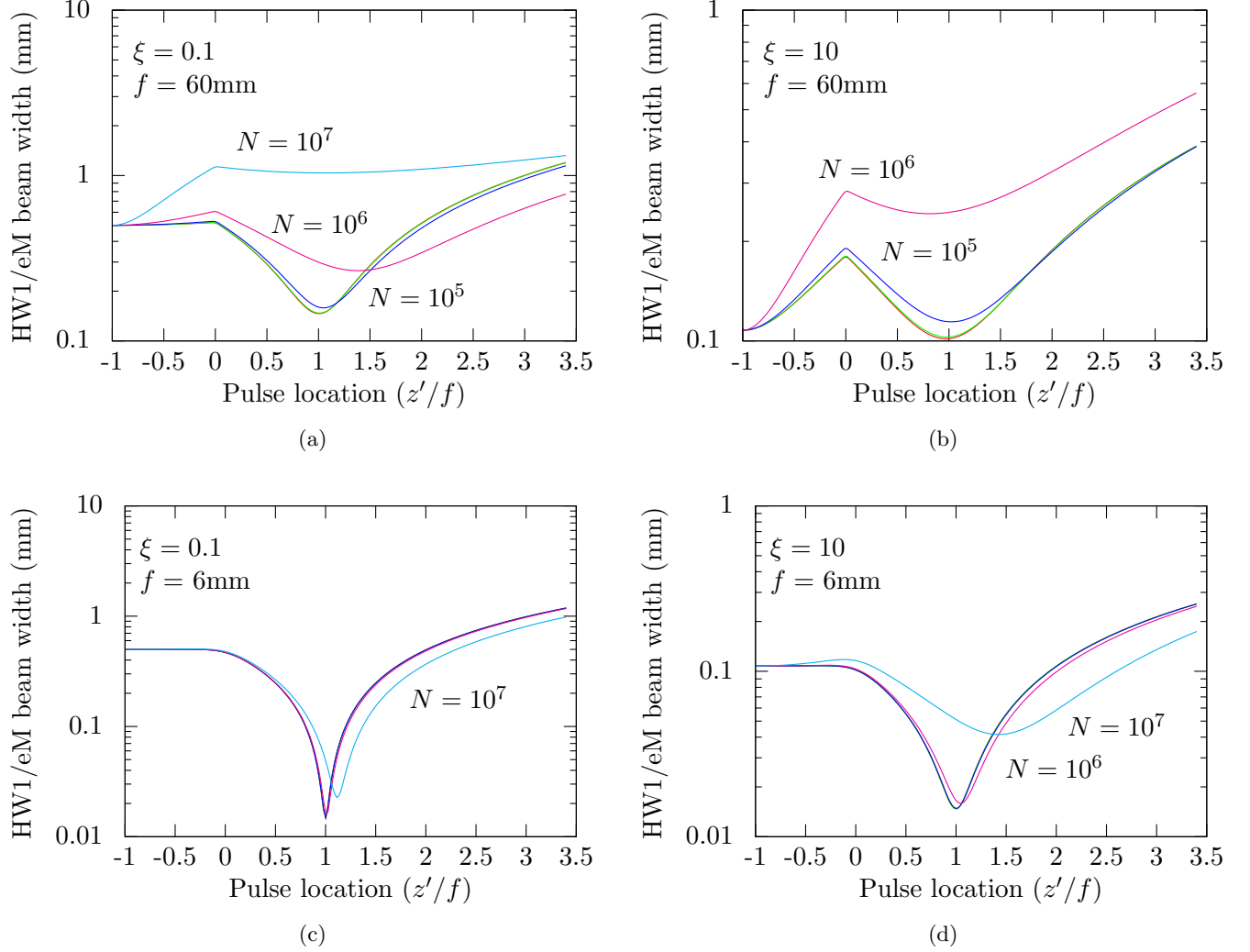


Figure 7: AG model simulated focal behavior of perfect magnetic lenses as a function of pulse charge N . Each plot's pulses begin at the lens' front focal plane at velocity $c/3$ (related to 30 kV energy) and have the same volume. The left plots ((a) and (c)) are initially oblate shaped, HW1/eM width $500\mu\text{m}$ and ellipticity $\xi(0) = 0.1$. The right plots ((b) and (d)) are initially prolate shaped, HW1/eM width $107.7\mu\text{m}$ and ellipticity $\xi(0) = 10$. Distance traveled in column is measured relative to the lens at $z' = 0$, in units of the focal length. The top plots ((a) and (b)) have a longer focal length $f = 60\text{mm}$ compared to the bottom plots ((c) and (d)) $f = 6.0\text{mm}$. A logarithmic scale is used for comparative clarity near the foci. Clearly the best performance is achieved for shorter focal lengths and oblate pulses (c) even at higher initial charge densities.

In the preceding sections it has already been established that oblate eccentricities are preferred for UEM in general. When focusing the pulse it can be shown that oblate pulses will also have markedly better performance. Figure 7 shows the predicted dynamics of the spatial electron pulse waist (HW1/eM) for initially oblate ($\xi(0) = 0.1$) or prolate ($\xi(0) = 10$) pulses under perfect focusing for lenses of two focal lengths; a ‘long’ focal length of 60mm and a ‘short’ focal length of 6.0mm. The pulse’s initial volume is constant in all cases ($w_T^2 w_z = (232\mu\text{m})^3$). For both lens strengths, the deleterious effects of space-charge are evident as the number of electrons/pulse N is increased. To make an effective comparison, highlighting the effect of space-charge alone, this simulation again uses the idealistic initial conditions set; the pulses used are at velocity associated with a 30kV energy and have momentum variance associated with $\Delta E = 0.5\text{eV}$, but are not simulated using an emitter and accelerator. As such the simulation presented approximates a beam which has been nearly perfectly collimated at the focus of a long focal-length lens.

The single-electron ($N = 1$) focal spot sizes of ~ 150 microns for the $f = 60\text{mm}$ lens and ~ 15 microns for the shorter $f = 6.0\text{mm}$ lens show marked increase starting around $N \approx 10^5$ and $N \approx 10^6$, respectively, and worsen dramatically above these thresholds. This order of magnitude difference is fundamentally related to the greater time of flight before the focus of the $f = 60\text{mm}$ lens; it increases the impulse that the internal Coulomb force can exert on the pulse as its charge density is increased under focusing. A consequent further effect is a shift in the focal position to $z' > f$. A more subtle effect is that oblate pulses are more readily

focused than prolate pulses — the rate of transverse pulse broadening due to space-charge effects already being intrinsically greater in the latter (Figure 4).

Thus, the extended AG electron pulse propagation model predicts that higher fidelity focusing will be achieved with shorter focal length magnetic lenses, higher acceleration energy electrons (time of flight reduction), and pulses with $\sigma_T \gg \sigma_z$ at the entrance aperture of the lens.

4.4 Compensation of Temporal Space-charge Effects: RF Cavities

In comparison to using magnetic lenses to compensate for transverse pulse broadening by using magnetic lenses, RF cavities are being employed in UED systems (102), and are expected to be employed in UEM systems as well, to compensate for longitudinal broadening in the ultrashort pulses. Figure 8 illustrates the operation of a $\Omega/2\pi = 3\text{GHz}$ TM_{010} RF cavity of axial length $d = \pi v_0/\Omega$ as an electron pulse compressor tuned to produce the shortest pulse at a distance $z' = 10\text{cm}$ behind the cavity for $N = 1$ and $N = 10^5$ pulse charges. The mathematical model of the RF cavity (see Section 3.4.3) employs $L_{RF} = d \approx 14\text{mm}$, $z'_{RF} = 0$, and a region of influence super-Gaussian of order 2 ($n = 2$ in Equation 3.29) to reflect the sharper ends of the RF cavity. In both cases, the idealized initial conditions are used, starting the pulse at $z' = -10\text{ cm}$, an excess photoemission energy $\Delta E = 0.5\text{ eV}$, velocity related to a $V_{DC} = 20\text{kV}$ acceleration potential, HW1/eM width $w = 0.1\text{mm}$ and duration $\tau = 100\text{fs}$ ($v_0\tau \approx 8.4\mu\text{m}$). This electron pulse is therefore initially in the preferred highly oblate regime ($\sigma_T(0) \gg \sigma_z(0)$), for which space-charge effects predominantly act in the longitudinal direction, broadening the pulse in time (see Figure 4).

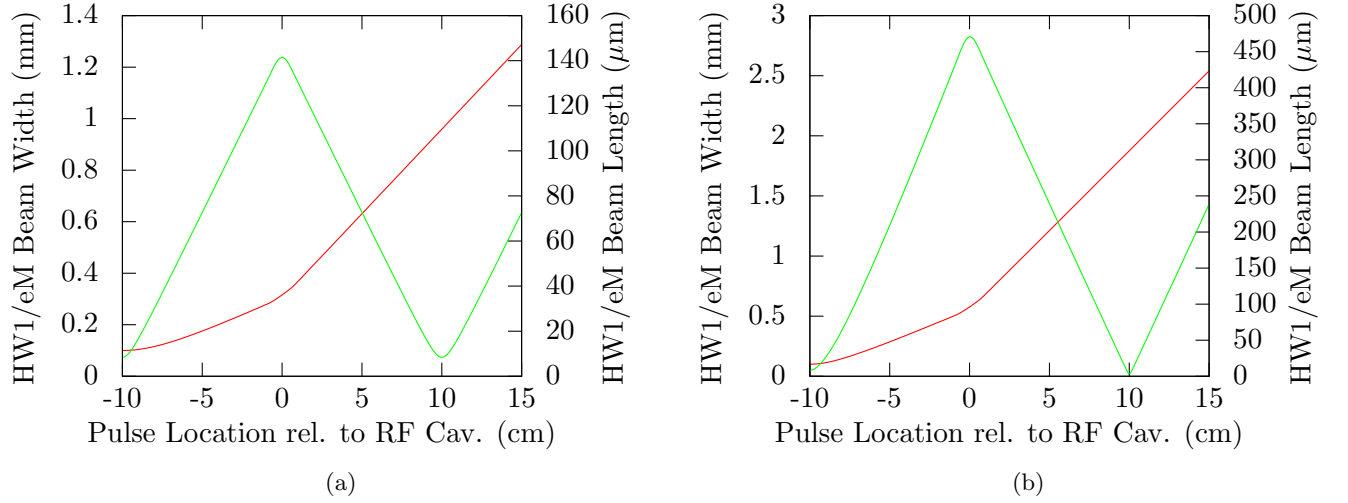


Figure 8: Dynamics of the pulse length (green) and width (red) under the influence of an RF cavity placed at $z' = 0$. The employed idealized pulses start at $z' = -100$ cm with velocity $v_0 \approx 84 \times 10^6$ m/s (20 kV) and initial HW1/eM width of $100 \mu\text{m}$ and length $\sim 8.4 \mu\text{m}$ ($v_0 \cdot 100$ fs). (a) has $N = 1$ electron and demonstrates one-to-one imaging of the initial pulse length at the focus at $z' = 100$ cm. (b) has $N = 1 \times 10^5$ electrons, whose added broadening allows for the factor of two reduction in pulse length at the focus (~ 48 fs).

Figure 8(a) depicts the optimized RF cavity performance with $N = 1$ electrons in the pulse. The internal pulse space-charge effects are negligible under these conditions, so that the RF cavity only compensates for the ‘dispersive’ electron pulse broadening to $\sim 1.67\text{ps}$ at the RF cavity entrance that is due to the initial longitudinal momentum spread caused by the $\Delta E = 0.5\text{eV}$ excess photoemission energy. For an RF field amplitude $E_0 = 450\text{ kV/m}$ and phase $\phi = 0$, the dispersion-generated momentum chirp γ_z is exactly reversed upon propagation through the RF cavity to produce a compressed pulse at $z' = 10\text{cm}$ behind the RF cavity. In this case, the pulse is returned to its original temporal duration — an exact 1-to-1 ‘temporal imaging’ of the photo-generated electron pulse at $z' = -10\text{cm}$ by the RF cavity to $z' = 10\text{cm}$. On the other hand, the dynamics of the spatial size of the electron pulse are clearly affected by the negative compound transverse lens of the RF cavity (the magnetic contribution of the TM_{010} -mode plus the axial entrance and exit aperture electric fields, see Section 3.4.3), increasing the pulse’s width at the temporal focus to a factor of $\sim 10\times$ its initial value.

In analogy to optical imaging, the compressed pulse duration in this dispersive limit is determined by the image-to-object distance (magnification) ratio, with pulses shorter than the original laser pulse duration being produced when the distance from the RF cavity to the temporal focus is less than that from the effective photocathode to the RF cavity; specifically, the ratio of the time-of-flight between the RF cavity and the temporal focus to that between the photo-gun and the RF cavity.

The RF electric field amplitude E_0 of about 450kV/m required to achieve the temporal focusing 10cm behind the RF cavity in the dispersive limit is also consistent with expectations.

By equating the differential impulse applied by the RF cavity across the electron pulse duration to that required to compensate for dispersive pulse broadening before the RF cavity and then compress the pulse thereafter, one can show that the required RF field amplitude for a TM₀₁₀ cavity with $d = \pi v_0/\Omega$ is given to a good approximation by

$$E_0 \approx V_{DC} \left(\frac{1}{L_1} + \frac{1}{L_2} \right), \quad (4.2)$$

where L_1 is the distance from the pulse source (the DC photoelectron gun) to the RF cavity (the object distance) and L_2 is the distance to the temporal pulse focus behind the RF cavity (the image distance). For the considered case, $V_{DC} = 20\text{kV}$ and $L_1 = L_2 = 10\text{cm}$, giving $E_0 \approx 400\text{kV/m}$, which is in reasonably good agreement with the optimum value of 450kV/m employed for the simulation displayed in Figure 8(a). Equation 4.2 also clearly indicates that the DC photoelectron gun and TM₀₁₀ RF pulse compression cavity should be considered as a single system, since the temporal ‘focal length’ of the RF cavity, V_{DC}/E_0 , is dependent upon the acceleration voltage.

The optimized RF cavity performance for the temporal compression of a pulse with the same initial photoemission conditions, but with $N = 10^5$ electrons, is shown in Figure 8(b). In this case, intra-pulse space-charge effects act to further broaden the initial 100fs pulse duration to $\sim 6\text{ps}$ after the $\sim 1\text{ns}$ time-of-flight over the 10cm distance to the RF cavity. The fact that almost the same RF field strength (495 kV/m) is required to generate a temporal focus at $z' = 10\text{cm}$ is a direct consequence of the linear dependence of the longitudinal RF cavity

force on z (Equation 3.36), which means that the required restorative force is not dependent on σ_z — just as the focal length of a perfect optical lens is independent of its aperture size. However, unlike in the dispersion limited case (Figure 8(a)), the compressed pulse duration is now a factor of ~ 2 less (~ 48 fs) than the original 100fs laser pulse duration. This additional pulse compression for the employed 1-to-1 image-to-object distance (magnification) ratio is made possible by the additional pulse bandwidth (and momentum chirp) generated by the space-charge effects — in analogy to self-phase modulation (and dispersion) in fiber-grating laser pulse compression (99). In this case, the ~ 20 -fold increase in the transverse pulse size (corresponding to a $\sim 400\times$ reduced peak pulse charge density) aids the temporal compression by greatly diminishing Coulomb effects that counteract the reduction in electron pulse duration. Again, in analogy to optical imaging, a stronger (and suitably phased) RF field will result in an even shorter compressed pulse duration as the distance to the temporal focus behind the RF cavity is reduced.

It is important to note that the example illustrated in Figure 8(b) approaches the limit imposed in obtaining Equation 3.35; namely that the longitudinal electron pulse length be much shorter than the axial length d of the RF cavity, or $\Omega z \ll v_0$. For a ~ 10 ps electron pulse entering the 3GHz RF cavity we have $\Omega z/v_0 = \Omega\tau \approx 0.19$, for which the small angle approximation $\sin(\Omega z/v_0) = \Omega z/v_0$ is 0.6% inaccurate. In principle, the AG model could simulate the action of the RF cavity on longer pulse by including additional terms $O(z^3)$ and higher in Equation 3.36 resulting from the expansion of $\sin(\Omega z/v_0)$, but at the expense of voiding its self-similar Gaussian approximation.

4.5 UEM Column Example

Through the use of multiple electron optical components such as magnetic lenses, RF cavities, and accelerators (properly region-of-influence limited by application of Equation 3.29), the extended AG model can be employed to design and assess a full UEM column from pulse generation to sample stage. The design of such a compound system is, of course, a cornerstone of modern electron microscope development, although space-charge effects are generally not included, since, on average, there is usually no more than one electron in the microscope column at a time. However, for a nanosecond DTEM (56; 86), the microscope column must be designed to compensate for transverse (r) space-charge effects, which dominate the propagation dynamics for the prolate electron pulses employed in such instruments (see Figure 4). For the ultrashort (i.e., picosecond and femtosecond) electron pulse durations used in UEMs (80) and UED experiments (102), the longitudinal (z) pulse dynamics due to both dispersion and space-charge effects must also be considered (as indicated in Figure 4).

Figure 9 shows an example of a compound element system for the delivery of an ultrashort electron pulse to the specimen area; in this case, optimized for $N = 10^6$ — the number of electrons per pulse required for single shot diffraction measurements (12). The displayed dynamics are for an electron pulse generated by a laser having HW1/eM duration $\tau = 100\text{fs}$ and width $w = 0.1\text{mm}$, driving a photocathode, with $\Delta E = 0.5\text{eV}$, then accelerated by 20 kV to a velocity of $8.4 \times 10^7\text{m/s}$. In this simple system, an optimum RF cavity ($\Omega = \pi v_0/d$) is surrounded by two magnetic lenses (positioned a realistic 5cm to either side of the RF cavity) that compensate for the electron beam divergence due to the non-zero $\eta_T(0)$ and the negative spatial lensing of

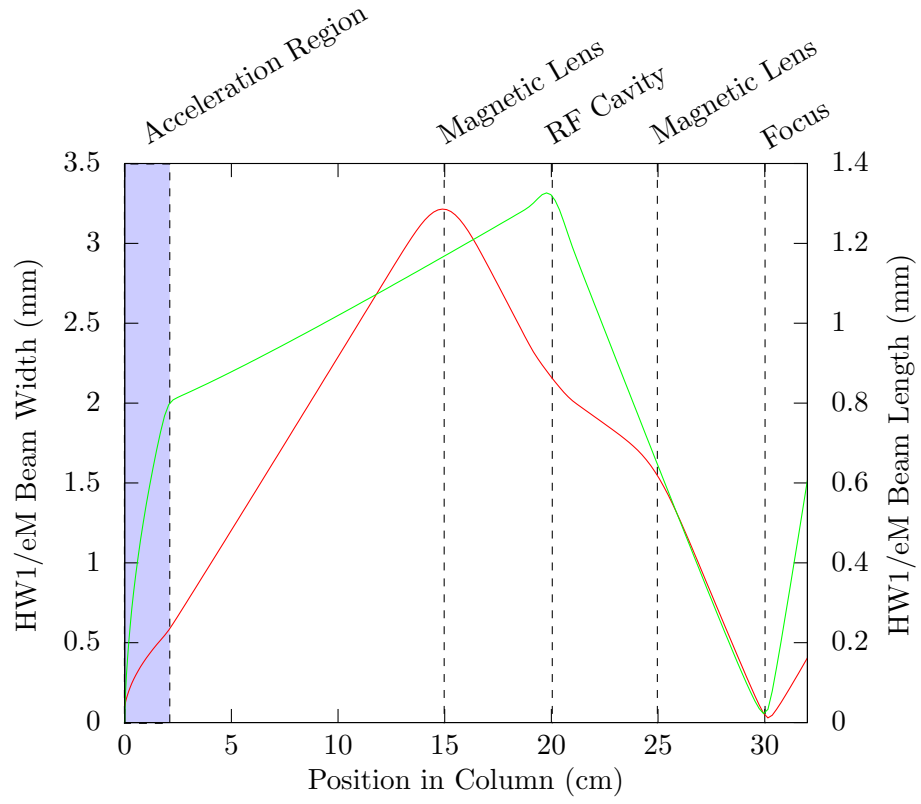


Figure 9: Example model of a compound system of electron-optical elements. The length (green) of the pulse is compressed to a “focus” 10 cm after the RF cavity at 20 cm. The width (red) is affected by two magnetic lenses (5 cm before and after the RF cavity) as well as by the cavity itself. The lenses are tuned to produce a simultaneous focus with the pulse length, creating a small spatial and temporal probe should this focal point represent a sample holder.

the RF pulse compression cavity. For the transverse dimension, this arrangement of electron optical elements is similar to the Cooke triplet in optics. The magnetic lenses are assumed to be identical and wired in series, and thus have equal magnetic field strengths. The three lensing elements are positioned at a distance of 15cm from the cathode to the front of the first magnetic lens and are adjusted so as to space-time image the electron pulse 5cm behind the second magnetic lens. The dependencies of the the spatial variances, σ_α , shown in Figure 9 as the electron pulse propagates through the multi-element system, clearly illustrate the effect of the magnetic lenses and RF cavity in the transverse (r) and longitudinal (z) dimensions. As the image-to-object distance ratio is less than unity in this case, both the transverse and longitudinal imaged pulse dimensions are reduced relative to their initial values.

As seen in Section 4.2, with increasing pulse charge, Ne , space-charge effects in general will act to degrade the space-time imaging by increasing the three-dimensional pulse size delivered to the reference plane positioned 5cm behind the second magnetic lens. At $N = 10^6$, space-charge effects moderate the image demagnification due to the ~ 2 object-to-image distance ratio in Figure 9. In other words, for the displayed compound element system, which could be employed in UED experiments (102), the initial space-time resolution associated with the $\sim 0.1\text{mm}$ spot size and $\sim 100\text{fs}$ pulse duration can be maintained (or bettered) for $N \lesssim 10^6$. For a UEM, on the other hand, it may be necessary to separate longitudinally the space and time images produced by the compound element column. This is because the inclusion of the microscope's objective lens will likely require the pulse's time focus to be at the objective's back focal plane (i.e., in the specimen) while the column's spatial image may need to be located

at the objective's front focal plane (i.e., entrance aperture) for efficient beam transfer with minimal spherical aberration. Fortunately, a compound component system of the type shown in Figure 9 with a RF cavity can meet this challenge since the longitudinal positions of the two foci can be manipulated independently.

CHAPTER 5

UEM DESIGN CONSIDERATIONS

In Chapters 2 through 4, I have explored the mathematical side of designing an ultrafast electron microscope; modeling the behavior of a pulse and the effects that column elements have upon it. However, since microscopy is an experimental science, we are also designing and building a prototype UEM system at UIC. In doing so we have decided that special care must be given to the creation and propagation of the electron beam. In the case of single-shot UEM, in which the image of the sample is acquired using only one electron pulse, several factors lead to two major considerations: first, that a large area photoemission source is required versus smaller area or even single point emitters, and second, that the “normalized transverse emittance,” a beam quality figure of merit which will be defined later, must be minimized.

These considerations drive the remainder of this thesis. In this chapter, I will first convince the reader of these considerations. As a direct consequence thereof, it is our belief that a successful UEM project cannot simply stem from small modifications to the platform of a conventional electron microscope. In the following chapters, I will show how we are addressing these considerations for the prototype system at UIC, both in column design (Chapter 6) and photocathode engineering (Chapter 7).

5.1 Pulse Charge Requirement

It is straightforward to show that in order to make a useful image in an electron microscope, the number of electrons collected must be above some minimum number. The Rose criterion (88) indicates that an average detector signal strength of ~ 100 electrons/pixel is required for adequate gray scaling of the image. For a $1\text{k} \times 1\text{k}$ CCD camera, this implies an incident electron pulse with $N = 10^8$ (13).

In a conventional electron microscope the electrons are generated by one of several processes, often by heating the cathode or applying a large field to the cathode, or combinations thereof. Although these processes produce a very large number of electrons, far more than required by the Rose criterion, they are not highly directional. A pinhole is used to eliminate most of the electrons, with the exception of those which will travel down the column axis, thereby reducing the beam current but producing a high-quality beam. For conventional electron microscopes without time resolution, the Rose criterion may be met for arbitrarily low beam current by simply allowing the image to acquire for a long enough time to collect sufficient electrons. Further, high beam current may be damaging to the sample over time, so a lower beam current is often preferred.

By definition, for single-shot imaging with a DTEM, all of the electrons used to form an image must be contained in a single pulse. In a single-shot DTEM, the dynamics being studied are often destructive, regardless of the knock-on damage cause by the probe pulse; what matters is that the system be able to probe the sample before it is destroyed. Nevertheless, although sample damage concerns may be neglected, the use of a pinhole is likely to reduce the pulse

charge below the useful level. This means that the designer of a DTEM must endeavor to retain and utilize all of the generated electrons.

It should be noted that for diffraction studies performed in a DTEM, many fewer electrons per pulse are required for single-shot experiments; typically, about 10^6 electrons/pulse (12) as significantly less signal is required to determine the position of discrete single-crystal Bragg diffraction spots or diffraction rings for polycrystalline specimens.

5.2 Generation Current Limitations

Since we are now aware that there is a large minimum number of electrons needed per pulse, it is only natural to ask if there is the practical limit on how much charge (i.e., the number of electrons/pulse, N) can be extracted from a pulsed laser-driven DC photoelectron gun. When the incident laser pulse duration τ is longer than the time-of-flight (TOF) t_{gun} of a single electron across the acceleration gap d of the DC gun with a potential V_{DC} , $\tau > t_{gun} = d\sqrt{2m/eV_{DC}} \approx 0.1 - 1\text{ns}$, typically, then the maximum photocurrent density J_{CL} is given by the well-known Child-Langmuir law (29; 57):

$$J_{CL} = \frac{4\varepsilon_0}{9} \sqrt{\frac{2e}{m}} \frac{V_{DC}^{3/2}}{d^2}, \quad (5.1)$$

where e is the electron charge and ε_0 is the vacuum permittivity.

This steady-state law for the maximum current density that can be achieved is not valid in the regime of interest for UEM (and UED) where the use of picosecond and femtosecond photocathode drive laser pulses implies that t_{gun} is usually much greater than the electron

pulse duration τ_e . Though there is no clear delineation in the literature or the community between moniker of Ultrafast Electron Microscopy (UEM) and the more general term Dynamic Transmission Electron Microscopy (DTEM), we propose that this is useful delimitation, reserving the term UEM for those systems where the pulse can be completely contained inside the accelerator, i.e. $t_{gun} > \tau_e$. Pulses of this type are subject to a different “short pulse analog” of the Child-Langmuir limit.

In this short pulse case, an equivalent diode approximation (101) allows for the definition of a critical current density associated with virtual cathode formation in terms of the steady-state Child-Langmuir limit:

$$J_{crit} = \frac{27}{4} \left(\frac{1 - \sqrt{1 - \frac{1}{3}\chi^2}}{\chi^3} \right) J_{CL}, \quad (5.2)$$

where $\chi = \tau_e/t_{gun}$. When $\chi \ll 1$, the usual case in UEM, the critical current density is simply given by

$$J_{crit} = \frac{\varepsilon_0 E_{DC}}{\tau_e}, \quad (5.3)$$

where the DC gun field $E_{DC} = V_{DC}/d$. This relation may be rewritten to yield a critical number of photoemitted electrons/pulse before virtual cathode formation:

$$N_{crit} = \frac{\pi \varepsilon_0 w^2 V_{DC}}{ed}. \quad (5.4)$$

In obtaining the above equation, we have used an irradiated photocathode area of πw^2 associated with an incident Gaussian laser pulse of the form of Equation 3.1. The relation clearly

indicates that N_{crit} is only dependent upon the initial DC surface field (i.e., E_{DC}) at the photocathode and the illuminated area — as expected, because a virtual cathode forms when the initial photocathode surface charge density associated with E_{DC} is photoemitted, effectively screening the cathode from the acceleration field.

For a typical DC gun with $E_{DC} \approx 30$ kV/cm (e.g., $V_{DC} = 100$ kV and $d \approx 3$ cm), Equation 5.4 reveals that the generation of 10^8 electrons/pulse needed for single-shot imaging applications in a DTEM with a $1k \times 1k$ CCD detector requires an incident laser beam area πw^2 of about 1 mm^2 — the virtual cathode being formed for the extraction of more than 1.7×10^8 electrons/ mm^2 in this short pulse regime. We note that Equation 5.4 does not express a limit on the number of electrons/pulse N that can be emitted from a pulsed laser-driven DC photoelectron gun, it merely indicates a critical number before virtual cathode formation occurs. More electrons can be produced, at the expense of a severely distorted temporal electron pulse profile (101).

This finally leads to the first consideration for UEM design mentioned in the introduction: for the clean pulsed emission of sufficient to create a useful image, the generated beam should have a HW1/eM width

$$w \gtrsim \sqrt{\frac{Ned}{\pi\epsilon_0 V_{DC}}} . \quad (5.5)$$

For our example case above, to cleanly extract $N \geq 10^8$ electrons/pulse we require $w \gtrsim 0.56$ mm. The effect that accommodating a large transverse pulse size has on designing an Ultrafast Electron Microscope will be discussed in Chapter 6.

5.3 Beam Quality and Resolution Limit

A common figure of merit for electron beams is its normalized transverse emittance (45), ε_T , defined as

$$\varepsilon_T = \frac{1}{mc} \sqrt{\langle x^2 \rangle \langle p_T^2 \rangle - \langle xp_T \rangle^2}, \quad (5.6)$$

where m is the electron mass, c is the speed of light in vacuum and x and p_T are the transverse position and momentum respectively. For the usual case of axially symmetric electron pulses, we may use the simplified form

$$\varepsilon_T = \frac{1}{mc} \sqrt{\langle x^2 \rangle \langle p_T^2 \rangle}. \quad (5.7)$$

By Liouville's Theorem (Section 3.2), we know that this quantity is conserved throughout pulse propagation (for free-space and perfect electron-optical elements), and therefore is related directly to the initial photoemission properties of the system. For a laser pulse of the form of Equation 3.1 we have simply

$$\varepsilon_T = \frac{w}{mc} \sqrt{\frac{\langle p_T^2 \rangle}{2}}. \quad (5.8)$$

Note that imperfect electron-optical elements may cause “emittance growth” (78), increasing the pulse's emittance after these elements.

This normalized transverse emittance limits the resolving capability of the beam, so this quantity can be thought of as a measure of the beam quality, where a lower number is preferred (17). Since Equation 5.5 specifies a lower bound on the emission spot size w , knowing a UEM will exhibit higher resolution by employing an electron source with the minimum possi-

ble transverse emittance directly implies that every effort must be made to reduce the initial transverse momentum spread. Though deriving an absolute limit on the allowable transverse emittance for imaging in a UEM would depend on many column-specific factors, since diffraction is expected to impose less stringent requirements on the beam than imaging, we may consider it when searching for an upper bound on transverse emittance.

In Ref. (17), we explore the impact of these limitations for an ultrafast electron diffraction (UED) experiment. We find that for a desired spatial resolution per pixel ΔX (related to the magnification) using a $N_p \times N_p$ detector, one may only resolve a fractional change $\Delta a/a$ in a crystalline material's Bragg plane spacing a in the M^{th} diffraction order if

$$\varepsilon_T \leq \frac{5\hbar}{mc} N_p \Delta X \frac{M}{a} \left(\frac{\Delta a}{a} \right). \quad (5.9)$$

However, because of lower limit that exists on w from Equation 5.5, we can say that these requirements impose an upper limit on the initial transverse momentum spread

$$\sqrt{\langle p_T^2 \rangle} = \sqrt{\eta_T(0)} \leq \frac{5\sqrt{2}\hbar}{w} N_p \Delta X \frac{M}{a} \left(\frac{\Delta a}{a} \right). \quad (5.10)$$

To have $\Delta X = 1$ nm spatial resolution, and be able to measure a 10% change ($\Delta a/a = 0.1$) in a Bragg spacing $a \sim 1\text{-}2$ Å in the 1st diffraction order, the example DTEM from Section 5.2, equipped with a 1k x 1k CCD will require $\varepsilon_T \lesssim 2$ nm. For comparison, using the simplistic initial conditions in Equation 3.12, exciting carriers from a HW1/eM $w = 0.56$ mm Gaussian spot-size on a Tantalum metal photocathode (work function $\Phi = 4.25$ eV) using our laser

(photon energy $\hbar\omega = 4.75$ eV, further described in Section 6.1), for an excess photoemission energy $\Delta E = \hbar\omega - \Phi = 0.5$ eV, the normalized transverse emittance is about 200 nm.

One might think to narrow this discrepancy by simply better matching the photocathode work function and the laser photon energy, thereby reducing the excess photoemission energy ΔE . Unfortunately, since the photoemission efficiency is proportional to ΔE^2 (94), though this would indeed reduce the transverse emittance, it would do so at the cost of a much reduced pulse charge. In Chapter 7, I will explore several more exotic photoemission processes in an attempt to reduce ε_T without this penalty.

CHAPTER 6

PROTOTYPE INSTRUMENT

It is common in the DTEM field to modify an existing transmission electron microscope column, adapting it for laser-stimulated electron generation. For the reasons covered in Section 5.2, the prototype UEM at UIC is being built to accommodate electron pulses with a large transverse size. To satisfy this restriction, it has been designed and built from parts either fabricated in-house or from commercially available sources, both for the ease of prototyping inherent in using replaceable parts and to accommodate the physical limitations that our choice of a large beam width have imposed on the standard electron microscope column components.

In this chapter, I will first describe the laser system which was custom built for the prototype UEM system being constructed at UIC. I will then describe how we have addressed the necessity of the large-area electron beam in each of the individual components of the UEM column.

6.1 Yb:KGW Laser System

In order to experiment using very short laser pulses, we have designed and built a custom Ytterbium-doped potassium gadolinium tungstate ($\text{Yb:KGd(WO}_4)_2$ or Yb:KGW) laser system (16). In practice, the flexibility afforded by having a custom-built system has outweighed its original performance benefit. I have shown in Section 3.1 that the electron pulse duration is not a simple function of the laser pulse duration, yet, at the time the laser was built, this fact

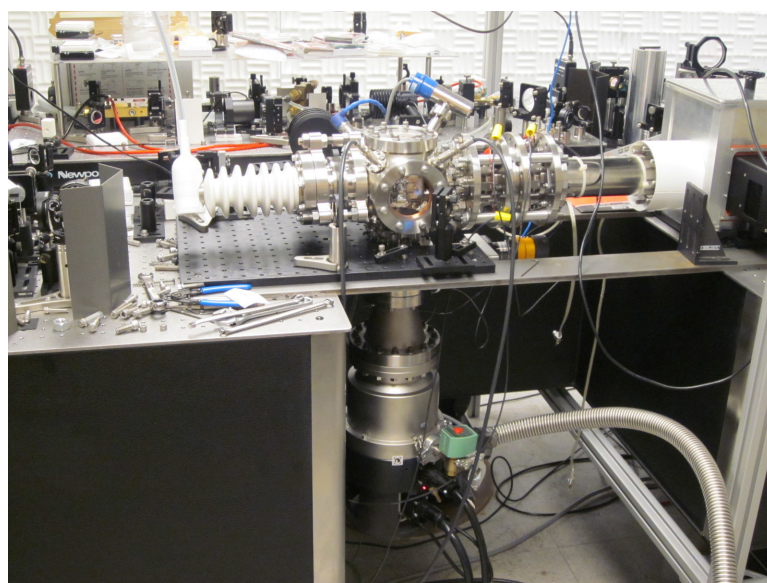


Figure 10: Picture of the majority of the prototype UEM column at UIC. The main vacuum chamber is laid sideways, with the high voltage (gun) at the left and the imaging system on the right. The magnetic levitated turbo pump hangs below the column, a scroll pump used for backing is not pictured. The laser system is in the background. All of the above is mounted on a custom shaped active vibration-canceling optical table. The electronic control systems are not pictured.

was not yet obvious. As such, our laser was designed to produce relatively high power output while generating ultrashort pulses, on the order of 250 fs for some conditions.

6.1.1 Laser Introduction

Yb:KGW is becoming a widely used solid-state gain medium for ultrafast laser systems. As with other Yb-doped laser crystals (21), this is primarily due to the gain medium's advantageous absorption properties for direct laser diode pumping at 980nm, its broad emission bandwidth around 1040nm, and consequent small ($\sim 6\%$) quantum defect that results in a relatively low thermal load. Mode-locked (ML), diode-pumped, Yb:KGW laser oscillators generating pulses with sub-picosecond durations at average output powers in excess of 1W have been demonstrated (22; 31; 66; 43) and are now available commercially (1; 9). Such lasers have used dichroic mirrors (22; 66; 81; 65), polarization-coupling (43), or more complex optical geometries (e.g., thin disk lasers (1; 23)) to pump the laser crystal in an efficient manner.

The spectroscopic properties of the biaxial Yb:KGW laser crystal (19) indicate that the optimum diode pumping arrangement is for 980nm radiation polarized parallel to the optical N_m -axis since the crystal has the largest absorption cross-section in this configuration and, hence, the smallest absorption saturation intensity to drive the gain medium into a quasi 4-level system or to achieve transparency at the emission wavelength (21). However, as is the case for Yb-doped potassium yttrium tungstate (Yb:KYW) (60; 49), mode-locked Yb:KGW lasers should ideally oscillate with radiation polarized parallel to the optical N_p -axis to access the broadest gain bandwidth around 1040nm, where the emission cross-section is comparable to that of the absorption along the optical N_m -axis (43; 19). This optimal requirement for orthogonal

linear pump and laser polarizations led Holtom (43) to employ a polarization-coupling scheme to diode pump longitudinally a 10W, sub-500fs, Yb:KGW laser.

In this chapter, a high-power, femtosecond Yb:KGW oscillator is presented that also accesses the broader emission bandwidth parallel to the optical N_p -axis (parallel to the crystallographic b -axis), yet employs a simpler geometry for polarized diode-pumping on the strongest 980nm absorption line parallel to the optical N_m -axis (rotated by $\sim 20^\circ$ from the crystallographic a -axis (19; 73; 84)). The laser head design is based on the thermal lens shaping (TLS) technique developed in-house for astigmatism compensation in diode-pumped Nd-doped lasers with Brewster-cut gain media (87). It employs a simple single layer SiO_2 anti-reflection coating on the gain medium to provide minimal loss for p -polarized intracavity 1040nm laser radiation and less than 0.5% surface reflection for orthogonal s -polarized 980nm pump light. The result is a simple and robust, soliton mode-locked and directly diode-pumped, solid-state laser oscillator delivering over 4W of average output power in a 63MHz train of pulses with a duration less than 300fs. Frequency doubling of this laser output in a 2mm Brewster-cut Lithium triborate (LBO) crystal provides 1.65W of average power at 520nm.

The Watt-level green output power from the frequency-doubled sub-picosecond Yb:KGW oscillator corresponds to a visible peak laser pulse power in excess of 100kW, which is well-suited for further frequency conversion through harmonic generation or pumping of an ultrashort pulse optical parametric oscillator. To our knowledge, the generation of sub-picosecond green peak pulse powers greater than 100kW by frequency doubling the output of a laser oscillator has only been demonstrated for high-power thin-disk (24; 68) and cavity-dumped (79) Yb-doped solid-

state lasers, although externally-doubled commercial Ytterbium femtosecond oscillators (1; 9; 4; 10) and oscillators with rod-like Yb-fiber gain media (77) can be expected to yield comparable peak green pulse powers.

6.1.2 Laser Head Design

The design of the laser head follows the example of Holtom (43), which ensures efficient pumping and access to the broadest emission bandwidth of Yb:KGW, while also employing the thermal lens shaping (TLS) technique to compensate for astigmatism (87). To ensure efficient operation of a Yb:KGW laser, the dominant absorption feature at 980nm for radiation polarized parallel to the optical N_m -axis ($\sim 20^\circ$ from the crystallographic a -axis) should be pumped using high brightness diode lasers. On the other hand, as with Yb:KY(WO₄)₂ (60; 49), the broadest emission bandwidth for ultrashort pulse generation occurs for radiation polarized parallel to the optical N_p -axis (parallel to the crystallographic b -axis (43)) in this biaxial material. Instead of using a polarization-coupled pumping geometry (43) to ensure these optimum pump-lasing conditions, we employ the non-Brewster crystal geometry and cut shown in Figure 11(a), where a single 193nm-thick SiO₂ anti-reflection coating is applied to both polished 3x10mm Yb:KGW crystal faces. At an angle of incidence of 32.3° , this coating theoretically has zero reflection loss for p -polarized 1040nm laser radiation parallel to the b -axis propagating perpendicular to the a - b plane of the crystal (Figure 11(b)); i.e., the preferred optical N_p -axis with refractive index $n_p = 1.98$ (19; 84). The SiO₂ coating also has an appropriate bandwidth for femtosecond laser operation in excess of 100nm (to the 0.1% reflection points) for p -polarized radiation centered at 1040nm. On the other hand, the $\sim 0.4\%$ reflection loss per surface for s -polarized 1040nm

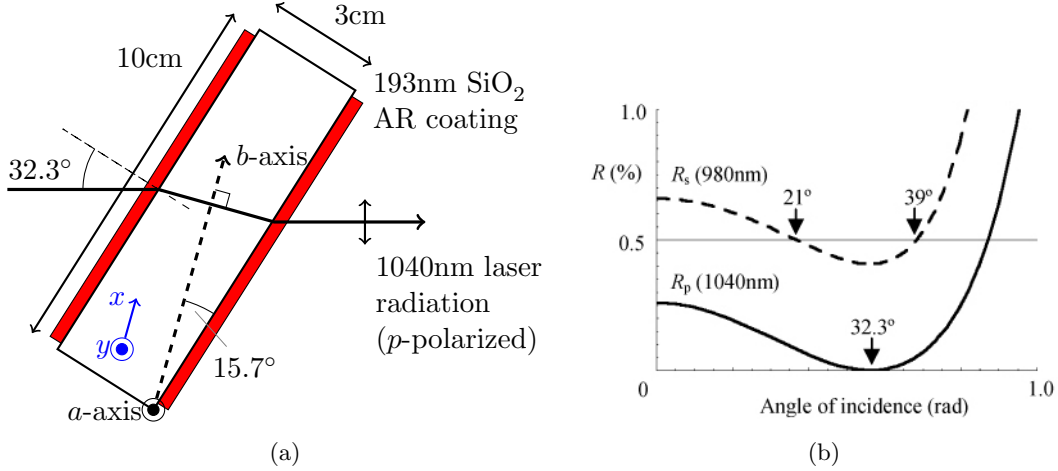


Figure 11: (a) Top view of the 3x3x10mm AR coated Yb:KGW laser crystal showing the crystal cut, the direction of propagation of p-polarized laser radiation at 1040nm, and the x (tangential) and y (sagittal) directions (in blue) employed in the thermal analysis. Pump laser radiation (at $\sim 20^\circ$ to the crystal face) is not pictured. (b) Calculated reflectivity of the 193nm SiO₂ AR coating as a function of incidence angle for p-polarized 1040nm laser radiation (solid line) and s-polarized 980nm pump radiation (dashed line).

radiation is sufficient to suppress s-polarized oscillation in a laser resonator. In addition, the same anti-reflection coating has less than 0.5% reflection loss for s-polarized 980nm pump radiation (polarized parallel to the a -axis of the Yb:KGW crystal) at incidence angles between 21 and 39° (Figure 11(b)). Thus, in this Yb:KGW laser crystal geometry, the largest absorption cross-section associated with the optical N_m -axis is accessed with about 94% efficiency ($\cos 20^\circ = 0.94$) by the s-polarized pump radiation.

Efficient pumping is achieved with two, 35W, dual-axis collimated and TM-polarized laser diode arrays operating at 980nm (HLU35C10x5-980 from LIMO GmbH (6)). The ~ 3 nm emission linewidth of the two laser diode arrays is well matched to the 3.7nm full-width half-

maximum (FWHM) 980nm absorption line of Yb:KGW (81; 19; 3). Moreover, the two dual-axis collimated laser diodes have full-angle $1/e^2$ intensity beam divergences of $\theta_y \approx 4.4\text{mrad}$ and $\theta_x \approx 6.8\text{mrad}$ in the horizontal (x -direction parallel to the emitter array) and vertical (y) directions respectively. With 100mm focal length lenses, this allows the pump radiation to be focused to a pump spot diameter $2W \approx 400\mu\text{m}$, yielding a maximum incident pump irradiance of $\sim 28\text{kW}/\text{cm}^2$ from one laser diode array. The Yb concentration was chosen to be 2% atomic doping to ensure that more than 90% of the pump radiation was absorbed over the 3mm Yb:KGW crystal thickness. With the employed counter-propagating pump geometry, the resultant maximum average pump irradiance over the crystal length is then roughly 3 times the $\sim 6\text{kW}/\text{cm}^2$ saturation intensity of the dominant 980nm absorption line (24). The laser crystal was obtained from NovaPhase (8).

To ensure a stigmatic laser resonator, we also employ the thermal lens shaping (TLS) technique (87) to compensate for the astigmatism induced by the non-normal incidence geometry of the laser crystal. For the employed non-Brewster crystal cut (Figure 11(a)), a ray transfer matrix analysis (with the x direction parallel to the crystallographic b -axis and the y direction parallel to the a -axis) reveals that the required ellipticity for a stigmatic thermal lens generated by a parabolic temperature distribution, $T(x, y) = T_0 - \frac{1}{2}(A_T x^2 + B_T y^2)$, where T_0 is the on-axis temperature, is given by

$$\frac{B_T}{A_T} = \frac{\cos^2 \theta_2 \left(\frac{dn}{dT} \right) + 2\alpha_T \Delta (n \cos \theta_2 - \cos \theta_1)}{\cos^2 \theta_1 \left[\left(\frac{dn}{dT} \right) + 2\alpha_T \Delta (n \cos \theta_2 - \cos \theta_1) \right]}. \quad (6.1)$$

Here, $\frac{dn}{dT}$ and n are the thermo-optic coefficient and refractive index of the medium respectively (in this case for radiation polarized along the optical N_p -axis), θ_1 is the 32.3° angle of incidence, $\theta_2 = 15.7^\circ$ is the angle of refraction (as $n_p = 1.98$ (19; 84)), and Δ is the fraction of the crystal length l contributing to the bowing of the crystal faces under thermal expansion with coefficient αT (87). Generally, $\Delta \approx W/l$, where W is the transverse size (radius) of the pumped region (52). In our case, $l \approx 3\text{mm}$ and $W \approx 0.2\text{mm}$, so that $\Delta < 0.1$, implying that the thermal duct due to a non-zero $\frac{dn}{dT}$ primarily determines the required B_T/A_T ratio. In other words, for the potassium gadolinium tungstate ($\text{KGd}(\text{WO}_4)_2$) crystal geometry of Figure 11(a), we expect from Equation 6.1 to require $\frac{B_T}{A_T} \approx \frac{\cos^2 \theta_2}{\cos^2 \theta_1} = 1.3$.

The spatial pump distribution needed to generate the required B_T/A_T ratio can be found using a cosine Fourier series solution to the thermal diffusion equation for our two-dimensional problem,

$$\kappa \nabla^2 T(x, y) = Q(x, y), \quad (6.2)$$

where κ is the thermal diffusion coefficient. Thermal diffusion in the third z -direction has been neglected due to the relatively uniform longitudinal heat deposition resulting from our counter-propagating pump geometry (87). The specifications of our dual-axis collimated diodes (6) indicate that heat source can be represented mathematically as

$$Q(x, y) = Q_0 \exp \left[-\frac{x^2}{W_x^2} - \left(\frac{y^2}{W_y^2} \right)^3 \right]; \quad (6.3)$$

that is, the focused pump radiation is described accurately by a Gaussian irradiance distribution in the horizontal (x) direction with half-width 1/e maximum (HW1/eM) spot size W_x and a super-Gaussian of order 3 in the vertical (y) direction with spot size W_y . Equation 6.2 can then be solved using the appropriate boundary conditions for our 3x10mm crystal cross-section for the employed TLS technique (87); namely, heat removal only through the top crystal face implies $T(x, y = \pm 1.5\text{mm}) = 0$ (or arbitrary constant) and $\frac{\partial T}{\partial x} = 0$ at $x = \pm 5.0\text{mm}$ for any y . For a fixed vertical pump spot size of $W_y = 0.2\text{mm}$, our analysis indicates that in order to achieve the required ratio $B_T/A_T = 1.3$ in the parabolic approximation for $T(x, y)$ about $(x, y) = (0, 0)$ a horizontal pump spot size $W_x = 0.3\text{mm}$ is needed; in other words, the required $Q(x, y)$ heat source spot size ratio (or ellipticity) $W_x/W_y = 1.5$. This analytical result for the central region around the laser beam axis is shown in Figure 12; displayed are the horizontal ($y = 0$, Figure 12(a)) and vertical ($x = 0$, Figure 12(b)) sections, respectively, through the $Q(x, y)$ and $T(x, y)$ distributions. Also shown are the parabolic approximations to the pump-induced temperature distribution (dashed lines) and representative TEM₀₀ Gaussian laser modes (shaded area) in the Yb:KGW crystal with a HW1/eM field mode sizes of $w_y = 160\mu\text{m}$ and $w_x = 182\mu\text{m}$ (14% larger due to refraction (Figure 11(a))). This mode size ensures efficient pump-probe overlap for the TEM₀₀-mode while minimizing the loss due to ground state absorption in the unpumped regions of the Yb-doped gain medium (21); in particular, in the vertical direction (Figure 12(b)) where w_y greater than about $0.8W_y$ leads to significant absorptive loss as the extrema of the laser mode extend beyond the sharply-bounded super-Gaussian pump region.

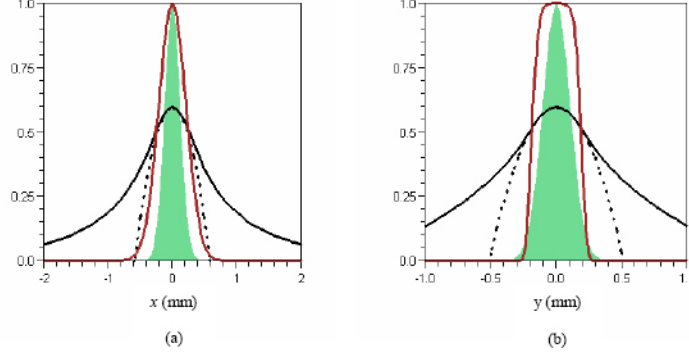


Figure 12: Analytical evaluation of the temperature distribution $T(x, y)$ due to the Gaussian/super-Gaussian heat source $Q(x, y)$ in the (a) horizontal ($y = 0$) and (b) vertical ($x = 0$) directions: $Q(x, y)$ - red-brown line; $T(x, y)$ - black line; parabolic approximation to $T(x, y)$ - dashed black line; representative TEM_{00} laser field modes - solid green.

The analysis clearly shows that the TEM_{00} laser mode will experience a near perfect pump-induced thermal lens upon propagation through the gain medium — the deviation of $T(x, y)$ from the parabolic approximation, and hence a perfect dominant thermo-optic (GRIN) duct, being insignificant over the size of the laser mode in both the horizontal and vertical directions. Moreover, the fact that $W_x \approx 1.6w_x$ implies that some degree of horizontal spatial walk-off between the pump and laser beams can be tolerated in this TLS geometry. For example, when the pump and laser beams are exactly overlapped at the center of the Yb:KGW crystal, an external angle of 0.1rad ($= 5.7^\circ$) would generate an effective spatial walk-off of only about $75\mu\text{m}$ over our 3mm gain crystal length. Clearly, this can be readily accommodated by the $W_x = 0.3\text{mm}$ horizontal pump spot size when $w_x \approx 180\mu\text{m}$. However, even though $W_x > w_x$, the Gaussian (rather than super-Gaussian) horizontal pump mode profile is still expected to

assist in ensuring TEM₀₀-mode operation since the net horizontal gain profile (gain minus absorptive loss) will fall off more rapidly than the pump profile for a quasi-three level Yb-doped gain medium (21).

We note that the above thermal lens analysis neglects the anisotropy of the thermal conductivity κ in potassium gadolinium tungstate (KGd(WO₄)₂) (19; 73) and stress-induced refractive index changes (109). For the employed crystal cut in our TLS geometry (Figure 11(a)), the anisotropy in κ (73; 3) is not expected to have a significant effect; the laser head geometry dictates that the dominant pump-induced heat conduction will be in the saggital (y) direction along the crystal a -axis where $\kappa \approx 2.6\text{W}/(\text{mK})$ (heat extraction only through the top and bottom 3x10mm crystal faces), so that the 46% larger value of κ along the b -axis (x) direction at 3.8W/(mK) should not have a large influence on the heat conduction. We see no observable effect from changes due to stress in the pumped gain medium, due both to the much stronger effect of the natural birefringence of the crystal and the laser polarization being along the optical N_p -axis (43).

6.1.3 The Yb:KGW laser cavity

The diode-pumped TLS Yb:KGW laser head is placed in the 2.35m-long, asymmetric z-fold cavity shown in Figure 13(a). The two focusing gain section mirrors each have a group velocity dispersion (GVD) of $-1300(\pm 150)\text{fs}^2$ (Layertec GmbH (5)), a radius of curvature $R = 50\text{cm}$, and are positioned 29.5cm from the gain medium. The 5° angle of incidence on the gain section mirrors results in minimal astigmatism, although any net round-trip cavity astigmatism can be compensated for by the TLS technique. The longer 75cm arm of the resonator is terminated

by a concave ($R = 1\text{m}$ and angle of incidence $< 2^\circ$) high reflector focusing the intracavity radiation on a saturable Bragg reflector (SBR) with a 1% reflectivity modulation depth at 1040nm (BATOP GmbH (2)) positioned a distance z from the focusing mirror. The shorter 63cm arm is terminated by a plane output coupler with a 7% transmission at 1040nm. As a free-running oscillator (SBR focusing section replaced by flat high reflector at $d_2 = 75\text{cm}$), the laser produced over 6W of TEM₀₀ ($M^2 < 1.2$) output power.

The stability analysis of our diode-pumped Yb:KGW laser (Figure 13(b)), clearly indicates that the resonator configuration is unstable for thermal focal lengths less than about -6m^{-1} (diopters) and is unlikely to oscillate for negative thermal focal lengths as this requires a vertical TEM₀₀-mode size w_y greater than $180\mu\text{m}$ in the Yb:KGW gain medium — a value that would result in strong absorptive losses due to the restrictive $W_y = 200\mu\text{m}$ super-Gaussian vertical pump beam size in the Yb-doped crystal. The clear implication is therefore that the net thermal lens due to the dominant thermal duct is positive; that is, the sum of the refractive index change due to the thermo-optic coefficient and stress for 1040nm laser radiation polarized along the optical N_p -axis (crystal b -axis) is positive. This result is in apparent contradiction to some recent measurements of relatively large negative thermo-optic coefficients in Yb:KGW (19), but is consistent with other determinations of the pump-induced thermal focal length for laser oscillation polarized parallel to the optical N_p -axis (43; 41).

6.1.4 Mode-locked laser operation

In the cavity configuration depicted in Figure 13(a), self-starting mode-locked (ML) operation was observed for output powers greater than $\sim 2\text{W}$ and $z \approx 42\text{cm}$. The maximum (or

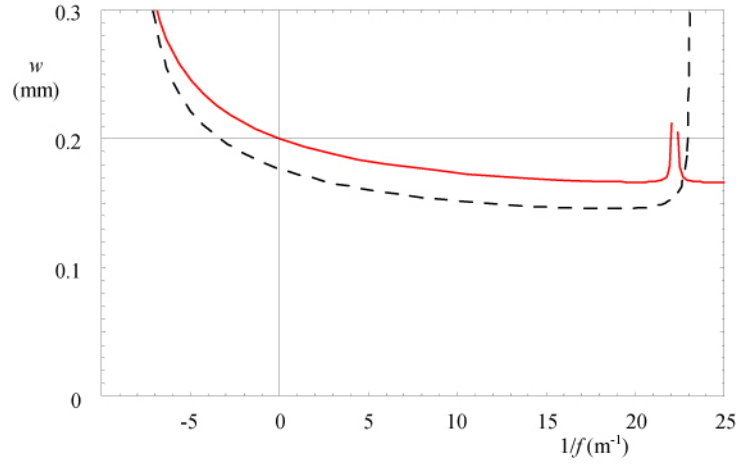
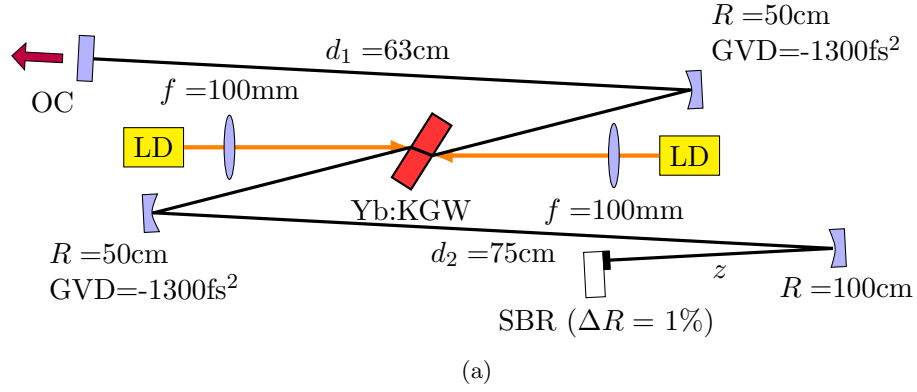


Figure 13: (a) Schematic of the femtosecond TLS Yb:KGW oscillator (LD = laser diode, OC = output coupler, SBR = saturable Bragg reflector). (b) Laser mode size in the center of the Yb:KGW gain medium (w) as a function of the strength of the lensing ($1/f$) in the gain medium (thermal and Kerr) obtained from a resonator stability analysis with $z \approx 42\text{cm}$ for both the tangential (x , red line) and saggital (y , dashed black line) directions. The 0.2mm (HW1/eM) vertical super-Gaussian pump spot size is indicated by the horizontal line.

optimum) mode-locked output power obtained without the emergence of DC spectral components was 3.5W, with a sech^2 pulse duration of 250fs (Figure 14(a)). The insertion of two plane dispersion compensation mirrors each with a GVD of -700fs^2 (Layertec GmbH (5)) into the short arm of the cavity generated higher mode-locked output powers with longer pulse durations. For example, with two reflections off each mirror (an additional -5600fs^2 of round-trip GVD), the pulse duration increased to 347fs (Figure 14(b)) at an optimum mode-locked output power of 5.0W. This trend is consistent with the expected ‘soliton’ modelocking regime; that is, the SBR only initiates the mode-locking mechanism, which is quickly dominated by self-phase modulation in the Yb:KGW gain medium balanced by the net negative GVD in the cavity (22).

The laser is capable of generating shorter ML pulse durations. Replacement of one of the $-1300(\pm 150)\text{fs}^2$ z-fold mirrors with a conventional $R = 50\text{cm}$ high reflector and the insertion of -880fs^2 of negative GVD per round trip (a pair of -220fs^2 dispersion compensating mirrors) generated $\sim 220\text{fs}$ pulses at 24A of diode current, 2W of output power, and a SBR position $z = 43.2\text{cm}$. However, ML operation was significantly less stable under these conditions, indicating that either the cavity is operating close to the net zero GVD point or that the finite gain bandwidth is influencing the ML operation. We also note that in this case the optimum SBR position z is larger than that for higher power 3.5W ML operation with a negative cavity GVD of $-5,200\text{fs}^2$ per round-trip (Figure 14(a)), but is always less than the 50cm focal length of the concave high reflector. This is due to the need to match the absorption-induced thermal bowing of the SBR (i.e., the radius of curvature of its front surface mirror) to the radius of curvature

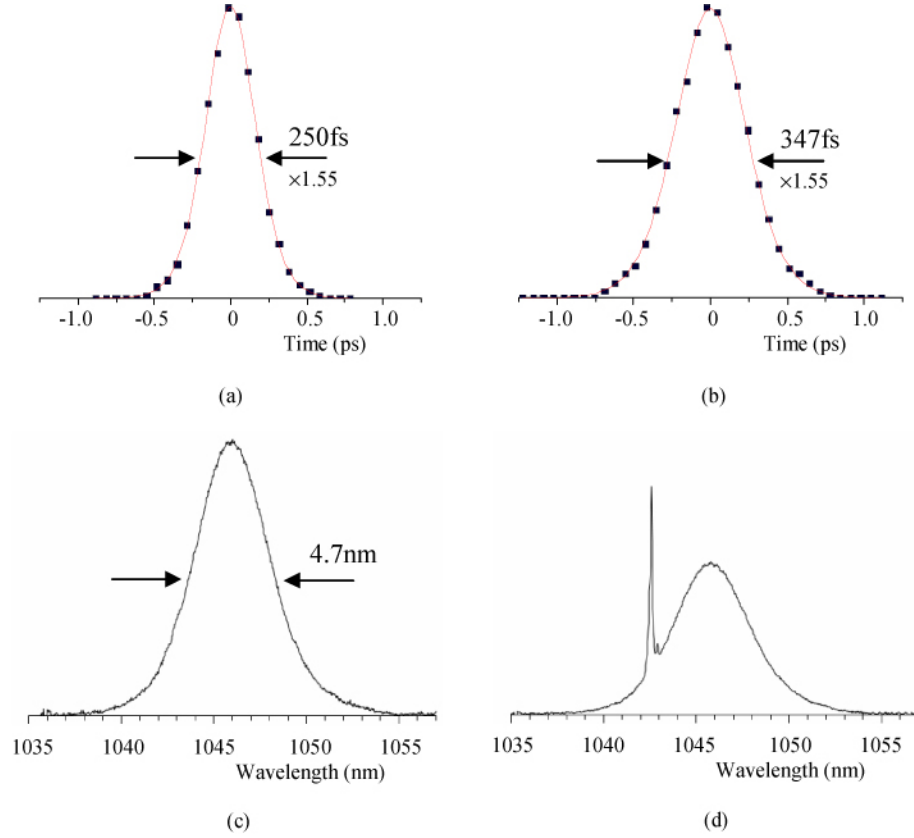


Figure 14: Second harmonic autocorrelation measurements and output spectra of the ML Yb:KGW laser; (a) the 250fs laser pulse duration (and fit assuming a sech^2 pulse shape) for the cavity depicted in Figure 13(a) at an output power of 3.5W, (b) the 347fs pulse duration (and fit assuming a sech^2 pulse shape) obtained with an additional -5600fs^2 of round-trip GVD at an output power of 5W, (c) the 4.7nm full-width half maximum spectrum associated with the 250fs ML pulse of (a), and (d) spectral output for the ML resonator of Figure 13(a) at a laser power of 3.7W.

of the intra-cavity laser mode (90). In general, good ML operation is achieved with the SBR positioned within $\pm 1\text{cm}$ from the optimum z distance.

Figure 15 shows the laser's output power as a function of diode current for the cavity configuration depicted in Figure 13(a); a total negative GVD of $-5,200\text{fs}^2$ per round-trip and a 7% transmission output coupler. Soliton mode-locked (ML) operation is observed for diode currents greater than 23A, corresponding to a continuous-wave (CW) output power of 1.8W. Between diode currents (output powers) of 23 and 25A (1.8 and 2.3W), the resonator operates mainly in the CW mode, but will transition to ML operation upon being subjected to a perturbation. The switching to ML operation is accompanied by a 250mW increase in output power indicating a higher cavity Q for ML operation. This is consistent both with the laser accessing more of the available inhomogeneous gain bandwidth and with our resonator design favoring operation with a strong Kerr lens in the Yb:KGW gain medium. Given a value of nonlinear refractive index $n_2 \approx 15 \cdot 10^{-16}\text{cm}^2/\text{W}$ for 1040nm radiation polarized parallel to the KGW crystal's optical N_p -axis (64; 93; 104) and a calculated peak pulse irradiance of $\sim 4\text{GW}/\text{cm}^2$ in the gain medium at 24A, we expect a Kerr lens strength of approximately 2m^{-1} . From Figure 13(b), we see that the resulting increase in the strength of the lensing in the Yb:KGW crystal will result in a reduction of the laser mode size in the gain medium, which produces a better spatial match to gain duct produced by the laser diode pumps (less absorptive loss), thus generating an increase in output power.

Above a diode current of 25A (i.e., an output power of 2.3W), the laser exhibits spontaneous self-starting ML operation. At a diode current around 29A, a maximum (or optimum) average

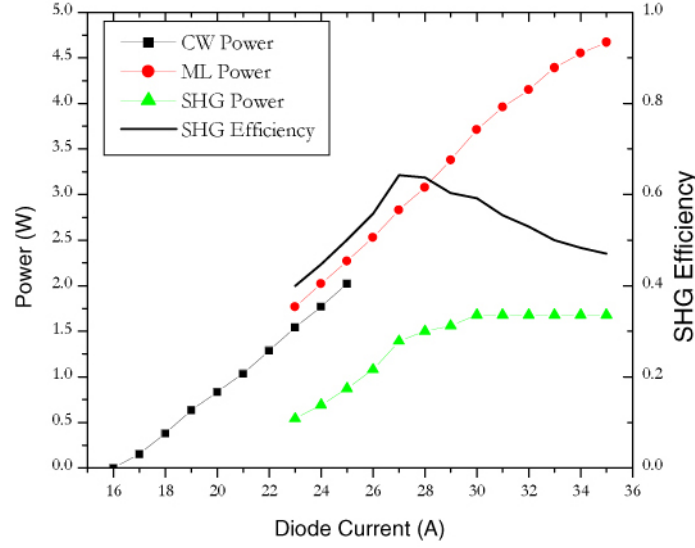


Figure 15: Performance of the diode-pumped, TLS, Yb:KGW laser (in the cavity configuration of Figure 13(a)) as a function of applied diode current: continuous-wave (CW) output power (black squares); mode locked (ML) output power (red circles); frequency doubled power (green triangles); and second harmonic generation (SHG) efficiency (line).

mode-locked output power of $\sim 3.5\text{W}$ is obtained. The 250fs pulses generated at this output power (Figure 14(a)) correspond to a Kerr lens strength in the Yb:KGW crystal of $\sim 4\text{m}^{-1}$, which is readily accommodated by the resonator design (Figure 13(b)). For this $\sim 3.5\text{W}$ ML laser with a negative cavity GVD of $-5,200\text{fs}^2$ per round-trip, the full-width at half maximum of the mode-locked spectrum centered at 1046nm is 4.7nm (Figure 14(c)). The laser is therefore generates pulses with a time-bandwidth product very close to the Fourier limit of 0.32 for a sech^2 pulse shape. At output powers greater than 3.5W, a DC spectral component emerges at the short wavelength end of the ML spectrum (Figure 14(d)) and there is a slow roll-over in the laser output power (Figure 15). This trend is expected for a Yb:KGW soliton ML laser; in

this case, the soliton power limit being reached at about 29A, and the asymmetric spectral gain of Yb:KGW forcing excess CW laser power oscillation at wavelengths shorter than the peak of the ML spectrum. Similar laser performance is observed with the insertion of an additional $-5,600\text{fs}^2$ of cavity GVD per round trip, which generates 347fs sech^2 pulses (Figure 14(b)); that is, a DC spectral component appears on the short wavelength side of a narrower $\sim 3.5\text{nm}$ ML spectrum at output powers above 5W.

6.1.5 Frequency doubling

For most photoemission sources, the fundamental laser photon energy of 1.19 eV does not provide enough energy to excite electrons above the vacuum level, either for single or two-photon emission (35; 47; 34). By appropriate application of crystals with strong non-linear properties, two photons at frequency ω may be converted into one photon at frequency 2ω (95). Since these higher harmonics will be necessary for stimulating photoemission it is important to optimize and characterize the efficiency of this process.

The ML output from the femtosecond Yb:KGW laser with a net negative GVD of $-5,200\text{fs}^2$ per round-trip was initially frequency doubled in a critically phase-matched, 2mm, Type I Lithium triborate (LBO) crystal. The crystal is uncoated and cut for frequency doubling with the fundamental p -polarized radiation at 1046nm incident at Brewster's angle — a geometry that ensures both minimum loss for the fundamental radiation and, more importantly, a high damage threshold. The doubling crystal is positioned at the focus of a z -fold comprising a 1040nm high reflector with a radius of curvature of 75mm followed by a collimating mirror with a radius of curvature of 100mm reflective at both the fundamental and second harmonic

wavelengths. At the 3.5W ML output power, with a pulse duration of 250fs, the estimated focal irradiance for the fundamental is $\sim 50\text{GW}/\text{cm}^2$ in the LBO doubling crystal. Two plane dispersion compensation mirrors, each with a GVD of -220fs^2 (Layertec GmbH (5)), inserted before the z -fold doubling geometry compensate for propagation through the 6mm-thick fused silica output coupler, reflections off standard optics, etc. After the collimating mirror, a standard flat dichroic beamsplitter then separates the reflected s -polarized 523nm radiation from the transmitted p -polarized fundamental.

This frequency doubling geometry for LBO is chosen to be close to the optimum for efficient short pulse doubling (105; 89) defined by limits imposed by group-velocity walk-off between the fundamental and second harmonic pulses, spatial walk-off in the critical phase-matching, and the ratio of the confocal parameter of the focused fundamental wave to the LBO crystal length. In addition, the z -fold configuration allows for astigmatism compensation (e.g., due to the Brewster LBO crystal) of the second harmonic output by adjustment of the angle of incidence on the second collimating mirror.

Figure 15 shows the resultant frequency-doubled green power for the ML Yb:KGW laser. The measured average power at 523nm increases rapidly from 0.5W at the 23A mode-locking threshold to over 1.3W at a diode drive current of 27A. At and above 30A, the second harmonic power saturates at 1.65W — an effect that is clearly consistent with the observed emergence of a DC spectral component at diode currents above 29A since only the ML pulse will be efficiently frequency doubled. Also plotted in Figure 15 is the frequency doubling efficiency, which is calculated taking into account the 17% loss suffered by the s -polarized 523nm radiation

upon exiting the Brewster-cut LBO crystal and the 4% loss (to diagnostics) of the fundamental radiation prior to the z -fold doubling geometry. The maximum doubling efficiency of over 60% occurs at 27-28A of diode drive current when the ML laser output power is ~ 3 W. At a ML output power of 3.5W (29-30A), the frequency doubling efficiency is still $\sim 60\%$ and slowly decreases above 30A as the DC spectral component absorbs the residual power above the soliton power limit.

6.1.6 Long-term Performance Enhancements

Since the initial construction and characterization of this laser system, described above, several improvements have been made, primarily to improve the long-term mode-locking stability of the laser. Due to the laser's role as a component of the larger UEM system, its stability is a tremendously important factor, both for repeatability of measurements and suitability for use in a user instrument.

The second harmonic generation system now employs a 3mm non-critically phase matched LBO crystal (7). This change has two benefits. First, in this geometry, the walk-off angle between the fundamental and second harmonic is zero, while the group velocity mismatch of 150fs (~ 50 fs/mm) is still less than the pulse duration 250fs. Second, because in this case, non-critically phase matching requires that the crystal is held at an elevated temperature of 176°C , the deleterious absorption of water in the hygroscopic LBO crystal is prevented. Additionally, in the place of the curved mirrors originally employed, the second harmonic system now uses 75mm lenses to focus the laser into the crystal and collimate the output.

Although the laser system had been relatively robust, maintaining mode-locked operation was initially problematic. A cover was added above the laser cavity to prevent dust and air currents from interrupting mode locking. More importantly, a 1.4mm aperture (approximately four times the HW1/eM beam width at the output coupler) was added to suppress higher-order transverse modes. As this is an additional loss in the cavity, the output coupler was changed from 93% to 95% reflectivity to maintain the soliton mode-locking power. These changes have greatly improved the mode-locking stability.

The laser now regularly operates at $1.9(\pm 0.1)\text{W}$ in mode locked operation with 250fs pulse durations, with minimal regular maintenance. The 40-50% efficient second harmonic generation yields 0.8-1W of green output. The green radiation can be again doubled to yield 261nm ($\hbar\omega = 4.75\text{eV}$) ultraviolet (UV) radiation in a 6mm β -Barium borate (BBO) crystal, though the group velocity mismatch results in a 4ps pulse duration. All data presented in this thesis has been acquired subsequent to these performance enhancements.

6.2 Column Design and Construction

Apart from the laser system, the majority of an Ultrafast Electron Microscope column is either vacuum hardware or contained within the vacuum system. The vacuum chamber itself is almost entirely standard 4.5in ConFlat (CF) hardware. Much has been purchased from off-the-shelf hardware suppliers. Some of the more specialized chamber components have been fabricated in-house or purchased from Kimball Physics Inc.

Kimball's line of Multi-CF hardware has been especially useful in building the prototype column. The main chamber is a 4.5in "spherical cube," a large stainless-steel sphere which has

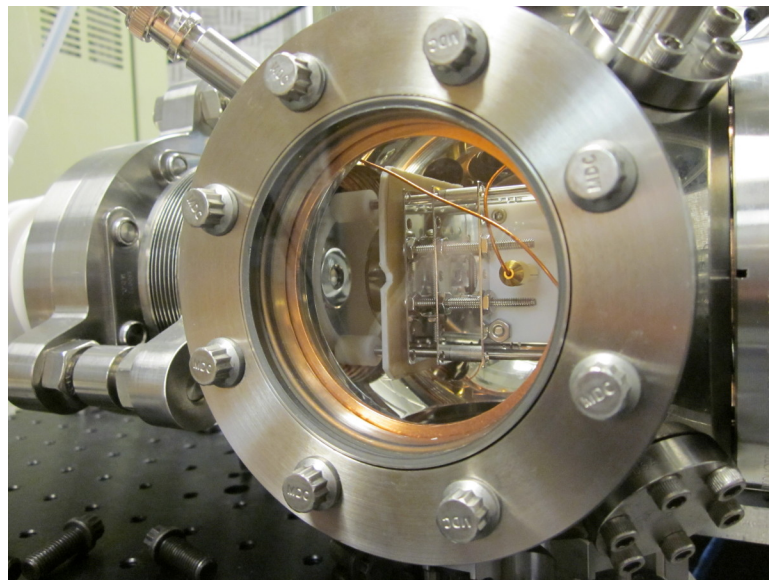


Figure 16: Assembled side view of the main chamber section of the UEM column at UIC. To the left are the high-voltage passthrough and “port aligner” to which the cathode is mounted. Visible inside the window are the cathode Wehnelt and photocathode (left), the side of the anode, and the side of the deflector plates assembly just after the anode (right). The anode and plate-assembly are mounted by the “eV Parts” system attached to the main chamber. The wires and connectors supplying the voltage to the plates are also clearly visible.

six 4.5in ConFlat ports oriented as a cube, with another eight 1.33in ports on the corners of the cube. All ports on Multi-CF hardware also contain a set of grooves designed as mounting points for a system of erector-set-like equipment called “eV Parts.” This system is used to mount the accelerator anode and the deflector plates which are both to be described later.

6.3 Accelerator Design

The acceleration region of our prototype UEM system has several features which are unique in comparison to standard electron guns. As discussed in Chapter 5, notable requirements for a UEM electron gun include the need to handle a large photoemission area and yet to retain all of the electrons; it may not employ a pin-hole to selectively clean the electron beam. These necessities lead to several additional criteria. The system must first be able to accept the large laser spot size needed to generate the electron beam. Then, in order to accommodate this large electron pulse, both the cathode Wehnelt and anode aperture must be similarly large; in fact, the beam size at the anode aperture will typically be larger than at the emission source due to transverse beam expansion during acceleration. Also, care must be taken to ensure a relatively uniform electric field for acceleration of the pulse. While in transit from the cathode to the anode, this large beam is more susceptible to non-uniformities in the electric field given that it will span a larger volume of the acceleration region than the thin beams used in conventional TEM.

These requirements led to the fabrication of cathode/Wehnelt and anode pair based on the design of Togawa *et al.* (100) (pictured in Figure 17). A schematic of this design, overlaid by a Finite Element Model (FEM) simulation of the electric field, is shown in Figure 18. The

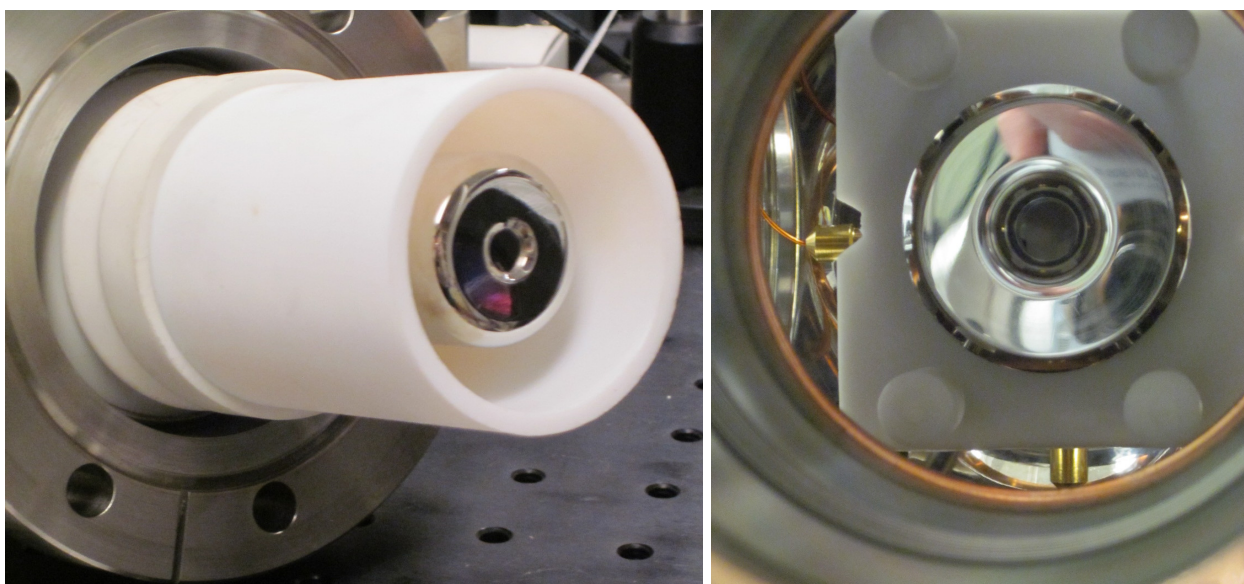


Figure 17: Pictured are the cathode (left) and anode (right) of the accelerator built at UIC from a design by Togawa *et al.* (100). The photocathode is visible in the cathode Wehnelt aperture. The anode is viewed as installed in the column, through the opened port normally occupied by the cathode and high voltage feedthrough. The white material seen in both images helps to prevent electrical arcing under high voltage.

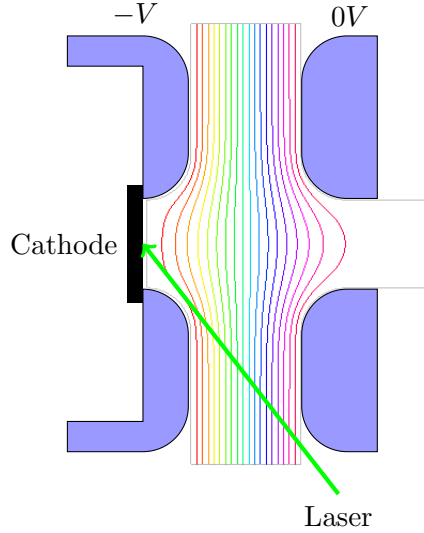


Figure 18: Schematic of the employed Togawa-inspired cathode ($-V$) and anode ($0V$, ground) pair. The emission source is inserted behind the cathode Wehnelt. The separation of the cathode and anode is adjustable to allow a greater range of input laser angles if needed. Also shown are simulated equipotential lines generated by FEM modeling. The acceleration gap is modeled as having linear potential along an edge at a very large width.

simulation was performed using **FreeFEM++**, a free finite element partial differential equation solver and meshing toolkit (<http://www.freefem.org/ff++/index.htm>). The FEM simulation modeled the features of the anode and cathode, while emulating gap walls at infinity by placing a linear potential on gap edges at a large distance. From the field equipotentials, it is clear that this design has a consistently flat electric field for large displacements off the central axis. Since the shape of the field is scale independent, the schematic shows that the aperture width and laser acceptance concerns are easily satisfied for an appropriate choice of scale.

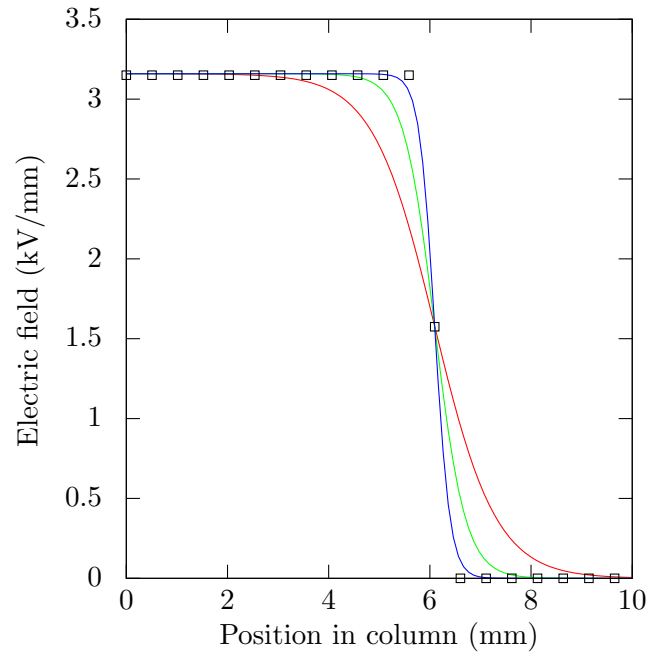


Figure 19: An example of a tanh form acceleration region (overall length 6.35mm) for three different “sharpness” values, the same data as in Figure 3(a). The square data points represent the on-axis electric field data from FEM simulations.

Figure 19 compares the FEM computed electric field to the form asserted for the AG model (Equation 3.48) for several values of the sharpness parameter s ; the lines are the same as in Figure 3(a). As derived in Section 3.4.4, the change of electric field strength near the anode will cause some divergence of the electric field which, in turn, will cause a divergence of the beam. Future work will include investigating the designs of Butler which may be able to build in an intrinsic lensing to compensate for this effect.

A gross realignment of the cathode and anode is sometimes necessary to direct the emitted beam down the center axis of the column. To facilitate this in the prototype column, the photocathode and Wehnelt are mounted on the end of the high voltage feedthrough which is, in turn, mounted on a two axis alignment mechanism. Although this mechanism, called a “port aligner,” is typically used to couple two non-colinear vacuum ports, for use in this instrument it has been modified to be able to manually adjust the aligner (i.e. cathode position) during use. In contrast, the anode is mounted to column using Kimball Physics’s “eV Parts” fixed mounting systems. These strictly manufactured mounting hardwares ensure that the anode is properly aligned with the remainder of the microscope column. Thus, by iteratively repositioning the input laser on the cathode and then the gun cathode alignment, the beam may be walked to pass as near as possible down the axis of the column.

6.4 Magnetic Lenses

In many ways, an electron beams and electron microscope columns can be thought of in terms of an optical equivalents. Of course there are notable exceptions; photons don’t repel each other; photon energies are hard to change. Electron optical systems do have an element

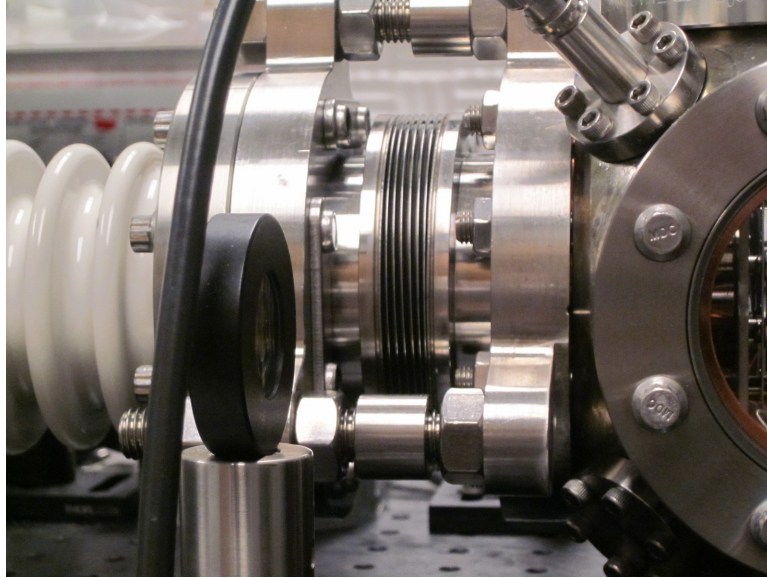


Figure 20: The high voltage passthrough (left) is mounted on the main chamber (right) by a “port aligner” which has been modified to allow coarse alignment of the cathode (mounted to the high voltage) and anode (mounted in the chamber).

which is analogous to the optical lens, in this case using magnetic fields rather than glass. The magnetic lens is a common element in electron microscopes and other electron-optical systems.

Magnetic lenses built for use in Ultrafast Electron Microscopy will be subject to the some unique design criteria. First, because of the considerations presented in Chapter 5, the beams are likely to be much larger than in conventional electron microscopy and thus a UEM will need large-aperture lenses. Second, and more importantly, near a lens crossover (i.e. focus), the charge density can increase rapidly. This charge density can lead to an unacceptable amount of space-charge interaction. These effects have been explored in Sections 4.2 and 4.3. The lenses

I present in this section were designed, in part, using information computed by the extended AG model (Section 3.4.2) in order to address these concerns.

6.4.1 Design

Discussion of the formal mathematics of magnetic lenses can be found in Section 3.4.2. While in principle one could design a magnetic lens using Equation 3.30 and Equation 3.31, the process wouldn't be very practical or instructive. Further — as suggested by the use of the auxiliary field H field in Equation 3.31 — better performance of the lens can be achieved by concentrating the field using materials with high magnetic permeability. These materials, called “magnetic shielding” since they capture the magnetic field lines, can direct the field lines to a small gap, known as the “pole-piece gap.” The field lines exit the shielding in the gap and it is this field that acts as the lens. This gap can be much smaller than the total width of the coil turns, and yet contain a field strength commensurate with that of the full coil. This geometry is presented schematically as Figure 21.

Figure 22 shows a schematic of the lens designed and built for the UEM at UIC. The central drift tube is made of stainless steel having a magnetic permeability of 1, thus magnetically not involved in the field shaping. In this way only the inner bore of the tube may be in vacuum thus minimizing necessary welding. The outer diameter of tube is machined down to $D = 2R = 0.5\text{in}$, though a disk of larger diameter, and length $S = 0.1\text{in}$, is left at the midpoint, which will separate the shielding material and be the pole-piece gap.

The high magnetic permeability shielding is made of ten pieces. There are two end pieces which are revolution solids of an “L” shaped profile. These ends slide together over the drift

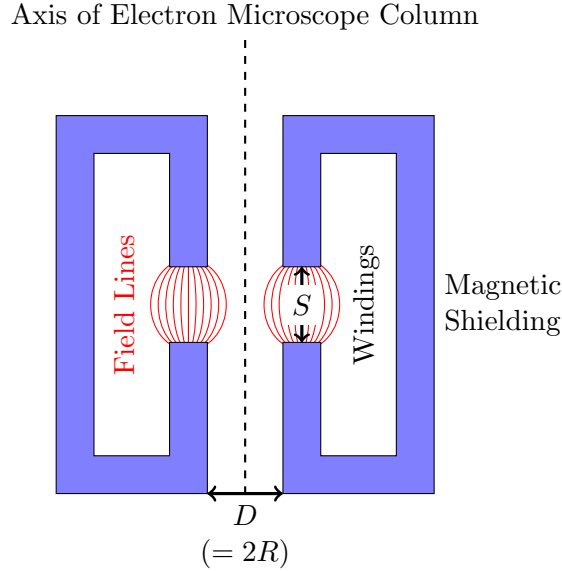


Figure 21: Side-view schematic of a generic magnetic lens with a pole-piece. The windings (current loops) are contained within the shielding. The magnetic field created by these windings is contained inside the shielding except in the gap.

tube until touching the disk at the midpoint; the disk is of the proper outer diameter to match the shielding's smaller outer diameter. The combination of the two ends and this disk make a "U" shape which contains the windings. The top of the each end's large outer disk (the walls of the winding container) are flattened on eight sides. These are the mount points for eight bridge pieces which connect the ends to complete the field-capturing shielding loop. The gaps between the shielding bridges also allow for direct air cooling of the magnetic coils (see Section 6.4.2).

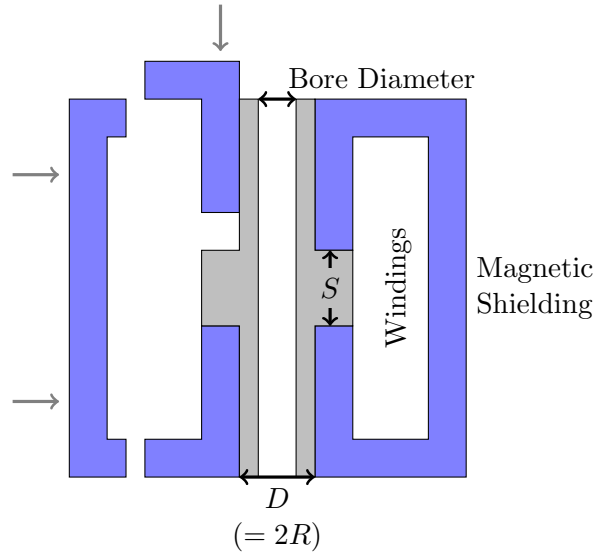


Figure 22: Side-view schematic of the magnetic lens with a pole-piece designed for the UEM at UIC. On the center axis is the inner drift tube, with pole-piece gap separation disk. The end pieces are shown top and bottom, bridges are on the left and right. The left side shows a bridge piece and one end before assembly. Note that this figure is not drawn to the scale of the lenses at UIC, but rather to match the general schematic in Figure 21.

El-Kareh and El-Kareh provide an analysis for symmetric lenses with magnetic shielding and a pole-piece (see Ref. (37) chapter 8, with the most useful information being in section 8.7). They define two parameters,

$$k^2 \equiv \frac{e}{8mV_r} B_0^2 R^2 \quad (6.4)$$

and

$$\beta \equiv k^2 V_r / (NI)^2, \quad (6.5)$$

where N is the number of loops, I is the current in a single loop, B_0 is the maximum axial magnetic field strength, R is the bore radius and V_r is the relativity corrected acceleration potential, given by

$$V_r = V \left(1 + \frac{0.978 \cdot 10^{-6}}{\text{Volt}} V \right). \quad (6.6)$$

Using the provided tabulated results, and for a choice of parameters one can determine the number of ampere-turns (NI) to create a certain focal length. Since the drift tube has an outer diameter $D = 0.5\text{in}$ and the pole-piece gap length is $S = 0.1\text{in}$, the lens has a ratio $S/D = 0.2$. By their table 8.2a this results in $\beta = 0.0146$. Then, to create a focal length of 4in ($f/R = 16$) table 8.13 in Ref. (37) gives a value for $k^2 \approx 0.06$. Finally substituting this value into Equation 6.5, with $V = 30\text{kV}$ ($V_r \approx 30.88\text{kV}$), one can deduce that $NI \approx 356\text{A}$.

For the UEM system at UIC, two of these lenses are employed to manage the divergence created by an RF cavity and the anode aperture, then focus the pulses to a focal spot. These lenses are positioned one before and one after the RF cavity, forming a lens system of a combined effective focal length; the two lenses are wound oppositely to counteract beam rotation. For

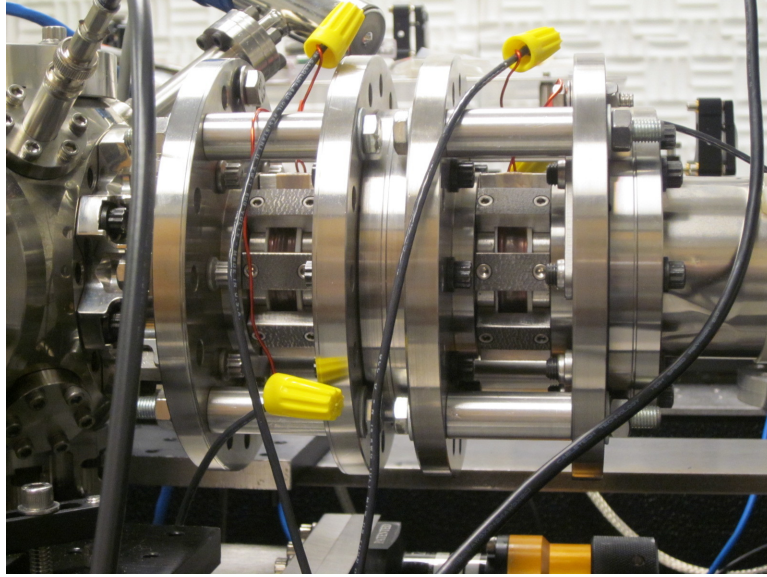


Figure 23: Side-view of the two custom large-bore magnetic lenses designed and built at UIC, seen installed in the prototype UEM. The coils are visible in the gaps between the high permeability shielding “bridges.” The bridges are attached to the tops of the end pieces by bolts to complete the shielding loop. The outer (larger) plates and struts are for structural integrity only.

the purposes of design, one can make a reasonable approximation that the two lenses together provide the total necessary number of amp-turns. As each lens has 100 turns, a current of only about 2A is needed to drive the two lenses in series to attain a 4in focal length. A picture of this system is shown in Figure 23. In that picture the two lenses are shown, however a placeholder is shown inserted between them rather than an actual RF cavity.

6.4.2 Thermal Properties

As the lenses have no active cooling system, it was prudent to characterize the thermal response to a moderate current load. Resistance of metals changes as a function of temperature

by $R = R_0[1 + \alpha(T - T_0)]$, where α is a material constant; for copper, $\alpha = 3.9 * 10^{-3}\text{K}^{-1}$. One can calculate the temperature increase of the system by monitoring the change in resistance. Maintaining a constant current of 4A through the lens, the voltage drop increased from 1.22V ($R_0 = 0.305\Omega$) to 1.25V ($R = 0.3125\Omega$) as the lens warmed. The resultant temperature increase is only $T - T_0 = 2\text{K}$. This result is easily confirmed manually; the oxygen-free copper wire coils remain cool to the touch under these operating conditions.

6.5 Deflection Plates

In order to direct the beam down the column, custom large area deflector plates are employed in conjunction with the gross accelerator alignment mechanism described earlier. Four plates are arranged on a hollow tube with a square profile, one on each side. One of each pair is held at ground while the other has a variable potential. By varying each potential the beam may be turned in flight.

A schematic description of such a system is shown in Figure 24. To estimate the required voltage on the plates V needed to correct for a lateral velocity v_x , consider the applied impulse provided to the beam by the plate's force F of the electric field,

$$F\Delta t = m\Delta v \tag{6.7}$$

$$\frac{eV}{d} \frac{L}{v_z} = m\Delta v_x, \tag{6.8}$$

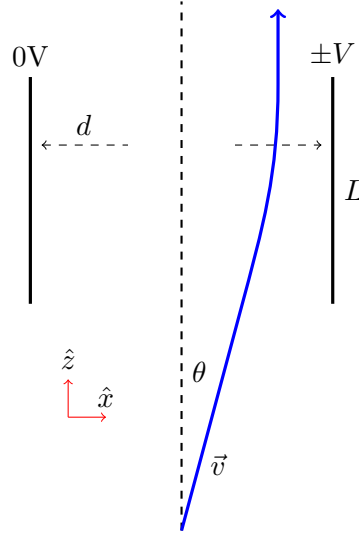


Figure 24: Schematic diagram of one pair of deflection plates. The blue ray represents the path of the pulse as a whole (not to be confused with the plot of a lens).

where (as seen in the figure) L is the length of the plate (in the direction of travel \hat{z}) and d is the separation of the plates. If the beam has a velocity v_z down the axis of the column, then in the small angle approximation, the angle that the plate may correct for is approximately

$$\theta = \frac{\Delta v_x}{v_z} = \frac{e}{m} \frac{L}{d} \frac{V}{v_z^2}. \quad (6.9)$$

Using this result, when $L \sim d$ and $v_z = c/3$ a voltage of 1kV will deflect the beam approximately one degree. These plates are, therefore, useful as a fine beam adjustment, as contrast to the coarse adjustment provided by manually aligning the acceleration gap.

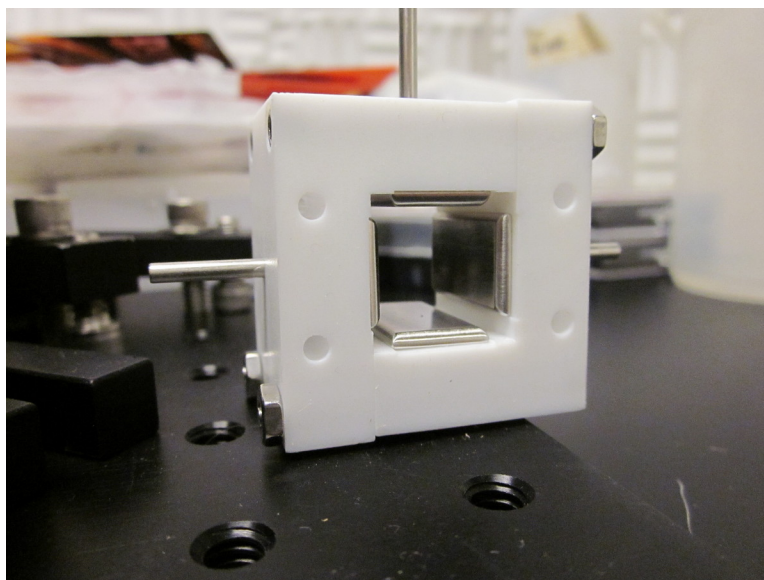


Figure 25: Picture of the custom built deflector plates for use in the UEM at UIC. A pair of vertical and horizontal plates are mounted in a non-conductive housing. Each plate has a pin for connecting to voltage or ground. Clearance drilled holes allow mounting onto the “eV Parts” cage inside the chamber.

CHAPTER 7

PHOTOCATHODE ENGINEERING

The spatial quality of the sources for UEM and UED are often characterized in terms of their emitted electron beam's normalized transverse rms emittance (34; 45); $\varepsilon_T = \Delta p_T \Delta x / (mc)$, where $\Delta p_T = \sqrt{\langle p_T^2 \rangle}$ is the rms transverse momentum of the beam, $\Delta x = \sqrt{\langle x^2 \rangle}$ is its size (cylindrical symmetry assumed), and m is the electron rest mass and c is the speed of light in vacuum. This quantity is conserved under free-space propagation and perfect lensing, but may increase due to lens aberrations (78). As I have discussed in Chapter 5, an electron beam (or in the case of UEM, a pulse) with a lower transverse emittance will result in higher quality images, however since this quantity is conserved, the only chance to minimize this quantity occurs upon emission. As a reduction in the source size Δx_0 is limited either by the attainable diffraction-limited incident laser pulse focusing or by the short-pulse Child's Law (screening of the electron gun's acceleration field) (101), significant improvements in the performance of scientific instruments employing pulsed electron sources through a reduction in their spatial emittance ε_T (and consequent increase in brightness (17)) may only be possible by decreasing the initial rms transverse momentum Δp_T of the electron source — an intrinsic property of the emission source (34; 45).

To address this need, I have experimented with many candidate photocathodes, which implement a variety of different photoemission processes. In this chapter, I will present an example of several of these different processes, discuss its prospects for reducing the transverse

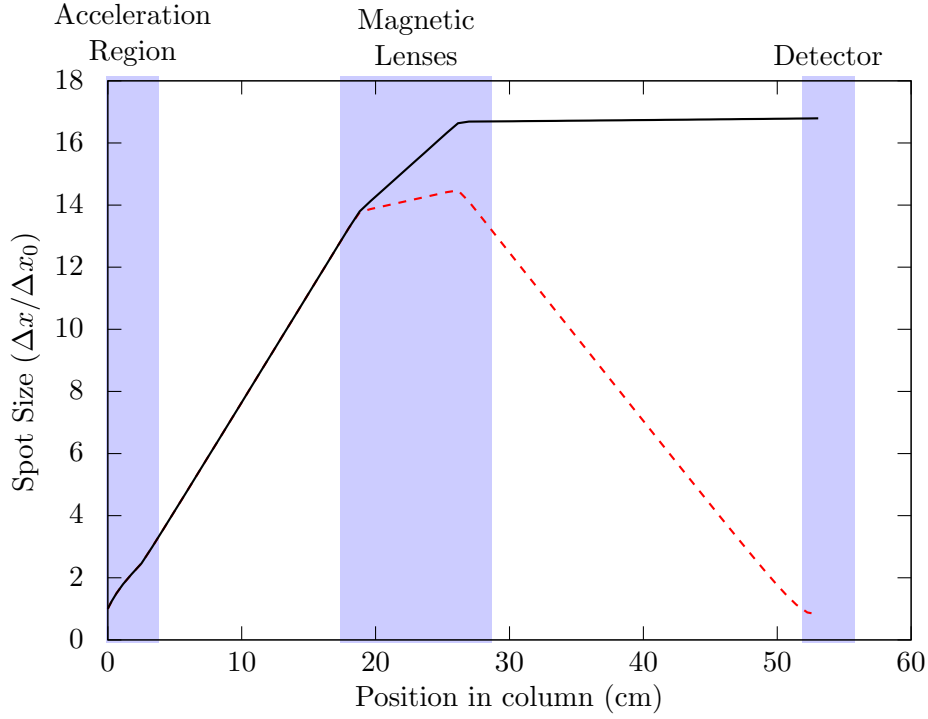


Figure 26: Simulations of the electron pulse propagation through the apparatus using the extended AG model. Solid line: The spatial beam width (normalized to that at the photocathode Δx_0) with the magnetic lens strengths adjusted to ensure that the detector is at their back focal plane (Fourier plane). Dashed line: The case when the strength of the magnetic lenses is increased by a factor of two to focus the electron beam on the YAG scintillator detector.

emittance and finally assess its utility as an electron source for UEM. I will then outline some future research directions that the group at UIC will continue to pursue. Since this is the most active current field in our group's research, indeed some very new results are presented near the end of the chapter, future plans are continuously evolving.

7.1 Experimental Methodology

Figure 26 depicts the experimental technique used to determine directly the transverse momentum distributions (and hence Δp_T) of the laser-driven electron sources. Though many of the experimental components have been described in detail in Chapter 6, for convenience I will briefly summarize them again here. The primary laser radiation source for the studies is a home-built, diode-pumped and thermal-lens-shaped, femtosecond Yb:KGW oscillator (16) delivering 250fs duration pulses at 1047nm and a 63MHz repetition rate. This 2W average power laser is frequency doubled in a 3mm lithium triborate (LBO) crystal with 50% efficiency to yield ~ 200 fs green pulses at 523nm (photon energy, $\hbar\omega = 2.37\text{eV}$). Further doubling with a cylindrical focusing geometry in a 7mm β -barium borate (BBO) crystal yields 261nm ($\hbar\omega = 4.75\text{eV}$) UV pulses with a duration of ~ 4 ps (due to the 600fs/mm group velocity mismatch between the green and generated UV). Both the green and UV laser pulses are focused with 30cm focal lenses onto the photocathode in a 20kV electron gun at an angle of incidence of $60(\pm 5)^\circ$, which improves the coupling of the p -polarized laser radiation into the photocathode surface (17). The electron gun design is based on the that of Togawa *et al.* (17; 100) and has an acceleration gap of $25(\pm 2)\text{mm}$. After acceleration in the DC photo-gun, the electrons pass through a set of electrostatic deflection plates to ensure that the electron beam passes, as close as possible, axially through the center of two, 6.35mm-bore, thin and round magnetic lenses with counter-propagating currents to minimize image rotation effects. A YAG scintillator placed 27.5cm after the second magnetic lens detects the spatial electron beam profile, and its visible fluorescence is 1:1 imaged onto a CCD detector with $5.4\mu\text{m}$ pixels.

To ensure that the transverse momentum distribution is monitored, the YAG scintillator must be positioned at the back focal plane (the Fourier plane) of the lens system. This is readily achieved by appropriate adjustment of the current I in the magnetic lens coils; specifically, after determining the current required to focus the electron beam onto the scintillator, optical imaging relations together with the I^2 dependence of the magnetic lens strength are used to find the current that ensures that the average lens to scintillator distance equals the focal length of the lens system. Simulation of the experimental apparatus (employing the extended AG model, see Section 3.3), confirms that this procedure places the YAG scintillator at the back focal plane of the lens system to within a $\pm 0.5\text{cm}$ error (Figure 26). This simulation also confirms that for our experimental conditions (less than 5,000 electrons/pulse and $\Delta x_0 > 30\mu\text{m}$) space-charge effects do not influence the observations. Additionally, and as expected from optical considerations, the modeling shows that the spatial beam size in the Fourier plane is independent of Δx_0 , the rms laser spot size incident on the photocathode (i.e., the electron source size). All of the results in this chapter use the Fourier plane beam size as a measure of the initial rms transverse momentum Δp_T .

7.2 Single-photon Photoemission from Flat Metal Photocathodes

Single-photon photoemission is the most common photoemission process and the easiest to explain. As described by Einstein in his famous paper on “the photoelectric effect” (36), as it is colloquially known, if an electron absorbs a photon whose energy is sufficient to promote the electron above the local vacuum level, it becomes free to leave the host material. The material dependent minimum energy needed to eject an electron is termed its “work function” Φ . Any

additional energy above the work function remains with the ejected electron, usually in the form of kinetic energy, and is called the “excess photoemission energy” ΔE ; for single photon photoemission, using a laser of frequency ω (photon energy $\hbar\omega$), this is simply,

$$\Delta E = \hbar\omega - \Phi. \quad (7.1)$$

The efficiency of photoemission η_{PE} , when ΔE is small compared to Φ may be written as (39; 34; 67),

$$\eta_{PE} = A(1 - R)\Delta E^2, \quad (7.2)$$

where A is a material parameter (typically of the order of $\sim 10^{-4}\text{eV}^{-2}$), and R is the photocathode surface reflectivity, which is itself a function of the polarization, frequency and angle of the incident light.

An example of single-photon photoemission is presented in Figure 27, wherein a sample of polished tungsten (W), having a work function $\Phi \approx 4.3\text{-}4.5\text{ eV}$ (108), is used as a photocathode; when paired with our $\hbar\omega = 4.75\text{ eV}$ photon energy laser (see Section 6.1) the excess photoemission energy $\Delta E \approx 0.35\text{ eV}$. The linear dependence of the electron yield (circles) on the laser pulse energy is indicative of a single photon process, as expected since each absorbed photon may eject one electron. In this experiment, the yield is determined by integrating the total counts recorded on the CCD detector and therefore is only a relative measurement. The fact that the Fourier plane spot-size (squares), directly related the initial transverse momen-

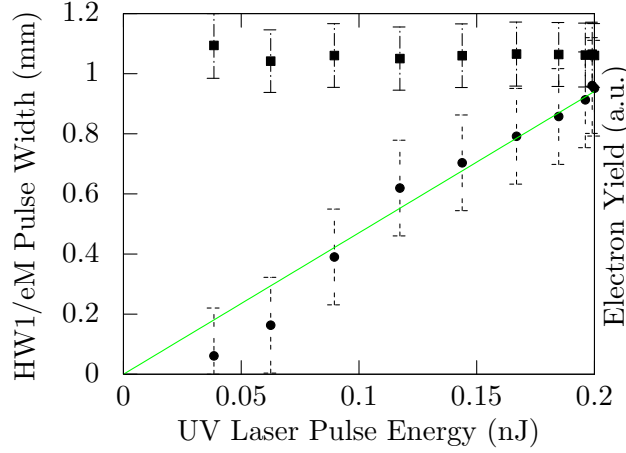


Figure 27: Single-photon photoemission from Tungsten. The good linear fit (green) to the relative electron yield (squares) indicates a single-photon process. The Fourier plane spot size (squares), related to the initial transverse momentum variance, do not depend on laser pulse energy, as expected.

tum variance Δp_T , is unchanged over the full range of laser power is also expected, since by $\Delta p_T = \sqrt{m\Delta E/3}$ (34), Δp_T only depends on ΔE .

In order to improve performance, one must be able to minimize Δp_T without negatively affecting the photoemission efficiency, and thus electron yield. For single-photon photoemission, although the polarization-dependent reflectivity can be tweaked to improve performance slightly (17), due to the quadratic dependence of the efficiency on excess photoemission energy (94), any reduction in Δp_T gained by reducing ΔE will be mitigated by a large drop in electron yield. For this reason, as it stands currently and as we have already seen in Section 5.3, flat metal photocathodes employing single-photon photoemission are not likely to be useful for UEM. However, as I will show in Section 7.6, this does not quite tell the complete story.

7.3 Two-photon Assisted Thermionic Emission

Although single-photon photoemission is more efficient than multi-photon photoemission, the concept remains the same; an electron in the photocathode must absorb enough energy to exceed the vacuum level. In multi-photon photoemission this energy is attained by absorbing multiple photons. As this is more likely to occur when more photons are present, the efficiency, and thus the yield, is proportional to the laser intensity to the power of the number of photons required. Two-photon photoemission, therefore, will have yield that is quadratic in laser intensity (I^2).

Two-photon assisted thermionic emission (2PTE) occurs when two photons provide nearly enough energy to emit a cold electron, and therefore a hotter electron, in the tail of the Fermi distribution, may have enough energy to be emitted (108). Of course this is even less efficient than direct two-photon photoemission, but as three-photon photoemission goes as I^3 , 2PTE will still be the dominant photoemission mechanism. For thermionic emission from electrons at a temperature T_e , the rms transverse momentum Δp_T is given by

$$\Delta p_T = \sqrt{mk_B T_e}, \quad (7.3)$$

where k_B is the Boltzmann constant (34; 45). Since a high laser intensity is required to drive 2PTE, the laser itself will heat the electrons, therefore, we expect the measured Fourier plane spot size to grow as incident laser pulse energy increases, assuming that the laser pulse duration

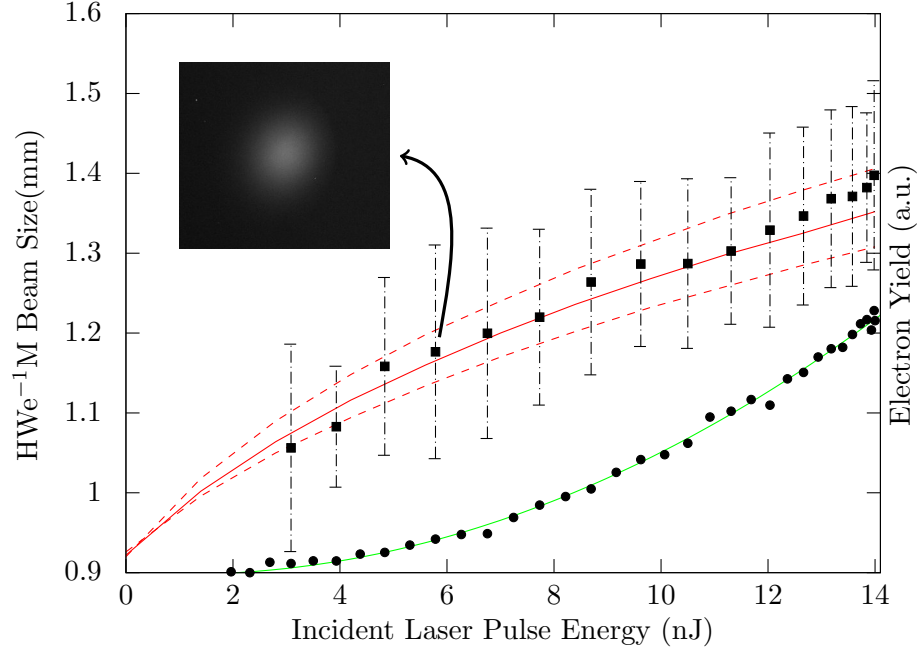


Figure 28: Measured Fourier plane electron beam size ($HWe^{-1}M$; squares) and electron yield (circles) as a function of the incident ~ 200 fs, 523nm laser pulse energy for the 300nm-thick gold photocathode. The electron yield is proportional to the square of laser pulse energy (solid green line) and the dependence of the beam size with the laser pulse energy fits that predicted by a zero free parameter electron heating model (solid red line; dashed lines represent $\pm 10\%$ error in the laser spot size). A representative raw Fourier plane beam image is also shown.

is less than the cooling time of the electron distribution so that the laser is only heating the electrons and not the lattice, which is true in this case.

Again using the experimental technique outlined in Section 7.1, we monitored the momentum distribution (Fourier plane spot size) for electrons emitted by 2PTE from gold using the ~ 200 fs green (523nm) p -polarized laser pulses. Due to the 60° angle of incidence, the circular laser beam is focused by the 30cm focal length lens to an elliptical $50 \times 100 \mu\text{m}$ (half-width $1/e$

maximum (HWe^{-1}M) of the field) spot size on the photocathode surface. The results, the measured Fourier plane beam size and electron yield, are displayed in Figure 28 as a function of the incident laser pulse energy, corrected to account for 10% optical loss (mainly from the uncoated vacuum system windows).

The quadratic dependence of the electron yield on pulse energy clearly indicates a two-photon emission process. This is expected since an excitation energy of two green photons ($\hbar\omega = 2.37\text{eV}$) will be required to overcome the reported $\Phi = 4.69\text{eV}$ effective work function of a thick gold film contaminated with adsorbed water (74) or ensure that at least the tail of the electron Fermi distribution has sufficient energy to overcome the $5.1(\pm 0.1)\text{eV}$ work function of a clean Au surface (35). Moreover, when $2\hbar\omega \approx \Phi$, the dependence of the yield on the square of the electron's excess energy above the work function (74) ensures that predominantly only the high energy (Boltzmann) tail of the Fermi distribution contributes to the emission. Consequently, the observed increase in Δp_T with incident pulse energy must be due to a heating effect; specifically, laser heating of the free electron Fermi gas as two-photon excitation is instantaneous and the $\sim 200\text{fs}$ green laser pulse duration excludes any coupling to the lattice which occurs on the time scale of a few picoseconds (28). The solid red line in Figure 28 is the predicted variation derived using a simple zero free parameter model of this effect. Using the known optical properties of gold (47), which give a reflectance $R_p = 0.53$ and an absorption depth of 20nm , and the temperature-dependent heat capacity of a free electron Fermi gas, the model evaluates the average temperature of the laser-heated electron gas that may be two-photon excited assuming that only electrons within a few nanometers of the surface can be emitted, as the mean free

path for electrons in Au is $\sim 4\text{nm}$ (92). This average electron temperature T_e is then used in the AG model simulation of the experiment (Figure 26) to determine the expected Fourier plane spot size on the YAG scintillator; that is, using an initial $\Delta p_T = \sqrt{mk_B T_e}$. The dashed red lines indicate the expected trends for a $\pm 10\%$ error in the laser spot size Δx_0 incident on the gold cathode surface. The close agreement between the data and the simulation strongly supports our interpretation of the emission mechanism.

7.4 Nanopatterned (Plasmonic) Photocathodes

In the search for alternative mechanisms to reduce the intrinsic divergence of the electron beam upon photoemission, a possible area of interest was Plasmon-Assisted Photoemission (PAPE). As the name suggests, a plasmon is the quasiparticle of plasma oscillation. When this occurs at the surface of a conducting material, the resultant quasiparticles are called “surface plasmon-polaritons.” Since these will be the only plasmons discussed in this thesis, the word “plasmon” will be used interchangeably for the name “surface plasmon-polariton.” Electrons in a conductor can couple with electromagnetic fields, in this case a laser field, and oscillate accordingly. This overall oscillation of electrons near the surface of the conductor creates strong oscillatory local surface electric field (30; 32). In PAPE, the goal is use this field to both enhance the emission and ‘control’ the divergence of photoemitted electrons through the combined action of photoemission barrier suppression and ponderomotive acceleration. On the other hand, these oscillating electrons are nothing but an oscillating current, and thus if a large plasmon response is established, resistive heating is a major concern even for the small resistivities typical of conductors.

This avenue of investigation was motivated by Zawadzka et al (110) who indicate that when driving a surface plasmon on gold they witnessed a reduction in the emission angle of photoemitted electrons. In their paper, the authors coat a thin gold film on a prism; the laser then “back illuminates” the gold through the prism, ejecting electrons on vacuum side of the foil. This arrangement is called the Kretschmann geometry. While this geometry is common, due to fears about the lack of heat conduction through the glass and the power needed to generate a sufficient electron beam current, we felt that for UEM applications we should explore the alternative “grating coupling” geometry (53; 54; 58). In this geometry, the plasmon is driven on a periodic surface rather than a flat surface attached to glass. Further, in this front-side illuminated geometry the back surface is now free to be attached to a heat sink.

7.4.1 The Grating Coupling Geometry

Every conducting material has an intrinsic plasma frequency given by

$$\omega_P = \sqrt{\frac{\rho_e e^2}{\varepsilon_0 m^*}}, \quad (7.4)$$

where ρ_e is the free-electron density and m^* is the electron effective mass in the material. And in the most simple (undamped) approximations, ε , the real part of the dielectric function of the material, may be written in the following form:

$$\varepsilon(\omega) = 1 - \frac{\omega_P^2}{\omega^2}. \quad (7.5)$$

At the interface of a vacuum and such a simple material, constraints on the material parameters which may allow surface plasmons, result in the condition that the dielectric constant at the oscillation frequency of the surface plasmon $\varepsilon(\omega_{SP}) = -1$ (30). Substituting this result into Equation 7.5 shows that this frequency of oscillation is simply related to intrinsic plasma frequency by

$$\omega_{SP} = \omega_P / \sqrt{2}. \quad (7.6)$$

Further, plasmons propagating along a vacuum interface carry momentum whose magnitude is given by

$$k_{SP}^2 = \frac{\omega^2}{c^2} \left(\frac{\varepsilon}{1 + \varepsilon} \right). \quad (7.7)$$

In the grating coupling scheme (shown in Figure 29) a laser of wavelength λ is incident on a material with a grating of period d , making an angle θ from the surface normal. A surface plasmon is driven when the sum of the component of the laser wave-vector parallel to the material surface (k_{Lx}) and a Fourier component ($k_G = 2\pi/d$) of the grating matches the wave-vector of the surface plasmon

$$k_{SP} = k_{Lx} + nk_G, \quad (7.8)$$

where n here is an integer. This expression reduces to

$$\sqrt{\frac{\varepsilon}{1 + \varepsilon}} = \sin \theta + \frac{n\lambda}{d}, \quad (7.9)$$

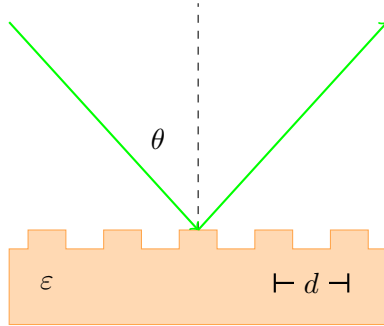


Figure 29: Schematic diagram of a grating coupling geometry for driving a surface plasmon

where λ is the incident laser wavelength. For a given grating period, Equation 7.9 determines the angle of incidence that the laser must make with the surface in order to drive the plasmon. Alternatively, it may be used to design the periodic surface structure, for example allowing for angles that the microscope column will accept, different driving orders (n), and even other Fourier components of the periodic surface structure.

7.4.2 Commercial Grating on Glass

For proof-of-concept purposes, the first experiment was performed on a commercially available gold foil on glass holographic grating (750 lines/mm). Like the Kretschmann geometry, a foil on glass grating is vulnerable to heating problems; a plasmon creates a large amount of heat but the glass is a poor heat conductor. The aforementioned laser (emitting ~ 200 fs pulses of green light at a peak pulse intensity of $30\text{MW}/\text{cm}^2$) was used to drive the plasmon.

The input laser angle was slowly changed until the plasmon oscillation is visible. At the instant that the plasmon started, a bright flash was visible on the scintillator screen and then

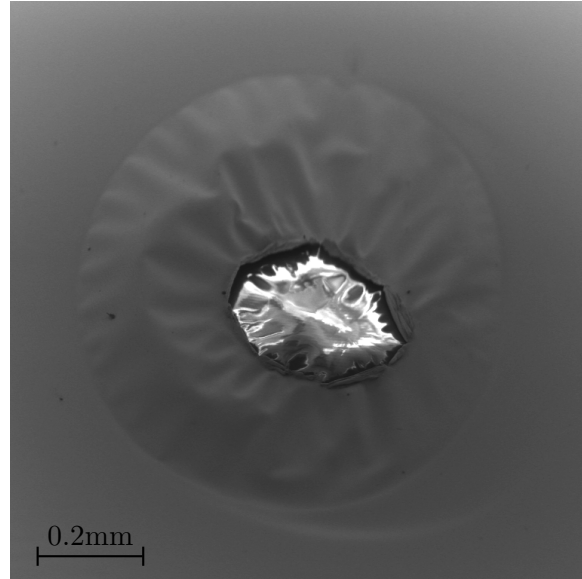


Figure 30: Damage to commercial gold-on-glass holographic grating

disappeared. After this, the grating showed visual signs of damage, both on the surface and in the reflected light pattern. Figure 30 shows the results of Scanning Electron Microscopy (SEM) on the grating. The damage pattern is round and of the size of the laser spot used to drive the plasmon. The extent of the damage indicates a large temperature increase, which given the other evidence of the test, can be assumed to be from the sudden appearance of a surface plasmon.

There are several conclusions that can be drawn from this experiment. Most importantly, it shows that a plasmon was driven successfully; given the angular dependence and large response, few other processes could have occurred. The heat generated by the plasmon oscillation destroyed the grating, therefore it validated the decision not to pursue a Kretschmann geometry

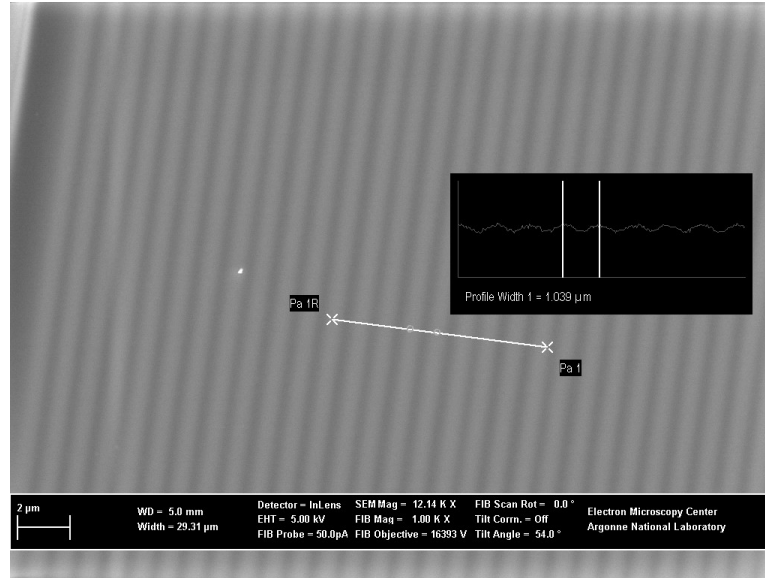


Figure 31: SEM image of sinusoidal grating on silicon. Pattern milled by focused ion beam milling at Argonne National Lab. Sample was later coated with 300 nm gold film.

over fears of heat damage at the high heating rates of the laser-plasmon interaction. Finally, it suggests that through the use of a thermally conductive and structurally sound photoemission material and mount for the plasmonic photocathode, PAPE might generate a large number of electrons (as evident by the bright flash).

7.4.3 Sinusoidal Grating

After the destruction of the gold foil on glass grating, new gratings were designed to have a higher substrate thermal conductivity. The second generation grating was constructed from a silicon substrate then coated with a gold film. The thermal conductivity of silicon is approximately 100 times that of glass.

Collaborators at Argonne National Laboratory's Electron Microscopy Center, Material Science Division employed a defocused Gallium focused ion beam (FIB) (Zeiss 1540XB) to mill an approximately sinusoidal shape into the surface of a silicon wafer. Several regions were created each $100 \times 100 \mu\text{m}$ in area, having a $\sim 1 \mu\text{m}$ period and $\sim 10\%$ modulation depth. By Equation 7.9, given a laser wavelength of 523nm ($\epsilon_{Au} \approx -3.95$ (47)), this choice of periodicity corresponds to an incidence angle of $\sim 39^\circ$, which is within the acceptance range of our experimental setup ($35\text{-}75^\circ$) (see Section 6.3). An SEM image of one such region is shown in Figure 31. A 300nm film of gold was deposited onto the silicon using the Varian e-beam deposition chamber at the UIC Nano Core Facility (NCF); a thin layer of chromium was deposited between the silicon and gold as a binding agent. As the gold film is many times thicker than the penetration depth of green light on gold and several times thicker than the penetration depth of the plasmon field, neither the laser radiation nor the plasmon field will couple with the silicon.

Figure 32 summarizes the photoemission results obtained from this gold-coated periodic photocathode under green (523nm) laser irradiation. Strong enhanced photoemission was observed for only a narrow $\pm 5\text{mrad}$ range of incidence angles θ around the expected plasmon resonance angle of 39° . Moreover, this enhanced laser-driven electron emission was only observed for p -polarized incident 523nm femtosecond laser radiation. These two properties are known characteristics of plasmon-assisted photoemission (53; 54; 58).

As seen in Figure 32, at low incident laser intensities, below a laser intensity of about $25\text{MW}/\text{cm}^2$, the emission from the nano-patterned photocathode at the plasmon resonance condition is very similar to that observed from a flat gold surface neighboring the FIB-milled

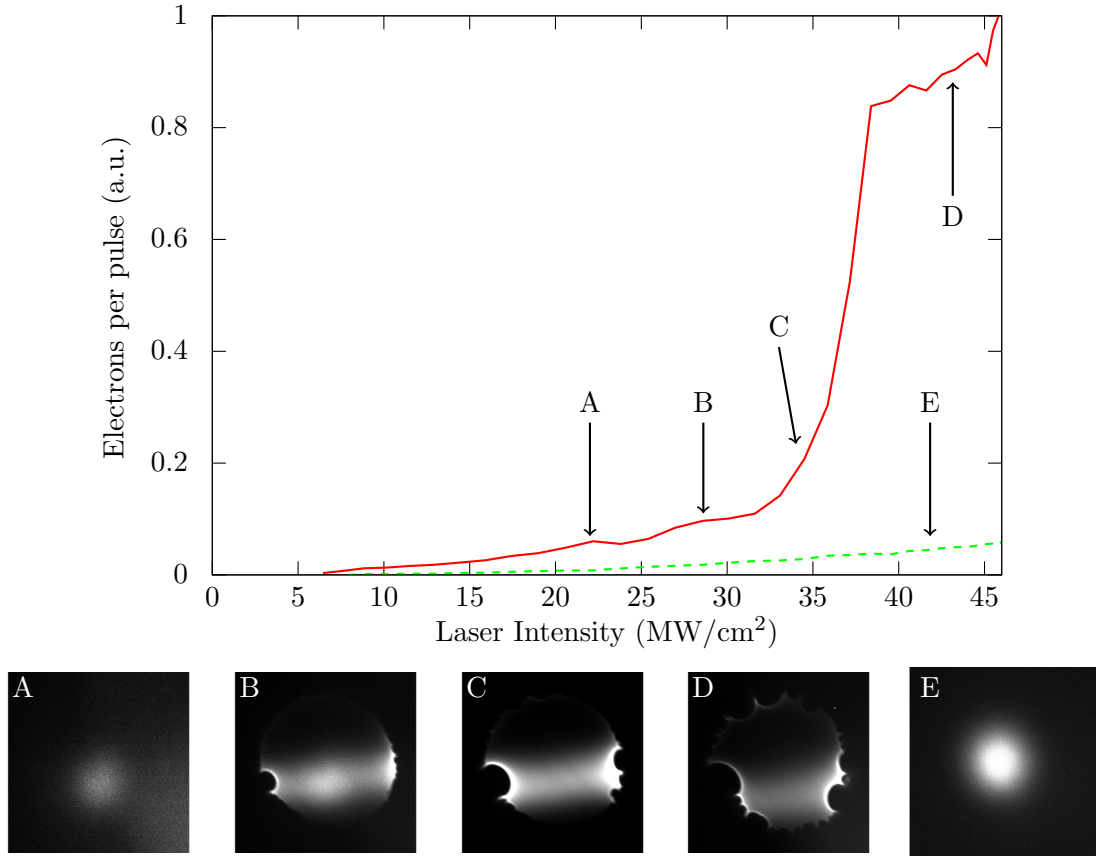


Figure 32: Photoemission characteristics of laser-driven plasmons on a one-dimensional periodic gold surface. Top: Electron emission strength as a function of incident 523nm femtosecond laser pulse intensity for coherently-driven plasmons (top curve) and comparative emission from a plane gold surface under the same irradiation conditions. Bottom: Two-dimensional electron momentum distributions for plasmon-assisted emission (A-D) and two-photon field emission from gold (E) at the laser intensities indicated on the top graph. The circular aperture visible in B-D is the 6mm-diameter bore of the magnetic focusing lens. The orientation of the grating lines of the periodic gold surface with respect to the emission in A-D is parallel to the broadening seen in B-D.

region. Specifically, the strength of both emissions have a quadratic dependence on the incident laser intensity. This is consistent with a two-photon field emission process — it requires the absorption of two 2.37eV (green) photons for an electron to acquire sufficient energy to allow any significant field emission as gold has a work function of $\sim 5\text{eV}$. Moreover, both emissions have similar momentum distributions (Figure 32 A and E), again indicating a similar emission process. The only difference is that the emission from the nano-patterned region is 3-4 times more efficient. This is readily explained by the fact that the periodic surface modulation results in a local enhancement of the $\sim 1\text{MV/m}$ DC gun field at the peaks of the modulation which, through the Schottky effect, then presents a reduced barrier for field emission.

I note here that for these measurements, the relative emission efficiencies are calculated from the integration of the luminosity detected on the YAG scintillator screen. The scintillator and CCD camera detection scheme was shown to be linear (i.e., integrated signal proportional to number of electrons per pulse) for at least 10^4 electrons per pulse, using the known linearity of single-photon photoemission from Ta irradiated by our 261nm ultraviolet laser source. As a result, the detection scheme will accurately determine any laser power law dependence to the electron emission from the photocathode.

Above an incident laser pulse intensity of $\sim 32\text{MW/cm}^2$, there is a rapid and dramatic increase in the emission efficiency for the nano-patterned photocathode. This can be explained by a suppression of the barrier to photoemission below the two-photon excitation energy, thus

allowing direct two-photon photoemission. The well-known Schottky Effect states that for an applied electric field E the work function will be suppressed by an amount

$$\Delta\Phi = -e\sqrt{\frac{eE}{4\pi\epsilon_0}}. \quad (7.10)$$

This suppression is likely caused by the laser-excited surface plasmon, since on the neighboring flat gold surface, where the suppression due to the laser (20MV/m) and the 20kV acceleration potential (0.8MV/m) is $\Delta\Phi \approx 0.18\text{eV}$, no similar increase in efficiency is observed. If this is indeed the case, and the surface plasmon field further suppresses the barrier to a total $\Delta\Phi \approx 0.35\text{eV}$ to allow direct two-photon photoemission, the field must be of the order of 60MV/m or three times that of the laser field. In Figure 32 B, at a laser intensity of $\sim 30\text{MW}/\text{cm}^2$, there is already a distinct broadening of the momentum distribution in the direction parallel to the wavevector k_G of the sinusoidal modulation on the photocathode (i.e., perpendicular to the FIB-milled grooves). This broadening becomes the dominant feature of the electron emission above $\sim 32\text{MW}/\text{cm}^2$; indeed, it becomes so severe that at laser intensities above $\sim 37\text{MW}/\text{cm}^2$ the 6mm-diameter bore of the magnetic lenses becomes a strong limiting aperture for the resulting beam — as is clearly seen in Figure 32 D and by the cut-off in the detected electron signal (YAG fluorescence).

7.4.4 Sinusoidal Grating, Rotated

In principle, this unexpected increase in transverse momentum (Figure 32 B and C) could be caused by any of three effects. The first, and most easily ruled out, is that the electric

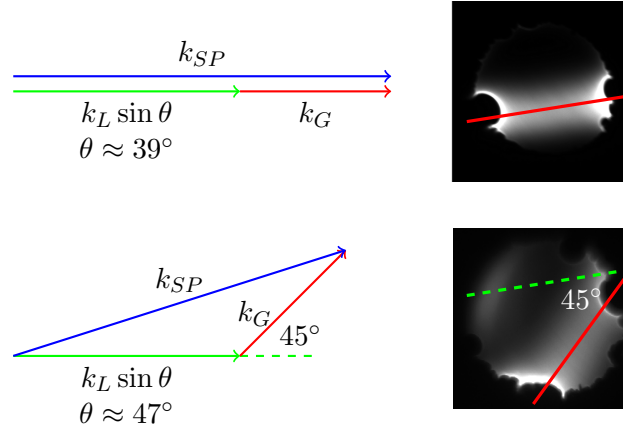


Figure 33: Comparison of the collinear (above) and rotated (below) plasmonic excitation geometries. This rotation separates the directionality of effects caused by the laser, plasmon field and grating. Each vector diagrams (left) is shown next to a representative observed momentum distribution image (right). The increased divergence is shown to be rotated by the same 45° as the grating (the original collinear line is shown dashed); evidence that the grating is the cause of the deleterious effect.

field of the laser itself could affect the electrons, causing the divergence. The possibility is easily dismissed as the effect is not observed when off the grating. The second possible cause is the divergence of the plasmon's own electric field ($\partial E_{plasmon}/\partial x$). This field is parallel to the surface plasmon vector k_{SP} (assumed here to be in the x direction). The third possible cause is local field enhancement of the accelerating electric field due to the peaks in the sinusoidal shape of the surface, commonly known as the “lightning rod” effect. For the employed one dimensional grating, this effect is necessarily parallel to the grating vector k_G .

Given the geometry of the previous measurement, notably the collinear arrangement of plasmon vector and the grating vector, the true cause is difficult to determine. However, if

instead the grating is rotated — and the laser incidence angle is corrected to account for the longer effective periodicity of the surface — the directionality of these effects may be separated. The left side of Figure 33 shows the comparison of the grating vector geometries for the original scheme (top) and one in which the grating is rotated by 45° (bottom). For this rotation, the laser angle must be increased from 39° to 47° .

The experimental results are shown to the right in Figure 33. As the divergence is clearly shown to be rotated by 45° with respect to the collinear case, this experiment demonstrates that the cause of the divergence increase is due to the local field enhancements near the peaks of the grating. For a mathematical treatment of the transverse electric field of such patterned surfaces, the reader is referred to Ref. (106). Our results are commensurate with the results shown by Zawadzka et al (110), who showed a reduced divergence in the Kretschmann geometry. As that geometry does not employ a patterned surface, it would not be subject to such local field enhancements of the accelerating electric field.

7.4.5 Trenched Grating

In an attempt to mitigate the effect of the surface peaks on the accelerating field, a new pattern was commissioned and prepared in a similar manner to the original. This new photocathode featured long trenches of an approximately square profile, arranged periodically across the surface; the trench spacing was five times the trench width in an attempt to present a “flatter” surface, which would should be less disruptive to the accelerating electric field. Although this periodicity should have been sufficient to facilitate the generation of the plasmon, the pho-

tocathode performed markedly worse than its sinusoidal predecessor. Indeed, no evidence of successful plasmon oscillation was demonstrated after repeated attempts.

Though the cause of the failure may never be known for certain, several causes are suspected. Now that the surface is not purely sinusoidal, the surface has multiple Fourier components. This may mean that the laser may not couple as efficiently to the plasmon, requiring significantly increased laser power for PAPE. Additionally, the non-smooth surface may cause increased difficulty for propagating the plasmon over large distances. Finally, upon further investigation of the surface by SEM, evidence was observed of incomplete filling of the gold coating into the trenches, which may have interrupted creation or propagation of the plasmon.

7.4.6 Discussion

Although plasmonic photocathodes are still an interesting field of research in photocathode physics, we have concluded that they are not a promising candidate for an electron source for UEM at this time. They have been difficult to manufacture and thus would likely be expensive. They are very intolerant to misalignment and would therefore be problematic for users. Finally, they cannot be shown to produce the performance (that is, a reduced transverse emittance) needed to justify the previous concerns.

Other nano-engineered surfaces are still being considered for future work. Various other more exotic nano-structures are under examination for PAPE (58; 82). Bi-metallic layers are known to enhance PAPE, which may allow for reduced incident laser power for driving the plasmon (54). Photoemission from nano-arrays of quantum-wells also offers the tantalizing hope of reduced rms transverse momentum of the generated electrons.

7.5 Excited State Thermionic Emission

Recent experiments in our group have come to change our understanding of several photoemission processes, once thought to be well understood (18). Indeed, while this knowledge has been commonplace in other fields, such as angle-resolved photoemission spectroscopy (ARPES) (42), to our knowledge the effect has not been considered for electron beam generation. In this section, we show that, at least for thermionic emission, the effective mass m^* of the electronic state from which the electron was emitted affects the rms transverse momentum; that is, the expression for Δp_T developed in Refs. (34) and (45) for thermionic electron emission should be rewritten to read $\sqrt{m^* k_B T_e}$, where T_e is the temperature of the emitting electron distribution and k_B is Boltzmann's constant. Direct observation of the transverse momentum distribution for excited-state thermionic emission (ESTE) from GaSb and InSb, two similar III-V zincblende semiconductors, demonstrates the m^* dependence. Simulations of the experiment using our extended analytical Gaussian (AG) model of electron pulse propagation (see Section 3.3) are in close agreement with the data.

Figure 34 depicts the results obtained for GaSb and InSb photocathode materials under pulsed UV (261nm) laser irradiation using the same experimental technique employed for PAPE, 2PTE, and single-photon PE studies. Both samples are cut from [100]-oriented polished wafers; the GaSb is undoped and the InSb is moderately p -type. Prior studies (40) indicate that single-photon photoemission should not be possible for either semiconductor — the effective photoemission work functions (about 4.8eV for undoped GaSb and 4.89eV for p -type InSb (Fermi level pinned at valence band maximum)) being greater than the 4.75eV photon

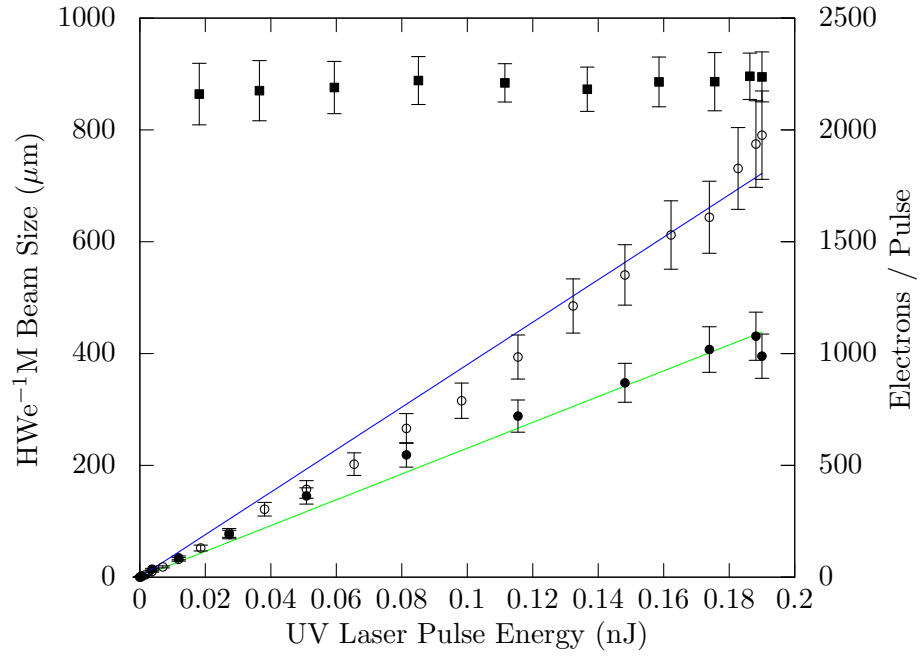


Figure 34: Number of electrons emitted per pulse as a function of the incident 261nm, UV laser pulse energy for GaSb (filled circles) and InSb (open circles): Linear efficiency dependences are shown by the solid lines. The laser pulse energy invariance of the $HWe^{-1}M$ Fourier plane electron beam size (filled squares) for GaSb and a representative raw Fourier plane beam image is also shown.

energy even when the 34meV Schottky barrier suppression due to the applied 8kV/cm DC field is included (34; 18). Nonetheless, for both zincblende semiconductors, significant laser-driven emission (more than expected for a single-photon field emission process) is observed with a yield nearly linearly proportional to the ~ 4 ps UV laser pulse energy. Note that due to the surprisingly large yield, we repeated the measurements, this time replacing the the scintillator screen with a Faraday cup and repeating the laser energy sequence. In this way, the yields for these photocathodes were measured directly and absolutely, unlike the results presented in the preceding sections, for which relative measurements were sufficient.

The known optical properties of the two semiconductors (14) indicate a strong absorption at 261nm, with an optical absorption depth of only 7-8nm, which, based on the band structures of GaSb (26) and InSb (27), is primarily due to promotion of electrons near the Γ point from the valence band (heavy-hole, light-hole, and split-off bands) directly into the upper Γ_8 conduction band located at 3.77eV and 3.59eV above the valence band maximum in GaSb and InSb, respectively. Assuming parabolic bands and an estimated effective mass m^* of about $0.3m$ ($0.5m$) for the Γ_8 conduction band in GaSb (InSb), we determine that these electrons are excited with an average excess energy (above the Γ_8 conduction band minimum) of ~ 0.35 eV (~ 0.41 eV); that is, an initial electron temperature T_e of $\sim 4,200$ K ($\sim 4,900$ K). For the ~ 0.1 nJ incident UV pulse energies, $\sim 40\mu\text{m}$ laser spot size, and p -polarized reflectance of $\sim 40\%$ for both semiconductors at our 60° incidence angle, the photo-injected electron density is $\sim 10^{18}\text{cm}^{-3}$. At these carrier densities, which are non-degenerate for the upper Γ_8 conduction bands, we expect rapid thermalization (83) and, consequently, an electron distribution with a well-populated Boltzmann

tail extending above the vacuum level located at an effective work function Φ of 0.99eV (1.18eV) above the Γ_8 conduction band minimum in GaSb (InSb); thus allowing for thermionic emission from this excited state as initially $\exp[\Phi/(k_B T_e)] \approx 0.06$ in both semiconductors.

Carrier cooling, primarily by longitudinal optical (LO) phonon emission, and decay out of the upper conduction band to lower states will rapidly deplete the Boltzmann tail above the effective $\sim 1\text{eV}$ work function, thereby curtailing the observed ESTE. By comparison with the Γ_6 conduction band Fröhlich coupling constant in GaAs, where the characteristic LO phonon emission time is 165fs for a hot electron in the Γ_6 conduction band (48), we estimate that hot electrons in the upper Γ_8 conduction band of both GaSb and InSb emit a LO phonon every $\sim 200\text{fs}$ with an energy of 29 and 24meV, respectively. This means that even without population decay mechanisms the temperature of the excited electron distribution T_e drops at a rate of $\sim 1,600\text{K/ps}$ in both semiconductors. We note that the close proximity of the lower and unconfined (in momentum space) Γ_7 upper conduction band to the Γ_8 band will likely result in a fast population decay, so that the observed ESTE process should have an intrinsic latency of much less than the $\sim 4\text{ps}$ UV laser pulse duration.

Figure 34 also shows that the measured Fourier plane electron beam spot size for GaSb is independent of the UV laser pulse energy, as would be expected for the proposed emission process. More significantly, using $\Delta p_T = \sqrt{mk_B T_e}$ (i.e., assuming the emitted electrons have a mass m in the semiconductor), simulation of the experiment with the extended AG model (15) indicates that the observed GaSb Fourier plane spot size of $0.90(\pm 0.06)\text{mm}$ (HWe^{-1}M) would be due to an electron temperature $T_e \approx 360\text{K}$ which is associated with negligible thermionic

emission ($\exp[-\Phi/(k_B T_e)] \sim 10^{-15}$). On the other hand, employing a mass of $0.3m$ for the electrons in GaSb allows an average electron temperature (over the ~ 4 ps laser pulse duration) of about 1,200K to be extracted using the AG model simulation — a value much more consistent with the proposed ESTE mechanism and the expected cooling rate by LO phonon emission. In fact, at the maximum ~ 0.2 nJ incident UV laser pulse energy up to 10^8 electrons/pulse could be excited into the upper Γ_8 conduction band, of which one in $\exp[\Phi/(k_B T_e)] \approx 20,000$ are above the effective 0.99eV work function, thus agreeing with the observed yield of $\sim 10^3$ electrons/pulse (Figure 34). We also note that the normalized transverse rms emittance ε_T of this UV laser-driven ultrafast GaSb electron source is more than a factor of two less than that expected from a standard Cu photocathode ($\Phi = 4.31$ eV and assuming $\Delta p_T = \sqrt{m(\hbar\omega - \Phi)}/3$, where $\hbar\omega$ is the incident photon energy (34; 45)) irradiated at the same 261nm wavelength.

Very similar results are observed with the p -type InSb photocathode except that the Fourier plane spot size is 30-40% larger and the electron yield is a factor of 1.7 higher. The increased rms transverse momentum for the same ESTE process is consistent with the larger $\sim 0.5m$ effective mass of the upper Γ_8 conduction band in InSb, the expected higher initial temperature of the electron distribution, and the marginally slower cooling process associated with the lower 24meV LO phonon energy. The resultant higher average electron temperature T_e also contributes to the increased electron yield that is likely further enhanced by a larger absorption into the upper Γ_8 conduction band (due to its larger effective mass) and a 4% lower p -polarized reflectance for the 60° incident UV laser radiation (14).

The dependence of Δp_T on m^* is readily explained through a consideration of energy and momentum conservation in transmission across a boundary with a potential step associated with the effective photoelectric work function Φ . Inside the material, an electron with an energy E above the Fermi energy which is greater than Φ has a maximum momentum of $\sqrt{2m^*(E - \Phi)}$ parallel to the boundary if it is to be emitted. As this momentum component is conserved in emission from the material surface into the vacuum, the rms transverse momentum Δp_T of the electron source clearly must scale with $\sqrt{m^*}$ as observed in the experiment. This is, of course, the *sine qua non* of angle-resolved photoemission studies (42) where determination of the electron emission angle and energy allows the effective mass parallel to the sample surface to be determined. We note that the electron effective mass also causes the narrow emission cone reported for *p*-type GaAs(100) negative electron affinity photocathodes (61), where surface cesiation lowers the vacuum level below the Γ_6 -valley minimum ($m^* = 0.067m$) to allow for direct emission of electrons excited into the conduction band.

7.6 Future Prospects

The philosophical argument presented in Section 7.5 for using the effective mass m^* in the expressions for the transverse momentum variance Δp_T simply follows from conservation of energy and momentum at the barrier and actually does not depend on the “excited state” nature nor the thermionic emission process. For the example of two-photon assisted thermionic emission (2PTE) from gold presented in Section 7.3, the close agreement between the data and the simulation is supported by the fact that the effective mass of a free electron in Au is equal to its rest mass m (47) — the value employed in that analysis.

For direct single-photon photoemission, we would therefore also expect to require that the expression describing the rms transverse momentum (Equation 3.3, Refs. (34) and (45)) to be written as $\Delta p_T = \sqrt{m^*(\hbar\omega - \Phi)/3}$. Efforts are currently underway to determine if this is indeed the case using a variety of metal photocathodes and the ~ 4 ps, 261nm laser radiation source. In an upcoming publication, we will show that the dependence of Δp_T on the electron effective mass may be extended to simple planar metal photocathodes — thus potentially allowing for the future development or discovery of a robust, high brightness photocathode material. For a selection of single-crystal and polycrystalline photocathodes, we will show that the simulation, incorporating m^* , is in good agreement with our direct measurements of Δp_T . We will also discuss the effect of laser-induced heating on Δp_T of the electron distribution in the photocathode during photoemission, which may limit the attainable pulsed electron source brightness at the desired high peak pulse current densities.

CHAPTER 8

CONCLUSIONS

Ultrafast Electron Microscopy is an exciting new field of instrumentation research which promises to open our eyes to the dynamics occurring in nanoscale processes. Through my contributions to this field, I have worked to advance this new technology. These include developing and implementing a model for simulating the dynamics of ultrafast electron pulses in electron microscope systems, deriving necessary design criteria for constructing such a system, and laying the theoretical and experimental groundwork towards selecting a useful photocathode for electron pulse generation. These advances have guided the design and construction of the prototype ultrafast electron microscope system being built at UIC.

8.1 Modeling

In this thesis, I have presented the extended Analytic Gaussian (AG) model, an efficient mean-field numerical model based on the work of Michalik and Sipe (70), but extended so as to be useful in modeling the dynamics of ultrafast electron pulses in microscope columns. For pulses containing N carriers of charge e and mass m , the model is simply these four equations,

$$\frac{d\sigma_\alpha}{dt} = \frac{2\gamma_\alpha}{m} \tag{8.1a}$$

$$\frac{d\gamma_\alpha}{dt} = \frac{\Gamma_\alpha^2 + \gamma_\alpha^2}{\sigma_\alpha m} + \frac{Ne^2}{4\pi\epsilon_0} \frac{1}{6\sqrt{\sigma_\alpha\pi}} L_\alpha(\xi) + \sigma_\alpha \sum_f M_\alpha^{\{f\}}. \tag{8.1b}$$

where the subscript α denotes the directionality of the dynamics, either $_T$ for the transverse or $_z$ for the longitudinal. At any time t , the σ_α quantities characterize the spatial variance of the pulse and γ_α represent the momentum chirps across the pulse. A third parameter, the local momentum variance η_α , is also encoded in these equations. By Liouville's theorem, which the AG model explicitly satisfies, we know that the product of the spatial variance σ_α and the local momentum variance η_α is constant throughout propagation (for perfect lensing and without clipping the pulse), so we define the constant,

$$\Gamma_\alpha^2 \equiv \sigma_\alpha \eta_\alpha, \quad (8.2)$$

which in the transverse direction is explicitly related to the the normalized transverse emittance (for cylindrically symmetric pulses),

$$\varepsilon_T = \frac{1}{mc} \sqrt{\langle x^2 \rangle \langle p_T^2 \rangle} = \frac{1}{mc} \sqrt{\sigma_T \eta_T}. \quad (8.3)$$

By evaluating this constant once, presumably from initial conditions, and later applying Equation 8.2, one may extract these η_α parameters, having only needed to compute the other four. The parameter ξ characterizes the ellipticity of the cylindrically symmetric pulse,

$$\xi \equiv \sqrt{\frac{\sigma_z}{\sigma_T}}, \quad (8.4)$$

and the family of L functions (defined in Equation 2.28) are smooth and well behaved functions for all physically meaningful ξ . Finally the $M_{\alpha}^{\{f\}}$ quantities define the α direction influence of the f^{th} external force.

In UEM, the initial pulse conditions are of notable importance for the performance of the instrument, therefore having a realistic description of these initial conditions is essential for accurately modeling the pulse dynamics. To this end, I have presented a simplistic but useful set of initial conditions for the extended AG model. This analysis assumes a photocathode with a work function Φ , the energy an electron must absorb before it is freed to leave the material, placed in a DC gun which accelerates the pulse by an electric field E_{DC} . It also assumes a laser pulse whose intensity I is of the form,

$$I(x, y, t) = I_0 \exp \left(-\frac{(x^2 + y^2)}{w^2} - \frac{t^2}{\tau^2} \right), \quad (8.5)$$

where w and τ are the HW1/eM laser pulse width and duration respectively, and the photon energy $\hbar\omega$ is greater than Φ , thus permitting single-photon photoemission. Ejected electrons will then carry an excess photoemission energy $\Delta E = \hbar\omega - \Phi$, so that the maximum velocity

that an ejected electron may have is $v_{max} = \sqrt{2\Delta E/m}$. Given these generic assumptions, the resulting initial conditions are simply,

$$\sigma_T(0) \approx \frac{w^2}{2} \quad (8.6a)$$

$$\sigma_z(0) \approx \frac{(v_{max}\tau)^2}{2} + \left(\frac{eE_{DC}\tau^2}{4m} \right)^2 \quad (8.6b)$$

$$\gamma_T(0) \approx 0 \quad (8.6c)$$

$$\gamma_z(0) \approx \sqrt{\sigma_z(0)} \left(mv_{max} + \frac{eE_{DC}\tau}{\sqrt{2}} \right) \quad (8.6d)$$

$$\eta_T(0) \approx \frac{m}{3}(\hbar\omega - \Phi) \quad (8.6e)$$

$$\eta_z(0) \approx \frac{\eta_T(0)}{4}. \quad (8.6f)$$

In Section 3.1.2 I have also presented a binning model which is being investigated as a possible improvement to this simplistic set of initial conditions.

Most UEM systems will employ magnetic lenses and DC accelerators; there is also increasing interest in using RF cavities for pulse compression. The extended AG model can simulate the influence of the external forces imparted by these column elements on the electron pulse via the M parameters in Equation 8.1b, which are in terms of the position of the center of the pulse z' (in the lab frame) and its velocity v_0 . Each magnetic lens, positioned at z'_{mag} and of length L_{mag} , can be represented simply as

$$M_T^{mag} = M_T^{mag}(I) \exp \left[- \left(\frac{z' - z'_{mag}}{L_{mag}/2} \right)^2 \right], \quad (8.7)$$

where $M_T^{mag}(I)$ is a lens-specific characterization of the magnetic field strength (versus current I). A single TM₀₁₀-mode cylindrical RF cavity, positioned at z'_{RF} , having length L_{RF} , and oscillating at frequency Ω with field strength E_0 and phase shift ϕ , may be expressed as

$$M_z^{RF} = \left[\frac{e\Omega E_0}{v_0} \cos\left(\frac{\Omega z'}{v_0} + \phi\right) \right] \exp\left[-\left(\frac{z' - z'_{RF}}{L_{RF}/2}\right)^2\right] \quad (8.8)$$

$$M_T^{RF} = eE_0 \left[\frac{v_0\Omega}{c^2} \cos\left(\frac{\Omega z'}{v_0} + \phi\right) + \frac{2n}{L_{RF}} \left(\frac{z' - z'_{RF}}{L_{RF}/2}\right)^{2n-1} \right. \\ \left. \times \sin\left(\frac{\Omega z'}{v_0} + \phi\right) \right] \exp\left[-\left(\frac{z' - z'_{RF}}{L_{RF}/2}\right)^2\right]. \quad (8.9)$$

Additionally, since an RF cavity can act as a pulse accelerator an additional force term

$$F_z^{RF} = eE_0 \sin\left(\frac{\Omega z'}{v_0} + \phi\right) \exp\left[-\left(\frac{z' - z'_{RF}}{L_{RF}/2}\right)^2\right], \quad (8.10)$$

should be added to the equation of motion governing the propagation of the pulse down the column. Finally, if an acceleration region with cathode at $z' = 0$, anode at z'_A , and acceleration potential V , has an on-axis force of the form

$$F_z(0, z') = \frac{eV}{2z'_A} \left(1 - \tanh\left(\frac{z' - z'_A}{z'_A/s}\right) \right), \quad (8.11)$$

where s is a parameter that quantifies the sharpness of the field drop at the anode, then accelerator's influence on the pulse dynamics are given by

$$M_T = -\frac{eVs}{4z_A'^2} \operatorname{sech}^2 \left(\frac{z' - z_A'}{z_A'/s} \right) \quad (8.12)$$

$$M_z = \frac{eVs}{2z_A'^2} \operatorname{sech}^2 \left(\frac{z' - z_A'}{z_A'/s} \right). \quad (8.13)$$

Since the extension to the AG model is valid only within the limits of the analytical method itself, in particular, its mean internal space-charge field and self-similar Gaussian approximations (70), the extension reflects a first-order (i.e., linear force) analysis of the effects of electron optics upon electron pulse propagation. Nonetheless, for free-space propagation, the AG model of charge bunch dynamics has already been shown to be very consistent with full Monte Carlo (i.e., particle tracking) simulations for a wide variety of electron pulse shapes (70; 72), including the uniform ellipsoid (63). This successful benchmarking is due primarily to the versatility of the AG model which results from its use of transverse and longitudinal pulse position and momentum variances. Consequently, the AG approach is applicable to both the single electron per pulse limit (62), where momentum variances determine the pulse evolution and the model is exact (obeying Gaussian optics), and the high charge density limit in which space-charge effects dominate (63; 96; 25). It is this versatility combined with its computational efficiency that makes the presented extended AG model particularly suitable for rapid initial assessments of pulsed electron microscope column designs and electron pulse delivery systems in UED experiments.

I have written an implementation of this model for the Perl programming language and released it to the Comprehensive Perl Archive Network (CPAN) under the name `Physics::UEMColumn` for use by the UEM community (<https://metacpan.org/module/Physics::UEMColumn>). It is released as free software under the terms of the Artistic License (a derivative of the GNU General Public License). This module is fully object-oriented, which makes it remarkably easy for an end-user to read, write, and change simulation scripts which use it. Under the hood, though, it uses a custom set of C level bindings to the GNU Scientific Library (GSL, <http://www.gnu.org/software/gsl/>), so that the numerical equation solving is fast and accurate. This speed, combined with the dynamic flexibility offered by object-oriented Perl, allows one to easily write optimization scripts and generate figures which might have been nearly impossible previously; several of these have been shown in this thesis.

8.2 UEM Design

This thesis expounds on several factors that are key concepts in designing a UEM. I have used the above model to show that for a given electron pulse, whether oblate (disk-like) or prolate (cigar-like), its initial expansion will be primarily in the same direction as its shorter dimension, i.e., an electron pulse “wants” to be spherical. The model predicts that the use of shorter focal-length magnetic lenses will result in higher fidelity focusing; such lenses limit the impulse delivered to the pulse by reducing the time of flight during which the pulse experiences the higher charge densities inherent while focusing. Additionally, we have seen that oblate pulses are preferred to prolate pulses in terms of focus fidelity. The model also demonstrates that when properly designed and driven, RF cavities can effectively recompress electron pulses which

have expanded longitudinally. Interestingly, the model suggests that the additional bandwidth generated by space-charge repulsion (especially in higher charge-density pulses) can allow for additional pulse compression, to durations shorter than expected, even at one-to-one image to object distances.

The Rose criterion (88) states that in order to have sufficient gray-scaling in a single-shot DTEM employing a 1k X 1k CCD camera for imaging, the pulse must contain at least 10^8 electrons. Additionally, the Child-Langmuir Law (29; 57) governs the upper-limit of charge extraction in an electron gun. Pulses which are short enough to be fully contained inside the acceleration region are subject to a modified form of Child-Langmuir Law (101), which limits its the number of electrons N_{crit} that may be generated by a laser of HW1/eM width w before the pulse is subject to deleterious distortions,

$$N_{crit} = \frac{\pi\epsilon_0 w^2 V_{DC}}{ed}, \quad (8.14)$$

where V_{DC} and d are the accelerator voltage and length respectively. Due to this distinction, it is proposed that the term “ultrafast” should therefore be reserved for pulses of this type. In order to satisfy the both the Rose criterion and this ultrafast Child-Langmuir restriction, we expect that UEM instruments will need to employ a relatively large-area emission source, typically of the order of $100\mu\text{m}$ HW1/eM width or greater. This has necessitated building a custom acceleration region based on the design of Togawa *et al.* (100) which boasts a moderately uniform

acceleration field near the axis of the accelerator, as well as other large-aperture electron-optical elements for our prototype UEM column.

We have also designed and built a custom laser source capable of generating these electron pulses. The primary laser radiation source for the studies is a home-built, diode-pumped and thermal-lens-shaped, femtosecond Yb:KGW oscillator (16) delivering 250fs duration pulses at 1047nm and a 63MHz repetition rate. This 2W average power laser is frequency doubled in a 3mm lithium triborate (LBO) crystal with 50% efficiency to yield ~ 200 fs green pulses at 523nm (photon energy, $\hbar\omega = 2.37\text{eV}$). Further doubling with a cylindrical focusing geometry in a 7mm β -barium borate (BBO) crystal yields 261nm ($\hbar\omega = 4.75\text{eV}$) UV pulses with a duration of ~ 4 ps (due to the 600fs/mm group velocity mismatch between the green and generated UV). An ancillary benefit of using an in-house built laser source is that the cavity length may be easily changed; for soliton mode-locked lasers, this length is directly related to the repetition rate. By tuning the length, one may frequency match a high harmonic of the repetition rate and the natural oscillation of an RF cavity. As a result, the laser and the RF cavity may be synchronized in an essentially passive manner, obviating the need for expensive electronic devices which would be add deleterious electronic phase noise (jitter) to the system.

8.3 Photocathode Engineering

A common figure of merit for electron beams is its normalized transverse emittance (45), ε_T , which for the usual case of axially symmetric electron pulses has the form,

$$\varepsilon_T = \frac{1}{mc} \Delta x \Delta p_T = \frac{\Gamma_T}{mc}, \quad (8.15)$$

where Δx and Δp_T are the transverse spatial uncertainty and transverse momentum uncertainty, respectively. This quantity is conserved under propagation through free space and perfect electron-optical, though it may increase for imperfect ones (78). The normalized transverse emittance limits the resolving capability of the beam, so this quantity can be thought of as a measure of the beam quality, where a smaller value is preferred (17). Since we have already established that a large area emission source must be used in UEM, the only avenue to reduce ε_T is to reduce the transverse momentum uncertainty, which is dependent on the photocathode and photoemission process employed.

The desire to reduce the transverse momentum uncertainty Δp_T — in an effort to reduce the rms transverse emittance ε_T and thereby improve the resolving power of the electron pulse (17) — has driven us to explore many photocathodes and even several different photoemission processes. I have demonstrated that single photon photoemission and two-photon thermionic photoemission were not likely candidates to reduce the Δp_T as those processes were tied to intrinsic properties of the material which couldn't provide high-yield and low emittance simultaneously. Recently, however, we have discovered that for those processes, the effective electron mass m^* should have been considered, and therefore we are currently revisiting many of the materials that fall into these categories, a publication on this topic is in preparation.

I have also presented our efforts to employ periodic nanostructured photocathode surfaces, designed to allow the incident laser to drive a surface plasmon, in hopes that a surface plasmon field might reduce the transverse emittance (110; 53; 54; 58). Though we had success in driving the plasmon, we were unable to demonstrate reduction in Δp_T . We believe the problems were

due to disturbances in the acceleration field near these nanostructures, though efforts to mitigate those disturbances have yet been unsuccessful.

The most promising results have come from excited-state thermionic emission (ESTE) sources, GaSb and InSb. In this process the laser promotes carriers from the valence band to an upper conduction band close to the vacuum level, reducing the effective work function. The electron temperature, elevated by the laser-driven photoemission process to $\sim 10^3\text{K}$, causes the tail of the Fermi distribution to exceed the effective work function and thus emission occurs. Importantly, the results we observed were inconsistent with predictions until we considered the effective mass of these upper conduction bands. Not only did this allow our prediction to match the experimental results, it opened our eyes to the possibilities of low effective mass materials, even for photoemission processes other than ESTE. As I have mentioned earlier, this work is ongoing and is a very exciting avenue for future research.

APPENDIX

EXAMPLE SIMULATION SCRIPT

In this appendix, I want to introduce the Perl implementation of the extended AG model, called `Physics::UEMColumn`. This distribution has been released as open source software under the terms of the Artistic License (a derivative of the GNU General Public License), which allows for free use of the software. The current state of development is available at <https://github.com/jberger/Physics-UEMColumn>, while official releases are available via the Comprehensive Perl Archive Network (CPAN) and its many tracker websites, see for example <https://metacpan.org/module/Physics::UEMColumn>.

The module is implemented as fully object-oriented Perl. For ordinary differential equation solving, it employs a custom designed, closure-based interface to the GNU Scientific Library (GSL, <http://www.gnu.org/software/gsl/>), which uses a Runge-Kutta Prince-Dormand (8,9) step function (RK8PD), so that the numerical equation solving is both fast and accurate (see <https://metacpan.org/module/PerlGSL::DiffEq>). I have also developed a system by which the object framework can use input units of the user's choosing for convenience (see <https://metacpan.org/module/MooseX::Types::NumUnit>).

To write a simulation script, the end-user need only define physical parameters of the system as instances of certain classes, and appropriately add them to the overall simulation object of class `Physics::UEMColumn`. In the following script, which produces Figure 9 (the compound element system), this occurs in lines 11-63. The `propagate` method call (line 65)

APPENDIX (Continued)

then performs all of the simulations given the current state of the overall `Physics::UEMColumn` object, which returns a two-dimensional Perl array of results. The columns are, in this order: elapsed time t , pulse center position z' , velocity of the pulse center v_0 , σ_T , σ_z , γ_T , γ_z , η_T , η_z . In line 65 I immediately load the returned data into the Perl numerical library PDL (see <http://pdl.perl.org>), which is rather like MatLab. Using this PDL object, I extract the pulse position (column 1, zero indexed), and the spatial variances (columns 3 and 4). I then plot the the data in terms of the normalized width and length of the pulse.

```

1  #!/usr/bin/env perl
2
3  use strict;
4  use warnings;
5
6  use Physics::UEMColumn alias => ':standard';
7
8  use PDL;
9  use PDL::Graphics::Prima::Simple [700,500];
10
11 my $laser = Laser->new(
12     width    => '100 um',
13     duration => '0.1 ps',
14     energy   => '4.75 eV',
15 );
16
17 my $acc = DCAccelerator->new(
18     length => '20 mm',
19     voltage => '20 kilovolts',
20 );
21
22 my $column = Column->new(
23     length    => '350 mm',
24     laser     => $laser,
25     accelerator => $acc,
26     photocathode => Photocathode->new( work_function => '4.25 eV' ), # Ta
27 );
28
29 my $sim = Physics::UEMColumn->new(
30     column => $column,
31     number => 1e6,
32     steps  => 200,
33     solver_opts => {
34         h_max => 5e-13,
35         h_init => 5e-14,
36     },
37 );
38

```

APPENDIX (Continued)

```

39 my $z_rf      = 20; #cm
40 my $l_mag_lens = '1 in';
41 my $cooke_sep  = 5; #cm
42 my $str_mag    = 43e-13;
43
44 my $lens1 = MagneticLens->new(
45   location => ($z_rf - $cooke_sep) . 'cm',
46   length   => $l_mag_lens,
47   strength => $str_mag,
48 );
49 my $lens2 = MagneticLens->new(
50   location => ($z_rf + $cooke_sep) . 'cm',
51   length   => $l_mag_lens,
52   strength => $str_mag,
53 );
54 $sim->add_element($lens1);
55 $sim->add_element($lens2);
56
57 my $rf_cav = RfCavity->new(
58   location => $z_rf . 'cm',
59   length   => '2 cm',
60   strength => '335 kilovolts / m',
61   frequency => '3 gigahertz',
62 );
63 $sim->add_element($rf_cav);
64
65 my $result = pdl( $sim->propagate );
66
67 my $z = $result->slice('(1),');
68 my $st = $result->slice('(3),');
69 my $sz = $result->slice('(4),');
70
71 plot(
72   -st => ds::Pair(
73     $z, sqrt( $st / maximum($st) ),
74     colors => pdl(255,0,0)->rgb_to_color,
75     plotType => ppair::Lines,
76     lineWidths => 3,
77   ),
78   -sz => ds::Pair(
79     $z, sqrt( $sz / maximum($sz) ),
80     colors => pdl(0,255,0)->rgb_to_color,
81     plotType => ppair::Lines,
82     lineWidths => 3,
83   ),
84   x => { label => 'Position (m)' },
85 );

```

As a further example, I also include the script used to generate Figure 5 and Figure 6. In this example, in lines 12-56 I define a function, which simulates the pulse dynamics for a given number of electrons with the option of having a realistic photocathode and acceleration region or an idealized pulse. From there, I loop over a set of predefined number of charges per pulse,

APPENDIX (Continued)

simulate each sequentially and extract the final pulse dimensions after a propagation distance of 15cm. I write this data to a file to be plotted elsewhere.

```

1  #!/usr/bin/env perl
2
3  use strict;
4  use warnings;
5
6  use Getopt::Long;
7  GetOptions( accelerator => \my $use_acc );
8
9  use Physics::UEMColumn alias => [qw/:standard Pulse/];
10 use Physics::UEMColumn::Auxiliary qw/:materials :constants/;
11
12 sub for_number {
13     my ($num, $use_acc) = @_;
14
15     my $sim;
16     if ( $use_acc ) {
17         my $laser = Laser->new(
18             width    => '1 mm',
19             duration => '1 ps',
20             energy   => '4.75 eV',
21         );
22
23         my $acc = DCAccelerator->new(
24             length => '20 mm',
25             voltage => '30 kilovolts',
26         );
27
28         my $column = Column->new(
29             length    => '15 cm',
30             laser     => $laser,
31             accelerator => $acc,
32             photocathode => Photocathode->new(Ta),
33         );
34
35         $sim = Physics::UEMColumn->new(
36             column => $column,
37             number => $num,
38         );
39     } else {
40
41         $sim = Physics::UEMColumn->new(
42             column => Column->new( length => '15 cm' ),
43             pulse  => Pulse->new(
44                 number => $num,
45                 initial_width => '1 mm',
46                 initial_length => ( vc / 3 * 1e-12 ) . ' m',
47                 velocity => vc / 3,
48             ),
49         );
50     }
51 }
52

```


APPENDIX (Continued)

```

53
54     my $result = $sim->propagate;
55     return $result;
56 }
57
58 my $outfilename = $use_acc ? 'spacecharge_acc.dat' : 'spacecharge_noacc.dat';
59 open my $fh, '>', $outfilename or die "Cannot open $outfilename for writing";
60
61 my @nums = map { ("1e$_", "2.2e$_", "4.6e$_") } (0..8);
62 pop @nums for 1..2;
63
64 for my $num ( @nums ) {
65     my $result = for_number($num, $use_acc);
66     for (@$result) {
67         next unless $_->[1] >= 0.15;
68         print {$fh} $num . ' ' . sqrt( 2 * $_->[3] ) * 1e3 . ' ' . sqrt( 2 * $_->[4] ) * 1e3 . "\n";
69         last;
70     }
71 }

```

I present these examples to demonstrate the utility of the Perl implementation of the AG model; I hope it will be useful to other members of the UEM community. Other examples may be seen in the source repository for this thesis, which is available at <https://github.com/jberger/Thesis>.

CITED LITERATURE

1. Amplitude Systemes. <http://www.amplitude-systemes.com/>.
2. BATOP GmbH. <http://www.batop.de>.
3. EKSPLA. <http://www.ekspla.com>.
4. High Q Laser Production GmbH. <http://www.highqlaser.at>.
5. Layertec GmbH. <http://www.layertec.de>.
6. Lissotschenko Mikrooptik (LIMO) GmbH. <http://www.limo.de>.
7. Newlight Photonics Inc. <http://www.newlightphotonics.com>.
8. Nova Phase. <http://www.novaphase.com>.
9. SOLAR Laser Systems. <http://www.solarlaser.com>.
10. Time-Bandwidth Products. <http://www.tbwp.com>.
11. Compact x-ray light source workshop report. Technical Report Contract DE-AC05-76RL01830, Pacific Northwest National Laboratory, 2012.
12. Armstrong, M. R., Boyden, K., Browning, N. D., Campbell, G. H., Colvin, J. D., DeHope, W. J., Frank, A. M., Gibson, D. J., Hartemann, F., Kim, J. S., King, W. E., LaGrange, T. B., Pyke, B. J., Reed, B. W., Shuttlesworth, R. M., Stuart, B. C., and Torralva, B. R.: Practical considerations for high spatial and temporal resolution dynamic transmission electron microscopy. Ultramicroscopy, 107(4-5):356–367, 2007.
13. Armstrong, M. R., Reed, B. W., Torralva, B. R., and Browning, N. D.: Prospects for electron imaging with ultrafast time resolution. Appl. Phys. Lett., 90(11):114101–3, 2007.

14. Aspnes, D. E. and Studna, A. A.: Dielectric functions and optical parameters of Si, Ge, GaP, GaAs, GaSb, InP, InAs, and InSb from 1.5 to 6.0 eV. Phys. Rev. B, 27:985–1009, Jan 1983.
15. Berger, J. and Schroeder, W.: Semianalytic model of electron pulse propagation: Magnetic lenses and rf pulse compression cavities. Journal of Applied Physics, 108(12):124905, 2010.
16. Berger, J. A., Greco, M. J., and Schroeder, W. A.: High-power, femtosecond, thermal-lens-shaped Yb:KGW oscillator. Opt. Express, 16(12), 2008.
17. Berger, J. A., Hogan, J. T., Greco, M. J., Schroeder, W. A., Nicholls, A. W., and Browning, N. D.: DC photoelectron gun parameters for ultrafast electron microscopy. Microsc. Microanal., 15(04), 2009.
18. Berger, J. A., Rickman, B. L., Li, T., Nicholls, A. W., and Schroeder, W. A.: Excited-state thermionic emission in III-antimonides: Low emittance ultrafast photocathodes. Applied Physics Letters, 101(19):194103, 2012.
19. Biswal, S., O'Connor, S. P., and Bowman, S. R.: Thermo-optical parameters measured in ytterbium-doped potassium gadolinium tungstate. Appl. Opt., 44(15):3093–3097, May 2005.
20. Bostanjoglo, O. and Liedtke, R.: Tracing fast phase transitions by electron microscopy. Phys. Status Solidi A, 60(2):451–455, 1980.
21. Brenier, A. and Boulon, G.: New criteria to choose the best Yb³⁺-doped laser crystals. EPL (Europhysics Letters), 55(5):647, 2001.
22. Brunner, F., Spühler, G. J., der Au, J. A., Krainer, L., Morier-Genoud, F., Paschotta, R., Lichtenstein, N., Weiss, S., Harder, C., Lagatsky, A. A., Abdolvand, A., Kuleshov, N. V., and Keller, U.: Diode-pumped femtosecond Yb:KGd(WO₄)₂ laser with 1.1-W average power. Opt. Lett., 25(15):1119–1121, Aug 2000.
23. Brunner, F., Südmeyer, T., Innerhofer, E., Morier-Genoud, F., Paschotta, R., Kisel, V. E., Shcherbitsky, V. G., Kuleshov, N. V., Gao, J., Contag, K., Giesen, A., and Keller, U.: 240-fs pulses with 22-W average power from a mode-locked thin-disk Yb:KY(WO₄)₂ laser. Opt. Lett., 27(13):1162–1164, Jul 2002.

24. Brunner, F., Innerhofer, E., Marchese, S. V., Südmeyer, T., Paschotta, R., Usami, T., Ito, H., Kurimura, S., Kitamura, K., Arisholm, G., and Keller, U.: Powerful red-green-blue laser source pumped with a mode-locked thindisk laser. Opt. Lett., 29(16):1921–1923, Aug 2004.
25. Cao, J., Hao, Z., Park, H., Tao, C., Kau, D., and Blaszczyk, L.: Femtosecond electron diffraction for direct measurement of ultrafast atomic motions. Appl. Phys. Lett., 83(5):1044–1046, 2003.
26. Chelikowsky, J. R. and Cohen, M. L.: Nonlocal pseudopotential calculations for the electronic structure of eleven diamond and zinc-blende semiconductors. Phys. Rev. B, 14:556–582, Jul 1976.
27. Chelikowsky, J. R. and Cohen, M. L.: Erratum: Nonlocal pseudopotential calculations for the electronic structure of eleven diamond and zinc-blende semiconductors. Phys. Rev. B, 30:4828–4828, Oct 1984.
28. Chen, J., Tzou, D., and Beraun, J.: A semiclassical two-temperature model for ultrafast laser heating. Int. J. Heat & Mass Transfer, 49:307–316, 2006.
29. Child, C. D.: Discharge from hot CaO. Phys. Rev. (Series I), 32:492–511, May 1911.
30. Cottam, M. G. and Tilley, D.: Introduction to Surface and Superlattice Excitations. Graduate Student Series in Physics. Taylor & Francis, second edition, 2004.
31. Courjaud, A., Deguil, N., and Salin, F.: High power diode-pumped yb:kgw ultrafast laser. In OSA Trends in Optics and Photonics (TOPS) 73, Conference on Lasers and Electro-Optics, OSA Technical Digest, pages 501–502, Washington DC, 2002. Optical Society of America, OSA.
32. Desjonqueres, M.-C. and Spanjaard, D.: Concepts in Surface Physics. Springer Series in Surface Sciences. Springer, second edition, 2002.
33. Domer, H. and Bostanjoglo, O.: High-speed transmission electron microscope. Rev. Sci. Instrum., 74(10):4369–4372, 2003.
34. Dowell, D. H. and Schmerge, J. F.: Quantum efficiency and thermal emittance of metal photocathodes. Phys. Rev. ST Accel. Beams, 12:074201, Jul 2009.

35. Eastman, D. E.: Photoelectric work functions of transition, rare-earth, and noble metals. Phys. Rev. B, 2:1–2, Jul 1970.
36. Einstein, A.: Über einen die Erzeugung und Verwandlung des Lichtes betreffenden heuristischen Gesichtspunkt. Annalen der Physik, 322(6):132–148, 1905.
37. El-Kareh, A. B. and El-Kareh, J. C. J.: Electron beams, lenses, and optics, volume 1. New York, Academic Press, 1970.
38. Fill, E., Veisz, L., Apolonski, A., and Krausz, F.: Sub-fs electron pulses for ultrafast electron diffraction. New J. Phys., 8(11):272, 2006.
39. Fowler, R. H.: The analysis of photoelectric sensitivity curves for clean metals at various temperatures. Phys. Rev., 38:45–56, Jul 1931.
40. Gobeli, G. W. and Allen, F. G.: Photoelectric properties of cleaved GaAs, GaSb, InAs, and InSb surfaces; comparison with Si and Ge. Phys. Rev., 137:A245–A254, Jan 1965.
41. Hellström, J., Bjurshagen, S., Pasiskevicius, V., Liu, J., Petrov, V., and Griebner, U.: Efficient Yb:KGW lasers end-pumped by high-power diode bars. Applied Physics B: Lasers and Optics, 83:235–239, 2006.
42. Himpsel, F.: Angle-resolved measurements of the photoemission of electrons in the study of solids. Advances in Physics, 32(1):1–51, 1983.
43. Holtom, G. R.: Mode-locked Yb:KGW laser longitudinally pumped by polarization-coupled diode bars. Opt. Lett., 31(18):2719–2721, Sep 2006.
44. Humphries, S.: Principles of Charged Particle Acceleration. John Wiley and Sons, 1986.
45. Jensen, K. L., O'Shea, P. G., Feldman, D. W., and Shaw, J. L.: Emittance of a field emission electron source. Journal of Applied Physics, 107(1):014903, 2010.
46. Jensen, K. L., O'Shea, P. G., Feldman, D. W., and Moody, N. A.: Theoretical model of the intrinsic emittance of a photocathode. Appl. Phys. Lett., 89(22):224103–3, 2006.
47. Johnson, P. B. and Christy, R. W.: Optical constants of the noble metals. Phys. Rev. B, 6:4370–4379, Dec 1972.

48. Kash, J. A., Tsang, J. C., and Hvam, J. M.: Subpicosecond time-resolved raman spectroscopy of LO phonons in GaAs. Phys. Rev. Lett., 54:2151–2154, May 1985.
49. Killi, A., Steinmann, A., Döring, J., Morgner, U., Lederer, M. J., Kopf, D., and Fallnich, C.: High-peak-power pulses from a cavity-dumped Yb:KY(WO₄)₂ oscillator. Opt. Lett., 30(14):1891–1893, Jul 2005.
50. Kim, K.-J.: RF and space-charge effects in laser-driven RF electron guns. Nucl. Instrum. Meth. A, 275(2):201–218, 1989.
51. King, W. E., Campbell, G. H., Frank, A., Reed, B., Schmerge, J. F., Siwick, B. J., Stuart, B. C., and Weber, P. M.: Ultrafast electron microscopy in materials science, biology, and chemistry. J. Appl. Phys., 97(11):111101–27, 2005.
52. Koechner, W.: Thermal lensing in a Nd:YAG laser rod. Appl. Opt., 9(11):2548–2553, Nov 1970.
53. Kupersztych, J., Monchicourt, P., and Raynaud, M.: Ponderomotive acceleration of photoelectrons in surface-plasmon-assisted multiphoton photoelectric emission. Phys. Rev. Lett., 86:5180–5183, May 2001.
54. Kupersztych, J. and Raynaud, M.: Anomalous multiphoton photoelectric effect in ultra-short time scales. Phys. Rev. Lett., 95:147401, Sep 2005.
55. LaGrange, T., Armstrong, M. R., Boyden, K., Brown, C. G., Campbell, G. H., Colvin, J. D., DeHope, W. J., Frank, A. M., Gibson, D. J., Hartemann, F. V., Kim, J. S., King, W. E., Pyke, B. J., Reed, B. W., Shirk, M. D., Shuttlesworth, R. M., Stuart, B. C., Torralva, B. R., and Browning, N. D.: Single-shot dynamic transmission electron microscopy. Appl. Phys. Lett., 89(4):044105–3, 2006.
56. LaGrange, T., Campbell, G. H., Reed, B., Taheri, M., Pesavento, J. B., Kim, J. S., and Browning, N. D.: Nanosecond time-resolved investigations using the in situ of dynamic transmission electron microscope (DTEM). Ultramicroscopy, 108(11):1441–1449, 2008.
57. Langmuir, I.: The effect of space charge and initial velocities on the potential distribution and thermionic current between parallel plane electrodes. Phys. Rev., 21:419–435, Apr 1923.

58. Li, R. K., To, H., Andonian, G., Feng, J., Polyakov, A., Scoby, C. M., Thompson, K., Wan, W., Padmore, H. A., and Musumeci, P.: Surface-plasmon resonance-enhanced multiphoton emission of high-brightness electron beams from a nanostructured copper cathode. Phys. Rev. Lett., 110:074801, Feb 2013.
59. Li, Y. and Lewellen, J. W.: Generating a quasiellipsoidal electron beam by 3d laser-pulse shaping. Phys. Rev. Lett., 100(7):074801, Feb 2008.
60. Liu, H., Nees, J., and Mourou, G.: Diode-pumped kerr-lens mode-locked Yb:KY(WO₄)₂ laser. Opt. Lett., 26(21):1723–1725, Nov 2001.
61. Liu, Z., Sun, Y., Pianetta, P., and Pease, R. F. W.: Narrow cone emission from negative electron affinity photocathodes. volume 23, pages 2758–2762. AVS, 2005.
62. Lobastov, V. A., Srinivasan, R., and Zewail, A. H.: Four-dimensional ultrafast electron microscopy. Proc. Nat. Acad. Sci. U.S.A., 102(20):7069–7073, 2005.
63. Luiten, O. J., van der Geer, S. B., de Loos, M. J., Kiewiet, F. B., and van der Wiel, M. J.: How to realize uniform three-dimensional ellipsoidal electron bunches. Phys. Rev. Lett., 93(9):094802, Aug 2004.
64. Major, A., Nikolakakos, I., Aitchison, J., Ferguson, A., Langford, N., and Smith, P.: Characterization of the nonlinear refractive index of the laser crystal Yb:KGd(WO₄)₂. Applied Physics B: Lasers and Optics, 77:433–436, 2003.
65. Major, A., Barzda, V., Piunno, P. A. E., Musikhin, S., and Krull, U. J.: An extended cavity diode-pumped femtosecond Yb:KGW laser for applications in optical DNA sensor technology based on fluorescence lifetime measurements. Opt. Express, 14(12):5285–5294, Jun 2006.
66. Major, A., Cisek, R., and Barzda, V.: Femtosecond Yb:KGd(WO₄)₂ laser oscillator pumped by a high power fiber-coupled diode laser module. Opt. Express, 14(25):12163–12168, Dec 2006.
67. Maldonado, J. R., Pianetta, P., Dowell, D. H., Corbett, J., Park, S., Schmerge, J., Trautwein, A., and Clay, W.: Experimental verification of the 3-step model of photoemission for energy spread and emittance measurements of copper and csbr-coated copper photocathodes suitable for free electron laser applications. Applied Physics Letters, 101(23):231103, 2012.

68. Marchese, S. V., Südmeyer, T., Golling, M., Grange, R., and Keller, U.: Pulse energy scaling to 5 μJ from a femtosecond thin disk laser. Opt. Lett., 31(18):2728–2730, Sep 2006.
69. McDonald, K. T.: Design of the laser-driven RF electron gun for the BNL accelerator test facility. IEEE T. Electron Dev., 35:2052–2059, nov 1988.
70. Michalik, A. M. and Sipe, J. E.: Analytic model of electron pulse propagation in ultrafast electron diffraction experiments. J. Appl. Phys., 99(5):054908–9, 2006.
71. Michalik, A. M. and Sipe, J. E.: Erratum: “analytic model of electron pulse propagation in ultrafast electron diffraction experiments” [J. appl. phys. 99, 054908 (2006)]. J. Appl. Phys., 103(12):129901–1, 2008.
72. Michalik, A. M. and Sipe, J. E.: Evolution of non-Gaussian electron bunches in ultrafast electron diffraction experiments: Comparison to analytic model. J. Appl. Phys., 105(8):084913–10, 2009.
73. Mochalov, I. V.: Laser and nonlinear properties of the potassium gadolinium tungstate laser crystal $\text{KGd}(\text{WO}_4)_2\text{:Nd}^{3+}$ —(KGW:Nd). Optical Engineering, 36(6):1660–1669, 1997.
74. Monjushiro, H., Watanabe, I., and Yokoyama, Y.: Ultraviolet photoelectron yield spectra of thin gold films measured in air. Anal. Sci., 7:543–547, 1991.
75. Montgomery, D. B. and Terrell, J.: Some useful information for the design of air-core solenoids. Technical Report AFOSR-1525, Massachusetts Inst. of Tech., Cambridge. National Magnet Lab., 1961.
76. Németh, K., Harkay, K. C., van Veenendaal, M., Spentzouris, L., White, M., Attenkofer, K., and Srajer, G.: High-brightness photocathodes through ultrathin surface layers on metals. Phys. Rev. Lett., 104:046801, Jan 2010.
77. Ortaç, B., Schmidt, O., Schreiber, T., Limpert, J., Tünnermann, A., and Hideur, A.: High-energy femtosecond Yb-doped dispersion compensation free fiber laser. Opt. Express, 15(17):10725–10732, Aug 2007.
78. O’Shea, P. G.: Reversible and irreversible emittance growth. Phys. Rev. E, 57:1081–1087, Jan 1998.

79. Palmer, G., Siegel, M., Steinmann, A., and Morgner, U.: Microjoule pulses from a passively mode-locked Yb:KY(WO₄)₂ thin-disk oscillator with cavity dumping. Opt. Lett., 32(11):1593–1595, Jun 2007.
80. Park, H. S., Kwon, O., Baskin, J. S., Barwick, B., and Zewail, A. H.: Direct observation of martensitic Phase-Transformation dynamics in iron by 4D Single-Pulse electron microscopy. Nano Lett., 9(11):3954–3962, 2009.
81. Paunescu, G., Hein, J., and Sauerbrey, R.: 100-fs diode-pumped Yb:KGW mode-locked laser. Applied Physics B: Lasers and Optics, 79:555–558, 2004.
82. Polyakov, A., Senft, C., Thompson, K. F., Feng, J., Cabrini, S., Schuck, P. J., Padmore, H. A., Peppernick, S. J., and Hess, W. P.: Plasmon-enhanced photocathode for high brightness and high repetition rate x-ray sources. Phys. Rev. Lett., 110:076802, Feb 2013.
83. Portella, M. T., Bigot, J.-Y., Schoenlein, R. W., Cunningham, J. E., and Shank, C. V.: k-space carrier dynamics in GaAs. Applied Physics Letters, 60(17):2123–2125, 1992.
84. Pujol, M., Rico, M., Zaldo, C., Solé, R., Nikolov, V., Solans, X., Aguiló, M., and Díaz, F.: Crystalline structure and optical spectroscopy of Er³⁺-doped KGd(WO₄)₂ single crystals. Applied Physics B: Lasers and Optics, 68:187–197, 1999.
85. Reed, B. W.: Femtosecond electron pulse propagation for ultrafast electron diffraction. J. Appl. Phys., 100(3):034916–16, 2006.
86. Reed, B., Armstrong, M., Browning, N., Campbell, G., Evans, J., LaGrange, T., and Masiel, D.: The evolution of ultrafast electron microscope instrumentation. Microsc. Microanal., 15(04):272–281, 2009.
87. Rimington, N., Schieffer, S., Schroeder, W., and Brickeen, B.: Thermal lens shaping in Brewster gain media: A high-power, diode-pumped Nd:GdVO₄ laser. Opt. Express, 12(7):1426–1436, Apr 2004.
88. Rose, A.: Television pickup tubes and the problem of vision. volume 1 of Advances in Electronics and Electron Physics, pages 131 – 166. Academic Press, 1948.
89. Saltiel, S. M., Koynov, K., Agate, B., and Sibbett, W.: Second-harmonic generation with focused beams under conditions of large group-velocity mismatch. J. Opt. Soc. Am. B, 21(3):591–598, Mar 2004.

90. Schieffer, S. L., Brajkovic, D., Cornea, A. I., and Schroeder, W. A.: Low-threshold, dual-passive mode locking of a large mode area Nd:GdVO₄ laser. Opt. Express, 14(15):6694–6704, Jul 2006.
91. Sciaini, G., Harb, M., Kruglik, S. G., Payer, T., Hebeisen, C. T., zu Heringdorf, F. M., Yamaguchi, M., von Hoegen, M. H., Ernstorfer, R., and Miller, R. J. D.: Electronic acceleration of atomic motions and disordering in bismuth. Nature, 458(7234):56–59, 2009.
92. Seah, M. P. and Dench, W. A.: Quantitative electron spectroscopy of surfaces: A standard data base for electron inelastic mean free paths in solids. Surface and Interface Analysis, 1(1):2–11, 1979.
93. Selivanov, A., Denisov, I., Kuleshov, N., and Yumashev, K.: Nonlinear refractive properties of Yb³⁺-doped KY(WO₄)₂ and YVO₄ laser crystals. Applied Physics B: Lasers and Optics, 83:61–65, 2006.
94. Shalae, V. M.: Electron escape and photoemission in the threshold region. Phys. Rev. B, 49:1437–1440, Jan 1994.
95. Shen, Y. R.: The Principles of Nonlinear Optics (Wiley Classics Library). Wiley-Interscience, 2002.
96. Siwick, B. J., Dwyer, J. R., Jordan, R. E., and Miller, R. J. D.: Ultrafast electron optics: Propagation dynamics of femtosecond electron packets. J. Appl. Phys., 92(3):1643–1648, 2002.
97. Siwick, B. J., Dwyer, J. R., Jordan, R. E., and Miller, R. J. D.: An Atomic-Level view of melting using femtosecond electron diffraction. Science, 302(5649):1382–1385, 2003.
98. Srinivasan, R., Lobastov, V. A., Ruan, C., and Zewail, A. H.: Ultrafast electron diffraction (UED). Helv. Chim. Acta, 86(6):1761–1799, 2003.
99. Strickland, D. and Mourou, G.: Compression of amplified chirped optical pulses. Opt. Commun., 56:219–221, 1985.
100. Togawa, K., Shintake, T., Inagaki, T., Onoe, K., Tanaka, T., Baba, H., and Matsumoto, H.: CeB₆ electron gun for low-emittance injector. Phys. Rev. ST Accel. Beams, 10(2):020703, Feb 2007.

101. Valfells, A., Feldman, D. W., Virgo, M., O'Shea, P. G., and Lau, Y. Y.: Effects of pulse-length and emitter area on virtual cathode formation in electron guns. Physics of Plasmas, 9(5):2377–2382, 2002.
102. van Oudheusden, T., de Jong, E. F., van der Geer, S. B., 't Root, W. P. E. M. O., Luiten, O. J., and Siwick, B. J.: Electron source concept for single-shot sub-100 fs electron diffraction in the 100 keV range. J. Appl. Phys., 102(9):093501–8, 2007.
103. Veisz, L., Kurkin, G., Chernox, K., Tarnetsky, V., Apolonski, A., Krausz, F., and Fill, E.: Hybrid dc-ac electron gun for fs-electron pulse generation. New J. Phys., 9:451–468, 2007.
104. Vodchits, A., Kozich, V., Orlovich, V., and Apanasevich, P.: Z-Scan studies of KYW, KYbW, KGW, and Ba(NO₃)₂ crystals. Optics Communications, 263(2):304 – 308, 2006.
105. Wang, H. and Weiner, A.: Efficiency of short-pulse type-I second-harmonic generation with simultaneous spatial walk-off, temporal walk-off, and pump depletion. IEEE Journal of Quantum Electronics, 39(12):1600–1618, Dec 2003.
106. Watts, R. A., Preist, T. W., and Sambles, J. R.: Sharp surface-plasmon resonances on deep diffraction gratings. Phys. Rev. Lett., 79:3978–3981, Nov 1997.
107. Williamson, J. C., Cao, J., Ihee, H., Frey, H., and Zewail, A. H.: Clocking transient chemical changes by ultrafast electron diffraction. Nature, 386(6621):159–162, 1997.
108. Yen, R., Liu, J., and Bloembergen, N.: Thermally assisted multiphoton photoelectric emission from tungsten. Optics Communications, 35(2):277 – 282, 1980.
109. Yumashev, K., Savitski, V., Kuleshov, N., Pavlyuk, A., Molotkov, D., and Protasenya, A.: Laser performance of N_g -cut flash-lamp pumped Nd:KGW at high repetition rates. Applied Physics B: Lasers and Optics, 89:39–43, 2007.
110. Zawadzka, J., Jaroszynski, D. A., Carey, J. J., and Wynne, K.: Evanescent-wave acceleration of ultrashort electron pulses. Applied Physics Letters, 79(14):2130–2132, 2001.
111. Zewail, A. H.: Laser femtochemistry. Science, 242(4886):1645–1653, 1988.

VITA

NAME:	Joel Adam Berger
EDUCATION:	B.S., Physics, University of Illinois at Chicago, Chicago, Illinois, 2005
TEACHING:	<p> \LaTeX for Technical Publishing (PHYS491 - Spring 2011) </p> <p> Problem-Solving Workshop for General Physics II (Electricity and Magnetism), General Physics II (Electricity and Magnetism) Lab, General Physics I (Mechanics) </p>
PROFESSIONAL MEMBERSHIPS:	<p>Microscopy Society of America</p> <p>Midwest Microscopy and Microanalysis Society</p>
SELECTED PUBLICATIONS:	<p> Berger, J. A., Greco, M. J., and Schroeder, W. A.: High-power, femtosecond, thermal-lens-shaped Yb:KGW oscillator. <u>Opt. Express</u>, 16(12), 2008. </p> <p> Berger, J. A., Hogan, J. T., Greco, M. J., Schroeder, W. A., Nicholls, A. W., and Browning, N. D.: DC photoelectron gun parameters for ultrafast electron microscopy. <u>Microsc. Microanal.</u>, 15(04), 2009. </p> <p> Berger, J. and Schroeder, W.: Semianalytic model of electron pulse propagation: Magnetic lenses and rf pulse compression cavities. <u>Journal of Applied Physics</u>, 108(12):124905, 2010. </p> <p> Berger, J. A., Rickman, B. L., Li, T., Nicholls, A. W., and Schroeder, W. A.: Excited-state thermionic emission in III-antimonides: Low emittance ultrafast photocathodes. <u>Applied Physics Letters</u>, 101(19):194103, 2012. </p>

Figure 11(b), Figure 12, Figure 13(b), Figure 14 and Figure 15 were previously published in Optics Express. The full article is available at <http://www.opticsinfobase.org/oe/abstract.cfm?uri=oe-16-12-8629>. Their use of these figures is granted to the author under the permissive non-commercial terms of the copyright transfer agreement (http://www.opticsinfobase.org/oe/submit/review/copyright_permissions.cfm).